Computational Modeling and Advanced Synthesis Techniques for the Improved Design of Zeolite Catalysts

A Dissertation
Presented to
the Faculty of the Department of Chemical and Biomolecular Engineering
University of Houston

In Partial Fulfillment
of the Requirements for the Degree
Doctor of Philosophy
in Chemical Engineering

by
Arian Ghorbanpour
December 2015

Computational Modeling and Advanced Synthesis Techniques for the Improved Design of Zeolite Catalysts

Arian Ghorbanpour

Approved:

Chair of the Committee,
Lars C. Grabow, Assistant Professor,
Chemical and Biomolecular Engineering

Chair of the Committee,
Jeffrey D. Rimer, Associate Professor,
Chemical and Biomolecular Engineering

Committee Members:

Michael P. Harold, Professor,
Chemical and Biomolecular Engineering

William S. Epling, Professor,
Chemical and Biomolecular Engineering

Jakoah Brgoch, Assistant Professor,
Chemistry

Ivan A. Konstantinov, Associate Scientist,
Dow Chemical

Suresh K. Khator, Associate Dean,
Cullen College of Engineering

Michael P. Harold, Professor and Chair,
Chemical and Biomolecular Engineering

Acknowledgements

My academic journey as a PhD student was greatly impacted by many people. I would like to express my utmost appreciation and special thanks to my PhD advisors, Dr. Lars Grabow and Dr. Jeffrey Rimer. Without their invaluable mentorship, guidance, encouragement, and patience during the PhD program, this accomplishment would not have been possible.

I am grateful to all the committee members who evaluated my research work, Dr. William Epling, Dr. Michael Harold, Dr. Jakoah Brgoch, and Dr. Ivan Konstantinov, for their useful comments. I would also like to acknowledge our collaborators at the University of Oklahoma, Dr. Steven Crossley and his student Abhishek Gumidyala, for enriching my research.

I was fortunate to have the opportunity to work in two wonderful research groups at the University of Houston. I would like to thank all my current and former fellow group members, especially Dr. Hieu Doan and Dr. Byeongjin Baek for their precious help and technical consultations through all these years. It was a very pleasant experience working closely in the same office with Dr. Alexandra Lupulescu, Dr. Sahar Farmanesh, Matthew Oleksiak, Jihae Chung, Manjesh Kumar, Dr. Di Wang, and Dr. Ming-Feng Hsieh, for which I am very grateful. I am also thankful to my other lab mates: Sashank Kasiraju, Rui Li, Wei Qin, Yufeng Shen, Katy Olafson, Megan Ketchum, Bryan Alamani, Madhuresh Choudhary, Dr. Shengguang Wang, Yuying Song, and Quan Do.

I have been blessed to have the friendship of some amazing people during the past five and half years; I would like to thank Heidar, Nabi, Ali, Homa, Mohammad, Neda,

Bahram, Yasser, Azadeh, Mahshid, and Ehsan, with whom I have shared my most enjoyable moments here.

Finally I would like to express my deepest appreciation to my family, especially my wonderful mother, who has been the greatest source of love, encouragement, and support in my life and academic endeavors.

Computational Modeling and Advanced Synthesis Techniques for the Improved Design of Zeolite Catalysts

An Abstract
of a
Dissertation
Presented to
the Faculty of the Department of Chemical and Biomolecular Engineering
University of Houston

In Partial Fulfillment
of the Requirements for the Degree
Doctor of Philosophy
in Chemical Engineering

by
Arian Ghorbanpour
December 2015

Abstract

Zeolites are the most widely used catalysts in industry due to a unique combination of features such as porous structure and high surface area, voids and channels of molecular dimensions, tunable active sites, and environmentally benign properties. To realize their great potential requires a thorough knowledge of structure-function relationships for rational zeolite design. Active sites in zeolites are created by Al substitution of framework Si atoms in crystallographically different positions on the exterior or in the interior of zeolite crystals. This leads to heterogeneous chemical/kinetic behavior of various active sites, which can be employed to tune the activity, selectivity, and lifetime of zeolites in catalytic processes. On the experimental side of this project, we enhance the shape selectivity of ZSM-5, an important zeolite catalyst in the petrochemical industry, by manipulating its active site distribution. Therefore, an advanced synthesis method was designed to passivate the external surface of ZSM-5 particles and suppress the reaction of bulky reactants over the exterior of the catalyst particles. The inert overlayer growth is performed at very low thicknesses and in an epitaxial structure so that the mass transfer limitations due to the added layer is minimized and the activity of internal active sites is not compromised.

We continue our investigation of the impact of heterogeneous distribution of active sites through atomic-scale modeling. Our density functional theory (DFT) simulation of H-ZSM-5 internal active sites reveal a large variation in the acidity and adsorption characteristics of 12 distinct active sites. The modeling of a test reaction, the dehydration of methanol to dimethyl ether (DME), indicates that the pore confinement effects that vary among different H-ZSM-5 active site locations result in nonidentical kinetic

behavior through different extents of transition state stabilization. This heterogeneous performance not only causes different rates of reaction, but also impacts the dominant reaction mechanism at typical reaction conditions. The distribution of H-ZSM-5 active sites in the form of paired acid sites, more likely to form in Al-rich zeolites, is also studied, which shows evidence for significant adsorption and kinetic variations compared to isolated active sites.

Table of Contents

List of Figures

List of Tables

Chapter 1 Introduction and overview

1.1 Introduction

Zeolites are crystalline microporous materials with a broad range of applications, which span from adsorption and ion exchange to catalysis, the latter possessing the largest market value among other applications.[1] Their success in the catalysis industry is mainly attributed to their porous structure and high surface area, channels and cavities with sizes in the range of molecular dimensions, versatile chemical composition, tunability of active sites' density and strength, and environmentally benign properties. Zeolites are aliminosilicate materials; in the siliceous form, they are composed of SiO_4 tedrahedra that can be interlinked in various ways to produce open structures with different topologies. When an aluminum atom (with three valence electrons) is substituted for a silicon atom (with four valence electrons) at a tetrahedral site (T site), a positively charged species such as an extra-framework metal cation or a proton is added to the framework to maintain charge neutrality. These positively charged sites result in the acidity property of aluminosilicate zeolites, which is the origin of their activity in most catalytic applications. The acid site is called a Lewis acid site if the extra-framework cation is a metallic species and a Brønsted acid site if the cation is a proton. Zeolite catalysts are currently employed in a large number of processes such as fluid catalytic cracking (FCC), isomerization, alkylation, methanol-to-hydrocarbon (MTH) conversion, NO_x abatement, etc.

Despite several recent advances in tailored zeolite synthesis, further improvements are needed to enhance their cost-effectiveness as well as their performance in terms of activity, selectivity, and lifetime. A common phenomenon observed in zeolite

crystallization is the tendency to form pore channels along the longest crystal dimensions, which has detrimental consequences on catalytic conversion through excessive mass transfer limitations and intensification of coke formation in the zeolite porous network.[2] Choi et al. obtained dramatically decreased catalyst deactivation through coke formation when using unilamellar zeolite MFI nanonsheets (2 nm thick) compared to the conventional zeolite in the methanol-to-gasoline (MTG) conversion.[3] In this case, the zeolite performance was enhanced through increasing the density of active sites located at the external surface of zeolite particles. An outstanding characteristic of zeolite catalysts, which is also impacted by their external surface area, is their shape and size selectivity owing to a variety of pore channel sizes of around molecular dimensions (eight-membered ring, ten-membered ring, and twelve-membered ring) formed by different frameworks. Large external surface area of zeolite particles can, however, have negative impacts on the reaction selectivity when the formation of the desired product benefits from the confined porous environment of zeolite framework. A well-known example is the disproportionation or alkylation of alkyl benzenes over H-ZSM-5, where smaller zeolite crystals result in a reduced selectivity toward the more valuable para isomers.[4-5] In this case, the confined environment in the interior of the zeolite is in favor of production and diffusion of the less bulky para isomers, while ortho and meta isomers can more readily form on the crystal exterior. These instances indicate some of the challenges in the synthesis of zeolite catalysts with desired performance.

Investigation of structure-property relationships toward a rational zeolite catalyst design necessitates understanding the complications associated with the structure and active site environment of zeolite materials. Their porous structure allows reactive centers

to be found both on the exterior and in the interior of zeolite particles. It is reasonable to expect different chemical behavior for the external active sites from those in the bulk due to the termination of chemical bonds and the absence of pore confinement on the external surface. Kim et al. observed a weaker acid strength and higher stability against steam treatment in external than in internal acid sites of MFI zeolites, although both domains indicated similar activity in the dehydration of methanol to dimethyl ether (DME).[6] Tighter confined environment within zeolite pores often leads to stronger guest-host attractive interactions and stronger adsorption enthalpies, while the adsorption entropy loss increases due to loss of mobility,[7] as shown by Eder et al.[8-10] for adsorption of alkanes over FER, MFI, and MOR zeolites. Albeit, if the void is too tight or the adsorbate size is too large to fit in the void, repulsion eventually dominates and the confinement will no longer be in favor of adsorbate stabilization. The stabilization of guest species within zeolite structure similarly applies to reaction transition states solvated by zeolite pore walls, which as a result influences catalytic reactivity. It has been shown that the rate of alkanol dehydration over acidic zeolites depends on the confining void size as long as the most abundant surface intermediate (MASI) species and the transition states are not confined to the same extent; i.e., are not of the same size.[7, 11] Dissimilar confinement effects may be observed at different internal locations of one individual framework as well. For example, the different environments of 8-MR pockets and 12-MR channels in the zeolite framework MOR have different kinetic behavior in the carbonylation of DME to methyl acetate.[7, 12] Heterogeneity in zeolitic internal structure and void size can also influence reaction selectivity through unequal solvation of transition states in two competing parallel reactions.

As briefly explained above, the concept of shape selectivity in zeolite catalysis is beyond the discrimination on the transport of reactants or products toward or out of the zeolite porous network, and understanding the heterogeneity of acid site properties throughout the catalyst framework is crucial. A number of experimental techniques such as temperature-programmed desorption (TPD), infrared (IR) spectroscopy, and nuclear magnetic resonance (NMR) have been employed extensively to investigate the properties of acid sites. Computational chemistry has also been given significant attention recently in understanding heterogeneous catalysis. In particular, density functional theory (DFT) has proved promising because of the balance it provides between accuracy and computational cost.[13] Construction of Brønsted-Evans-Polanyi and linear scaling relations for the computation of activation energies and adsorption energies of reaction intermediates based on simple descriptors to screen transition metal catalysts is one successful example where DFT can help to identify the optimal catalyst in a reaction of interest.[13-17] In the zeolite field, DFT applications are not limited to the calculation of reaction rates and can provide invaluable information in a large variety of areas such as investigating different stages of crystallization, evaluation of dispersion forces in zeolite guest-host interactions, characterization of zeolitic acid strength through vibrational analysis of the Brønsted O–H bond upon the adsorption of a probe base, etc.[18]

A principal difficulty associated with the experimental characterization of active sites in many zeolite frameworks is the presence of multiple crystallographically distinguishable T sites in a single framework serving as an acid site through Al substitution, which can in turn determine the performance of the zeolite.[19] For instance, the commercially popular zeolite frameworks known as the “big five”, i.e., Y, MFI,

MOR, BEA, and FER, have 1 (space group Fd-3m), 12 (space group Pnma), 4 (space group Cmcm), 9 (space group $P4_122$), and 4 (space group Immm) distinguishable T sites, respectively.[20] A number of experimental techniques such as Al NMR,[21-22] X-ray standing wave,[19] and X-ray scattering off metallic cations in metal-exchanged zeolites[23] have been used to resolve Al distribution among potential T sites. Despite the achievements, this problem has not been solved entirely and remains a challenging task, especially in zeolites with a low aluminum content and/or high number of distinguishable T sites occupied by Al.[23-24] DFT calculations can assist experimental attempts, e.g., by predicting NMR chemical shifts,[24] or be independently applied to probe the more stable Al sitings and investigate the structural, chemisorption, and kinetic properties of each of the potential active site locations. It must, however, be noted that the Al occupation of zeolite T sites is not determined only by thermodynamic stability and is, to a great extent, dependent on synthesis conditions.[22] The information that theoretical methods provide regarding the functionality of various acid sites in the zeolite structure, e.g., binding energies or reaction activation barriers, can be utilized in a more rational design of zeolite catalysts/adsorbents; examples include: 1) Working out synthesis techniques that enable us to selectively substitute T sites of interest in the zeolite framework for Al. Systematic tuning of active site locations in zeolite synthesis has not been accomplished so far. However, some progress has been made in selectively populating T sites by means of using different organic structure directing agents (OSDAs) in the synthesis formulation of zeolites FER[21] and MFI.[25] 2) Enriching crystals' external surface in Al or inversely making an Al-free zone close to the crystal rim, depending on which type of active sites (surface or bulk) favor activity and/or selectivity. The former phenomenon has been

reported by multiple groups in the synthesis of ZSM-5 using tetrapropylammonium (TPA) as OSDA.[26-30] Producing zeolite particles with an efficient passivating Al-free shell near the crystal exterior, however, requires additional post-synthesis treatments. 3) Synthesis of hierarchical structures and ultrathin nanosheets with high external surface areas,[3, 31] delaminated zeolites,[32] desilicated zeolites,[33] and morphology-modified structures through the use of zeolite growth modifiers,[34] which facilitate the access of bulky reactants to active sites and decrease mass transfer limitations and thereby enhance rate of reaction.

1.2 Present work

A combination of experimental efforts and computational modeling was used in the present work to enrich our knowledge of approaches to the improved design of zeolite catalysts. Ultimately, these efforts aim to investigate the impact of heterogeneous distribution of active sites, i.e., aluminum atoms, within the zeolite structure, how it can influence the catalytic performance, and how this knowledge may be employed in practice to enhance some of the catalyst properties. We focus on ZSM-5, a medium pore (10-MR) MFI-structured zeolite, which is the second most used zeolite catalyst after zeolite Y. The specific size of the of the porous network in ZSM-5 gives it a high shape selectivity property in the production of chemicals of interest such as para-xylene in the methylation/disproportionation of toluene, where the other two xylene isomers (meta and ortho) are too bulky to readily form and/or diffuse through the porous medium. This feature, however, is attenuated when the density of external surface active sites are considerable, e.g., in nano-sized particles. One way to circumvent this drawback is, as briefly mentioned above, the surface passivation of zeolite particles, i.e., making core-

shell particles with an active core and an inert shell, through secondary treatments and restricting the reactive sites to the internal porous medium. In chapter 3, we report our efforts to produce such structures and the relevant characterizations to validate the desired properties of the product. We then continue with our theoretical studies to understand the properties of ZSM-5 active sites at the atomic scale and how they influence zeolite catalytic performance. It would be desirable to make a comparison of surface and bulk active site performance following the surface modification work discussed in chapter 3. This task, however, does not prove straightforward. There is no prior indication of which T sites are populated by Al on the external surface of ZSM-5 crystals. The latter Al siting also differs at various crystallographic faces of MFI and is influenced by the synthesis conditions and morphology of the synthesized particles. The high number of potential acid site locations (12) in the interior of ZSM-5 structure imposes additional difficulties in the selection of a representative T site in the bulk to compare its behavior with a suitable counterpart on the crystal exterior. As a result, we decided to move one step back and begin the theoretical study of ZSM-5 acid sites' behavior with a thorough investigation of the 12 potential Al sitings in the bulk of ZSM-5. Chapter 4 discusses the chemical binding and site-specific acidity of all potential acid sites in ZSM-5. In chapter 5, we extend the comparison of ZSM-5 acid sites and their local environment to their kinetic behavior in the methanol-to-dimethyl ether (DME) reaction. Each of the zeolite models used in the simulations discussed in chapters 4 and 5 is comprised of one isolated acid site in an MFI unit cell, i.e., Si/Al atomic ratio of 95. In chapter 6, we take into account the possibility of the presence of two neighboring acid

sites in the zeolite structure at lower Si/Al ratios and its subsequent adsorption and kinetic effects.

Chapter 2 Methods

2.1 Experimental

The experimental techniques used to synthesize and characterize the ZSM-5 and ZSM-5@silicalite-1 (core-shell) catalysts are described in this section.

2.1.1 Materials

The following chemicals were purchased from Sigma Aldrich: tetraethylorthosilicate (TEOS, 98%), aluminum isopropoxide (98%), sodium hydroxide pellets (NaOH, 98%), 1,3,5-tri-isopropyl-benzene (TIPB, 95%), acetic acid (ACS reagent, ≥99.7%), isopropylamine (IPA >99.5%), and 2,6-di-tertbutyl pyridine (DTBP, >97%). Tetrapropylammonium hydroxide (TPAOH, 40%) was purchased from Alfa Aesar. The deionized (DI) water used for all synthesis and analytical measurements was purified with an Aqua Solutions RODI-C-12A purification system (18.2 MΩ). All gases necessary for reactions and gas chromatography analysis (He, N_2, H_2, and air) were obtained from Airgas. The N_2 for textural analysis was obtained from Praxair.

2.1.2 Synthesis of ZSM-5 seeds

Growth solutions were prepared with a molar composition of 6 TPAOH:0.1 Na_2O:25 SiO_2:0.25 Al_2O_3:480 H_2O:100 EtOH. We first added TEOS dropwise to a solution of TPAOH, NaOH, and DI water (25 mL total volume). This solution was stirred overnight at room temperature. Aluminum isopropoxide was added and the mixture was aged for an additional 24 hours at room temperature with continuous stirring. The solution was then placed in an acid digestion bomb (Parr Instruments) and was heated in a ThermoFisher Precision 3050 Series gravity oven at 100 °C. The solution was removed after 60 hours and immediately cooled to room temperature. The crystalline product was isolated from

the supernatant by three centrifugation and washing cycles of the mother liquor with DI water at 13,000 rpm for 40 minutes. The water was decanted, leaving behind a gel containing the ZSM-5 crystals. For protocols without an annealing step, a portion of the ZSM-5 gel was removed and dried in air for further characterization, while the remaining gel was directly added to a silicalite-1 growth solution (without drying) to prepare core-shell particles. For protocols employing an annealing step, the entire ZSM-5 gel was transferred to a solution with composition 10 TEOS:14 TPAOH:9500 H_2O. This solution was prepared by adding an appropriate amount of TEOS (dropwise) to a solution containing TPAOH and DI water (25 mL total volume). The solution was stirred at room temperature overnight prior to the addition of ZSM-5 seed crystals (1 wt%). The solution containing ZSM-5 seeds was thoroughly mixed, placed in an acid digestion bomb, and heated for 12 days at 170 ºC. The solution was removed from the oven and cooled to room temperature. A similar centrifugation/washing procedure was used to isolate the ZSM-5 crystals as a gel, which was fully transferred to a silicalite-1 growth solution (without drying).

2.1.3 Synthesis of ZSM-5@silicalite-1

A layer of silicalite-1 was grown on ZSM-5 seeds using a growth solution with a molar composition of x TEOS:14 TPAOH:9500 H_2O (with x = 17 – 40). This solution was prepared by adding an appropriate amount of TEOS (dropwise) to a solution containing TPAOH and DI water (25 mL total volume). The solution was stirred at room temperature overnight. Shell growth was carried out by adding ZSM-5 seeds (1 wt%) to the silicalite-1 growth solution. Prior to hydrothermal treatment, the solution pH was measured using an Orion 3-star Plus pH benchtop meter and 8102BNUWP ROSS Ultra electrode. The

suspension was placed in an acid digestion bomb and heated for 24 hours at 100 °C. The solution was removed from the oven and cooled to room temperature. A similar centrifugation/washing procedure was used to isolate ZSM-5@silicalite-1 crystals as a gel. For protocols without an annealing step, the entire gel was dried in air for further characterization. For processes employing an annealing step, the gel was directly transferred (without drying) to a solution with composition 10 TEOS:14 TPAOH:9500 H_2O, which was heated for 12 days at 170 ºC. The solution was then removed from the oven, the solid was isolated as a gel by centrifugation and washing, and the product was dried in air for further analysis.

2.1.4 Preparation of H-zeolites

ZSM-5 and ZSM-5@silicalite-1 samples were calcined to remove occluded TPA^+ from the pores using a ThermoScientific Lindberg Blue M tubular furnace. Calcination was performed with a temperature ramp rate of 1 ºC/min and a dwell time of 5 h at 550 ºC under the constant flow of compressed air (190 mL/min). An appropriate amount of each sample was then mixed with DI water to yield a 5 wt% suspension. This suspension was heated at 70 ºC for 12 h, and washed with DI water by centrifugation and decanting, such that the pH of the supernatant was within the range 6 to 7. The precipitate was mixed with a 1.0 M ammonium nitrate solution to yield a 5 wt% suspension. This suspension was then heated at 80 ºC for 5 h to allow the exchange of extra-framework Na^+ ions with NH_4^+. The solid material was recovered by centrifugation. This entire process was performed for a total of three cycles, and the final product was dried at room temperature and calcined at the same condition as above. The resulting H-form zeolite samples were

used for BET, XRD, XPS, IPA-TPD, probe reactions, and di-tertbutyl pyridine adsorption experiments.

2.1.5 Materials characterization

The MFI crystal structure of core and core-shell samples was verified by powder X-ray diffraction (XRD) using a Siemens D5000 X-ray diffractometer with CuKα radiation (40 kV, 30 mA, $\lambda = 1.54$ Å). The elemental composition of zeolite samples was determined by inductively coupled plasma atomic emission spectroscopy (ICP-AES) at Galbraith Laboratories (Knoxville, TN). The BET surface area of H-zeolite samples was measured by N_2 adsorption using a Micromeritics ASAP2020 instrument. Crystal morphology, size, and particle size distribution were assessed by scanning electron microscopy (SEM) using a FEI model Strata235 instrument. To prepare SEM samples, a small amount of the zeolite aqueous suspension was placed on a glass slide and dried overnight. The crystals were then transferred onto carbon grids and coated with a thin layer of carbon (ca. 30 nm). Transmission electron microscopy (TEM) was performed at the Texas A&M University Microscopy and Imaging Center. TEM specimens were prepared by dispersing zeolite particles in ethanol with sonication. A small droplet of the dispersion was placed on a TEM grid and dried with a filter paper. HRTEM, SAED, and EDS data were obtained with a Super-Twin TEM fitted with a Schottky field emission gun, a 2k x 2k Gatan CCD camera, and an EDS detector. EFTEM data was obtained using a FEI Tecnai G2 F20 ST FE-TEM instrument.

X-ray photoelectron spectroscopy (XPS) analysis of samples was performed using a PHI 5800 ESCA (Physical Electronics) multi-technique system equipped with a standard achromatic AlKα X-ray source (1486.6 eV) operating at 300 W (15kV and 20 mA) and a

concentric hemispherical analyzer. The samples were filled in the specimen holder and outgassed in the introduction chamber prior to analysis. Survey spectra (0 - 1400 eV) and high-resolution spectra were collected with a pass energy of 187.85 eV and 23.50 eV, respectively. All data were collected at a 45^{o} take-off angle. To compensate for surface charging effects, all spectra were referenced to the hydrocarbon C1s peak at 284.6 eV.

Growth solutions for dynamic light scattering (DLS) measurements were prepared with molar composition 14 TEOS:7 TPAOH:9500 H_2O (pH = 10.8) using the same protocol for silicalite-1 synthesis. To this solution was added an aliquot of stock ZSM-5 seed solution (3 g zeolite in 19 mL DI water) in the amount of 5 g seed solution per 75 g growth solution. After 30 min of stirring, the mixture was divided equally into three acid digestion bombs, and placed in an oven regulated at 100 °C. At various time points, a sample was removed from the oven, quenched to room temperature, filtered through a 0.45 mm nylon membrane (Pall Corp.), and diluted to obtain a transparent solution prior to DLS measurements. The degree of dilution was adjusted to ensure equal scattering count rates for each sample. Samples labeled as the zero time point refer to the solution without any heating. A total of three DLS measurements were taken for each sample (2 min per measurement) to obtain an average crystal size and standard deviation. Autocorrelation functions were analyzed using the method of cumulants to obtain an average hydrodynamic diameter. All measurements were performed using a Brookhaven Instruments BI-200SM machine equipped with a TurboCorr Digital Correlator, a HeNe laser (637 nm), and a refractive index matching decalin bath. The temperature of the DLS sample was regulated at 25 °C.

The ^{27}Al NMR experiments were performed on a Bruker AVIII HD NMR spectrometer operating at a magnetic field strength of 11.74 T, equipped with a 4 mm Bruker MAS probe. For the MAS experiments of ^{27}Al (130.3754 MHz), a single pulse acquisition was applied with a spinning speed of 14 KHz and a short RF pulse (less than 15°) with a recycle delay of 0.5-1 s. Spectra were collected after 10240 scans and referenced to $AlCl_3$ (aq. 1 M) at 0 ppm.

2.1.6 Material testing in a fixed bed reactor

Flow reaction studies were performed in a quartz tube reactor (1/4" OD) at atmospheric pressure. The H-zeolite catalyst was diluted with acid washed glass beads packed in the reactor between plugs of quartz wool. The inlet of the reactor was heated to create a vaporization zone and the outlet stream of the reactor as well as the six port valve for injection to the gas chromatograph (GC) were heated to 250 °C to prevent condensation. The temperature of the catalyst bed was controlled by a thermocouple attached to the outer wall of the reactor. The catalyst was preheated and flushed with helium (50 mL/min) for one hour at 400 °C before introducing the reactant via a syringe pump. The results and product distribution were analyzed using a HP-6890GC equipped with a flame ionization detector and innowax column (30 m and 0.25 μm). Reaction products were condensed in a sample bubbler using ice and water as a coolant medium for identification via GCMS.

For temperature programmed desorption (TPD) experiments, 50 mg of H-zeolite sample was packed in a quartz reactor (1/4" OD) between two quartz plugs and flushed at 400 °C for 1 h with helium as the carrier gas (50 mL/min). After pre-treatment, the temperature was reduced to 100 °C and 2 μL pulses of isopropylamine (IPA) were

injected into the reactor through a septum using a syringe. The IPA exiting the reactor was tracked by following species with a mass-to-charge ratio (m/z) of 58 using a MKS Cirrus 200 quadrupole mass spectrometer (MS) until the signal remained constant with additional pulses to ensure that all of the acid sites in the catalyst bed were saturated. After adsorption of IPA on to the catalyst bed, it was flushed with carrier gas at 20 mL/min and 100 °C for 4 h to remove any physically absorbed IPA, after which the temperature was ramped from 100 to 600 °C at a rate of 10 °C/min under a flow of He (20 mL/min). The outlet stream of the reactor was connected to the MS to analyze the desorbing species from the catalyst bed. Quantification of the number of moles of product evolved in the MS was conducted by injecting standards, with propylene gas injected through a sample loop. The Brønsted acid sites for each H-zeolite sample were quantified by integrating the moles of propylene (m/z = 41) desorbed during the IPA-TPD experiment.

Flow reaction studies of TIPB were performed at 400 °C and atmospheric pressure, keeping the W/F = 0.2 h, where W is the total mass of catalyst (g-zeolite) and F is the reactant feed rate (g-reactant h^{-1}). The acetic acid ketonization reaction was performed at 320 °C and atmospheric pressure with W/F = 0.3 h. Reactant and helium (carrier gas) feed rates for the probe reactions were 0.1 and 50 mL/min, respectively. For all reactions, the catalyst was first preheated and flushed with helium (50 mL/min) for one hour at 400 °C prior to introducing the reactant via a syringe pump.

Adsorption measurements with DTBP were conducted in a PerkinElmer Spectrum 100 FT-IR Spectrometer equipped with a Harrick Praying Mantis™ chamber. After pre-treating the H-zeolite sample at 300 °C in helium flow for 1 hour, the temperature was

reduced to 50 °C and a blank spectrum of the zeolite surface was taken as a reference. DTBP was then adsorbed onto the surface for 30 min at 50 °C through a sample bubbler maintained at –7 °C while flowing helium at a rate of 50 mL/min (using a Porter mass flow controller). This was followed by flushing for 2 hours at 50 °C under a flow of 50 mL/min to remove physically adsorbed DTBP. After flushing, the spectrum of the H-zeolite surface adsorbed with DTBP was collected at 50 °C and then the temperature was raised at a steady rate of 10 °C/min. Analysis at each desired temperature was conducted by stopping the ramp and holding at a fixed temperature to obtain the spectrum (64 scans) prior to continuing the temperature ramp.

2.2 Modeling

Density functional theory (DFT) is one of the most widely used methods for ab initio calculations of the structure of atoms, molecules, crystals, surfaces, and their interactions.[35] Numerous advantages such as its direct applicability to chemical reaction calculations including the prediction of geometries and energetics of transition states (in contrast to force field approaches), inclusion of electron correlation and relatively low computational resource consumption (e.g., compared to Hartree-Fock (HF) and MP2 methods, respectively) turn it into a very powerful tool. This technique is based on a few principles and approximations:

1) **Born-Oppenheimer approximation**: Atomic nuclei are much heavier than the electrons. As a result, electron response to changes in their surroundings is much more rapid than that of nuclei and thus, in evaluating the energy of a set of atoms, we can first optimize the position of electrons and obtain their ground-state energy while holding the nuclei fixed and then relax nuclei.

2) **Hohenberg-Kohn's theorem**: The ground-state energy from Schrödinger's equation ($H\psi=E\psi$) is a unique functional of the electron density, i.e., $E=E[n(\mathbf{r})]$, where: $n(\mathbf{r})=2\Sigma\psi_i^*(\mathbf{r})\ \psi_i(\mathbf{r})$; E, n, $\mathbf{r}$, and ψ represent ground-state energy, electron density, position vector, and electron wave function, respectively.

3) **Kohn-Sham equations**: The original Schrödinger equation is a many-body problem; i.e., it involves the interactions between all electrons of the system, which makes the solution complicated. Kohn and Sham simplified the problem by expressing it in terms of separate equations, each of which is assigned to one individual electron,

$$\left[\frac{h^2}{2m}\nabla^2 + V(\mathbf{r}) + V_H(\mathbf{r}) + V_{XC}(\mathbf{r})\right]\psi_i(\mathbf{r}) = \varepsilon_i\psi_i(\mathbf{r}), \tag{2.1}$$

where the terms within the brackets (the Hamiltonian of the system) account for the electron kinetic energy, electron-nuclei, electron-electron (Hartree), and exchange-correlation potential, respectively.

Using the Kohn-Sham approach, a code may be developed in an iterative manner to get to the ground-state energy; one can define an initial, trial electron density, $n(\mathbf{r})$, solve the Kohn-Sham equations with this initial guess to find the single-particle wave functions, $\psi_i(\mathbf{r})$, calculate the new electron density, compare the latter with the initial guess, and continue this loop until convergence is reached. In contrast to the first three terms in equation (2.1), no analytical form of the exchange-correlation functional is known. Attempts made to fill this gap start with simple approaches such as Local Density Approximation (LDA) and extend to more sophisticated, complex functionals including the Generalized Gradient Approximation (GGA), Meta-GGA, and Hyper-GGA methods. The type of functional to select is an important step of any DFT calculation and determines the applicability and reliability of the results. The choice depends to a great

extent on the physical conditions of the problem and the functional's computational expensiveness. Especially van der Waals or dispersion interactions are often neglected (GGA) or described only empirically using a non self-consistently calculated electron density (e.g., DFT-D).[36] Dispersion forces, however, play a major role in zeolite catalysis due to the confinement of adsorbates and reaction species within the zeolite porous network. Development of more accurate, self-consistent, rapid exchange-correlation functionals is still an active area of research. Examples include the vdW-DF[37-38] and vdW-DF2[39] functionals, in which a fully non-local correlation potential describing long-range interactions is combined with local and semi-local exchange and correlation contributions.[40] We have tested a number of common exchange-correlation functionals including vdW-DF, and will show that the latter provides the most reasonable results in our calculations among others.

In our computational approach, we use the Vienna ab initio simulation package (VASP),[41-42] which finds the solutions of the Kohn-Sham equations (2.1) within a plane-wave basis set using a projector-augmented-wave (PAW)[43] method for describing the electron-ion interactions. Using a plane-wave approach, in particular, is appropriate when treating bulk materials with periodic structures such as zeolite crystals. Within this approach, wave functions can be described as a sum of finite set of functions,

$$\psi_i(\mathbf{r}) = \sum_{\mathbf{k}} \alpha_{i,\mathbf{k}} \phi_{\mathbf{k}}(\mathbf{r}), \tag{2.2}$$

where the set of functions $\phi_{\mathbf{k}}(\mathbf{r})$ is called the basis set for the calculation. Bloch's theorem asserts that the solution for $\phi_{\mathbf{k}}(\mathbf{r})$ must be of the from

$$\phi_{\mathbf{k}}(\mathbf{r}) = \exp(i\mathbf{k}.\mathbf{r})\, u_{\mathbf{k}}(\mathbf{r}), \tag{2.3}$$

where $\exp(i\mathbf{k}.\mathbf{r})$ are plane waves and $u_{\mathbf{k}}(\mathbf{r})$ are periodic functions with the same periodicity as that of the studied supercell. **r** vectors represent the real space and **k** vectors represent the reciprocal space. Although the larger number of points along each direction of the reciprocal space (**k** vector) provides higher precision in calculations, we limit our calculations in this work to **k** = **0** (Brillouin zone sampling around the **Γ** point only) due to the relatively large size of MFI zeolite unit cell (20.09 Å x 19.74 Å x 13.14 Å).[20] The periodic nature of $u_{\mathbf{k}}(\mathbf{r})$ follows that we can write

$$u_{\mathbf{k}}(\mathbf{r}) = \sum_{\mathbf{G}} c_{\mathbf{G}} \exp(i\mathbf{G}.\mathbf{r}) . \quad (2.4)$$

In equation (2.4), **G** is a linear combination of the reciprocal lattice vectors ($\mathbf{G} = m_1\mathbf{b}_1 + m_2\mathbf{b}_2 + m_3\mathbf{b}_3$). The coefficients m_1, m_2, and m_3 are defined so that for the real space lattice vectors $\mathbf{a}_i$, we have $\mathbf{G}.\mathbf{a}_i = 2\pi m_i$. Combining equations (2.3) and (2.4) we get

$$\phi_{\mathbf{k}}(\mathbf{r}) = \sum_{\mathbf{G}} c_{\mathbf{k}+\mathbf{G}} \exp(i(\mathbf{k}+\mathbf{G})\mathbf{r}). \quad (2.5)$$

The kinetic energy associated with the functions in equation (2.5) is $E = \frac{h^2}{2m}|\mathbf{k}+\mathbf{G}|^2$, the kinetic energy of the Schrödinger equation solutions. Although equation (2.5) is an infinite summation over **G**, it is reasonable to consider only the solutions with a kinetic energy lower than a maximum value $E_{\text{cut}} = \frac{h^2}{2m}G_{\text{cut}}^2$ and truncate the summation accordingly, so that

$$\phi_{\mathbf{k}}(\mathbf{r}) = \sum_{|\mathbf{G}+\mathbf{k}|<G_{\text{cut}}} c_{\mathbf{k}+\mathbf{G}} \exp(i(\mathbf{k}+\mathbf{G})\mathbf{r}). \quad (2.6)$$

The E_{cut} parameter is called the cutoff energy and we use a value of 540 eV in our calculations of this work.

Thermochemical properties such as entropy and Gibbs free energy are calculated within the ideal gas limit for gaseous compounds and the harmonic oscillator approximation, in which all degrees of freedom are treated harmonically, for solid and

adsorbed states. Such calculations require vibrational analysis to input the normal mode frequencies. The latter is obtained via the calculation of the energy Hessian matrix eigenvalues for a system composed of a collection of atoms. Since our system (the MFI unit cell + adsorbates/reaction species) is typically composed of ~300 atoms, taking all the present atoms into account would make these calculations too expensive. As a result, we have used a partial Hessian matrix in each of such calculations displacing only the adsorbate/reaction species and the zeolite acid site.

Chapter 3 Epitaxial growth of ZSM-5@silicalite-1: a core-shell zeolite designed with passivated surface acidity

The material discussed in this chapter has been published and is related to a project conducted in collaboration with the group of Dr. Steven Crossley at the University of Oklahoma. Figure and table numbers have been changed for dissertation consistency.

3.1 Introduction

Zeolites are used in a variety of applications owing to their unique acidity and nanoporous structures that are well-suited for catalysis, ion-exchange, sorption, and separations. The acidity of H-zeolites is attributed to Brønsted acid sites, which are located on oxygen atoms that bridge Si and Al atoms in the crystalline framework. In catalytic applications, Brønsted acid sites located within confined nanopores impose shape-selectivity to achieve narrow product distributions; however, acid sites on the exterior surfaces of zeolite crystals reduce product selectivity and can exhibit properties that differ from bulk sites.[6, 44] A catalyst "passivation" method was patented by Mobil in the 1970's to coat ZSM-5 (MFI type) surfaces with a catalytically inactive silica layer.[45] Surface passivation has proven to be a useful method for enhancing product selectivity in the production of para-xylene[46] and para-selective disproportionation and alkylation of aromatics.[47] The common catalyst deactivation route via external pore mouth plugging[48] could serve as justification for surface passivation as well. Additional examples include the production of methylamines using a passivated zeolite catalyst (RHO framework type) with enhanced selectivity for dimethylamine.[49]

Details regarding the synthesis and characterization of passivated zeolites are difficult to extract from patents. In addition, techniques reported in the literature tend to have associated drawbacks. Examples include post-synthesis dealumination by acid treatment,

which can generate crystal defects and/or mesopores.[50-52] An alternative approach is the modification of external functional groups on zeolite surfaces with a passivating agent. Examples include the use of metal oxides (e.g., Sb_2O_3)[53] and hydride, alkyl, or alkoxy compounds that chemisorb to the hydroxyl groups on zeolite surfaces.[54] This is frequently performed using chemical vapor deposition (CVD) or chemical liquid deposition (CLD) techniques.[55-58] These methods enhance shape selectivity by narrowing surface pore openings and eliminating surface active sites; however, they also result in pore blockage and/or increased internal diffusion resistance due to pore mouth narrowing, which reduce molecular flux during sorption and separations and decrease catalytic activity.[59]

The aforementioned side effects of zeolite passivation can be circumvented by growing an epitaxial zeolite shell on the surface of a zeolite core with identical or congruent structure. Synthesis of core-shell (or layered) structures has been demonstrated for a wide range of inorganic and organic materials[60] with applications ranging from semiconductors[61-62] and drug delivery[63] to catalysis[64-65] and separations.[66] A key factor in the fabrication of zeolite core-shell composite structures is sufficient compatibility between core and shell in terms of framework composition, crystal structure, and synthesis conditions required to facilitate oriented or epitaxial growth of one crystal on the surface of another.[67] In the literature, many combinations of core-shell zeolites are reported, such as LTA@FAU,[68] SOD@CAN,[69] FAU@BEA,[70] MOR@MFI,[71] MFI@BEA,[72] and BEA@MFI.[73-74] These materials can be formed through heterogeneous nucleation and growth of the shell on the core. Alternatively, the shell layer can be formed through the use of nanocrystalline seeds that are first deposited on the core

surface and then transformed into a contiguous layer via secondary growth.[75-76] One disadvantage of the latter approach is the need to calcine the seeded cores prior to shell growth in order to firmly fix the seeds to the core surface – a process that can introduce defects at the core/shell boundary.[77]

Herein, we focus on the formation of an MFI@MFI core-shell zeolite comprised of an aluminosilicate ZSM-5 (catalytically active) core and a silicalite-1 (catalytically benign) shell, both of which possess the same MFI crystal structure. Prior attempts to passivate MFI zeolite have resulted in incomplete silicalite-1 coverage, misaligned (non-epitaxial) shell growth, and/or individual silicalite-1 particles adhered to ZSM-5 seeds.[78-80] Core-shell MFI has been prepared by a one-step procedure using fluoride growth media;[81] however, the silicalite-1 shell thickness typically exceeds 1 μm and fluoride-based protocols are commercially restrictive. Prior examples have shown that MFI core-shell structures can improve catalyst selectivity, but often at the expense of reduced catalytic activity due to pore blockage or narrowing.[77] Moreover, structural mismatch between the core and shell can introduce molecular diffusion barriers that facilitate carbonaceous coke buildup.[82] Here, we report a robust protocol for realizing nanocrystalline ZSM-5@silicalite-1 with an ultrathin (< 10 nm), epitaxial silicalite-1 shell of tunable thickness. Performance tests using model reactions show that the shell layer preserves catalytic activity, thus avoiding pore blockage/narrowing and validating the overall effectiveness of this approach for zeolite design.

3.2 Results and discussion

3.2.1 Preparation of ZSM-5@silicalite-1

ZSM-5 and its purely-siliceous analogue silicalite-1 have an identical crystal structure (MFI type) comprised of 3-dimensional channels (ca. 5.5 Å diameter). ZSM-5 was synthesized according to a procedure reported by Persson et al.[83] with slight modifications. We prepared ZSM-5 crystals with a Si/Al molar ratio of 44, which was confirmed by inductively coupled plasma atomic emission spectroscopy (ICP-AES, Galbraith Labs). The crystal size was measured by dynamic light scattering (DLS) and electron microscopy. DLS analysis of a suspension of crystallites in aqueous solution revealed a relatively monodisperse distribution of crystals with a 156 nm average hydrodynamic diameter. Scanning electron microscopy (SEM) images of ZSM-5 confirmed their average size and size distribution (Figure 3.1A). High magnification SEM images (inset) revealed that crystals have rough surfaces comprised of spheroidal protrusions. ZSM-5 and other zeolites grow by non-classical routes[84-85] involving the aggregation of amorphous precursors. For instance, Subotić and coworkers[86-87] suggest that ZSM-5 crystallization proceeds via a complex series of pathways involving (i) precursor aggregation, (ii) precursor disorder-to-order transitions, (iii) aggregate growth and coarsening, and (iv) densification of aggregates. Increased synthesis time often leads to "annealing" by Ostwald ripening to form crystals with smooth surfaces. If syntheses are performed at low temperatures where the timescales for coarsening are sufficiently long, the final crystal is typically rough. There are many examples of highly corrugated crystals similar to the ones shown in Figure 3.1 where particles appear to be fractal aggregates of smaller crystallites or have surfaces comprised of protrusions with

dimensions spanning 5 to 20 nm. Notable examples include the syntheses of LTA (zeolite A), FAU (zeolite X), and MFI (silicalite-1).[88-91]

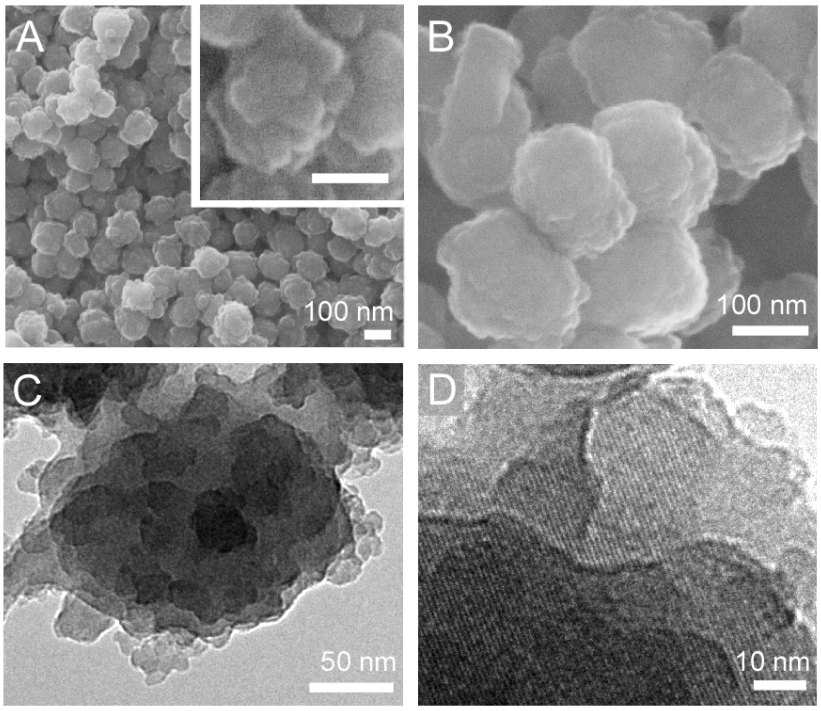

Figure 3.1 Electron microscopy images of ZSM-5 (core) and ZSM-5@silicalite-1 (core-shell) crystals prepared without thermal annealing. (A) SEM image of ZSM-5 crystals prepared at 100 °C for 60 h (inset scale bar = 100 nm). (B) SEM image of ZSM-5@silicalite-1 prepared with a 10 nm thick shell. (C) TEM image of a core-shell particle. (D) HRTEM image of the core-shell particle reveals the presence of lattice fringes with translation symmetry extending from the exterior to the interior of the crystal.

An epitaxial layer of silicalite-1 was grown on ZSM-5 by seeded growth. During the synthesis of ZSM-5 seeds, the crystals were isolated by centrifugation and washed with deionized (DI) water to remove the supernatant. The crystals were then transferred as a gel (without drying) to a silicalite-1 growth solution. We used the gel transfer procedure to minimize ZSM-5 crystal aggregation and to prevent the potential alteration of its exterior surface that may occur upon drying. The silicalite-1 growth solution was

prepared with tetraethylorthosilicate (TEOS) as the silica source and tetrapropylammonium (TPA^+) as an organic structure-directing agent (OSDA) to facilitate the formation of the MFI structure. We used a low supersaturated silica solution with molar composition *x* TEOS:14 TPAOH:9500 H_2O (with $x = 17 – 40$). The rationale for selecting a dilute concentration of silica was to minimize the homogeneous nucleation of silicalite-1, as well as achieve ultrathin (nanometer thick) silicalite-1 layers on the surface of ZSM-5 seeds. The silicalite-1 shell thickness was quantified by light scattering and electron microscopy. DLS measurements revealed that the hydrodynamic diameter increased by 10 nm or more depending on the TEOS concentration. The autocorrelation functions in DLS data showed no evidence of a bimodal size distribution that would be indicative of homogeneous silicalite-1 nucleation. SEM images of the core-shell particles (Figure 3.1B) revealed larger particles on average compared to the original seeds. Transmission electron microscopy (TEM) images indicated that the core-shell particles were rough (Figure 3.1C) with protrusions similar to those of the ZSM-5 core. High resolution TEM (HRTEM) revealed the presence of lattice fringes on the exterior surface (Figure 3.1D) with the same orientation as the particle interior, suggesting the shell formed via epitaxial growth of silicalite-1 on ZSM-5.

Rough surfaces impose challenges for the analysis of shell growth and the characterization of silicalite-1 uniformity on ZSM-5 crystals. In order to obtain definitive proof of a continuous epitaxial layer of silicalite-1, we prepared spheroidal ZSM-5 crystals with smoother surfaces that were more straightforward to characterize by scattering and microscopy techniques. This was accomplished by introducing an annealing step in the previous synthesis protocol. Following the completion of ZSM-5

crystallization, the gel product was transferred to a solution with molar composition 10 TEOS:14 TPAOH:9500 H_2O (with 1 wt% solid content) and was heated at 170 °C for 12 days. For this step, we selected a silica concentration that was approximately equal to the solubility of silicalite-1 in order to minimize ZSM-5 dissolution and prevent silicalite-1 crystallization. During hydrothermal annealing, protrusions on the exterior surfaces of ZSM-5 seed crystals coarsened, most likely as a result of Ostwald ripening, to produce crystals with smoother surfaces (Figure 3.2A). The annealed ZSM-5 seeds were then used to prepare ZSM-5@silicalite-1. Electron micrographs of the core-shell particles revealed a spheroidal morphology (Figure 3.2B) and showed no evidence of protrusions on their exterior surfaces (Figure 3.2C).

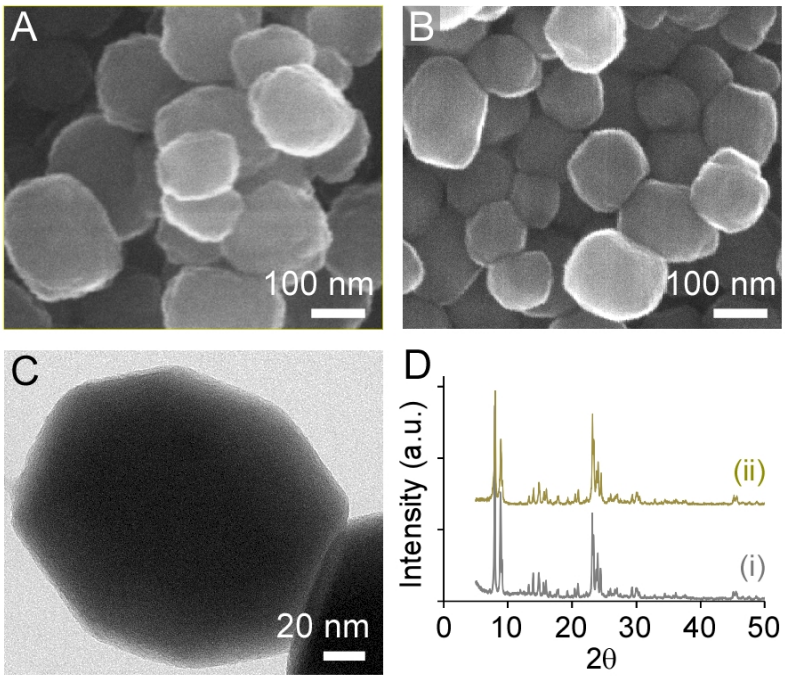

Figure 3.2 (A) SEM image of ZSM-5 crystals after 170 °C annealing for 12 days. (B) SEM image of ZSM-5@silicalite-1 crystals after the growth of a 10 nm silicalite-1 layer and an additional 12 days of annealing at 170 °C. (C) TEM image of ZSM-5@silicalite-1 reveals crystals with smoother surfaces. (D) Powder XRD patterns of annealed (i) ZSM-5 and (ii) ZSM-5@silicalite-1.

Powder X-ray diffraction (XRD) patterns of ZSM-5 (core) and ZSM-5@silicalite-1 (core-shell) confirmed that the products were fully crystalline (Figure 3.2D), i.e., an amorphous peak in the region $2\theta = 20 - 30^{o}$ was not observed in either the core or core-shell XRD patterns. ICP-AES analysis revealed Si/Al molar ratios of 44 and 53 for the core and core-shell samples, respectively. These results confirmed the expected increase in Si content due to shell growth. Moreover, N_2 adsorption measurements revealed that the BET surface area of ZSM-5 crystals (475 m^2/g) was approximately equal to the ZSM-5@silicalite-1 core-shell particles (454 m^2/g). These studies indicate that the silica layer on the surface of ZSM-5 is crystalline and that shell formation does not result in appreciable pore blockage (i.e., the undesired outcome of many previously reported surface passivation techniques).

3.2.2 Validation of the silicalite-1 shell structure

In order to confirm that the silica shell was a continuous epitaxial layer of silicalite-1, we used a combination of energy filtered transmission electron microscopy (EFTEM), electron dispersive spectroscopy (EDS), HRTEM, X-ray photoelectron spectroscopy (XPS), and catalytic testing with two probe reactions. EFTEM revealed the presence of a silica layer surrounding the ZSM-5 core with an approximately uniform thickness of ca. 10 nm (Figure 3.3A). The ZSM-5 core in EFTEM mappings appears to be yellow due to the superposition of Si (green) and Al (red) elements. Conversely, the exterior of the particle is green due to the presence of a Si-rich shell. EDS line scans along the cross-sections of both core and core-shell particles reveal that Al is contained only within the core of ZSM-5@silicalite-1 (see Figure A7 in Appendix A). HRTEM analysis of these particles shows the presence of lattice fringes (Figure 3.3B) and the translational

symmetry of pores between the core and shell, as determined by the continuous orientation of lattice fringes without any apparent discontinuity at the core/shell interface. The continuous channels, which span from one end of the core-shell particle to the other, permit unhindered access of ions and molecules to diffuse within the 3D porous network of the MFI framework.

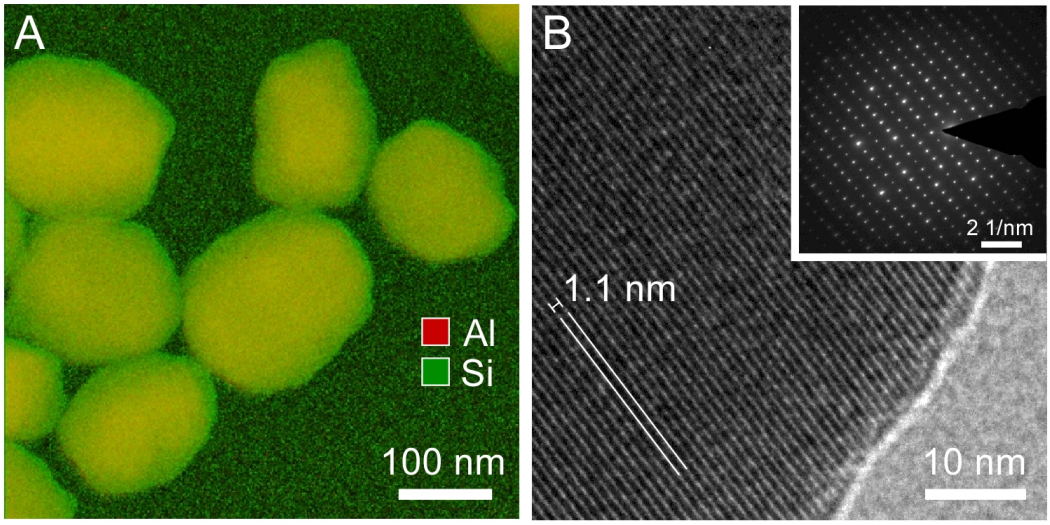

Figure 3.3 (A) Superimposed EFTEM mapping of annealed ZSM-5@silicalite-1 crystals prepared with a 10 nm silicalite-1 shell. The elements are color coded: Al (red) and Si (green). (B) HRTEM image of a core-shell crystal reveals the presence of lattice fringes that extend from the exterior to the interior of the particle without any discontinuity. The orientation of fringes (1.1 nm periodicity) is highlighted by the white lines. Inset: SAED pattern of core-shell reveals a single crystal.

The formation of a thin silicalite-1 shell was confirmed by a combination of analytical techniques, summarized in Table 3.1. Calcined ZSM-5 and ZSM-5@silicalite-1 samples were activated to their proton forms (H-zeolites) prior to XPS and catalytic studies. XPS results indicate a significant increase in the Si/Al ratio after growth of the silicalite-1 shell. The fact that the Si/Al ratio of the ZSM-5@silicalite-1 sample significantly

increases, but is still a finite value, indicates that the shell formed is very thin due to the short sampling depth of XPS (i.e., on the order of nanometers). Comparison of the Si/Al ratios of ZSM-5 core particles reveals slight differences between ICP-AES and XPS. The Si/Al ratio provided by the latter is biased to the elemental composition near the exterior of the particle, whereas ICP-AES provides a bulk average elemental analysis. The lower Si/Al ratio from XPS measurements suggests the potential for so-called "Al zoning" – a common phenomenon in ZSM-5 synthesis wherein crystallization leads to a Si/Al gradient that decreases in magnitude from the particle interior to its exterior.[92] It is important to point out, however, that high uncertainty in Si/Al ratios determined by XPS analysis have been reported in the literature for zeolites with low Al content such as these. Uncertainties in the Si/Al ratio as high as ±6 have been reported for zeolites with comparable Al content.[93] Other reports tend to use only qualitative comparisons when analyzing XPS data of zeolites with low elemental percentages of Al.[94] To this end, the quantitative degree of zoning in core (ZSM-5) particles cannot be conclusively determined from the XPS data.

Table 3.1 Si/Al ratios for H-ZSM-5 (core) and H-ZSM-5@silicalite-1 (core-shell).

	Si/Al ratio	
Technique	Core	Core-shell
XPS[a]	39	82
ICP-AES[a]	44	53
IPA-TPD[ab]	45 ± 1	51 ± 2

[a] Experiments performed on H-form zeolites. The XPS and IPA-TPD results were provided by our collaborator, Prof. Crossley, and his group.

[b] A 10% weight loss attributed to moisture within the zeolite during pretreatment is considered. Extra-framework Al estimated from ^{27}Al NMR (Table A1) is also included in the Si/Al ratio.

Techniques such as temperature programmed desorption (TPD) and ^{27}Al NMR provide additional means of analyzing the Al content in zeolite particles. The temperature programmed desorption of isopropylamine (IPA-TPD) measures the Brønsted acid sites, which directly correlate with the tetrahedral (or framework) Al content in H-zeolites.[95-96] The extra-framework Al was quantified by ^{27}Al NMR (Figure 3.4) to be 9.1% for the core and 5.1% for core-shell, both of which are significantly lower than the percentages reported for commercial MFI catalysts (i.e., values can reach as high as 25%).[97-98]

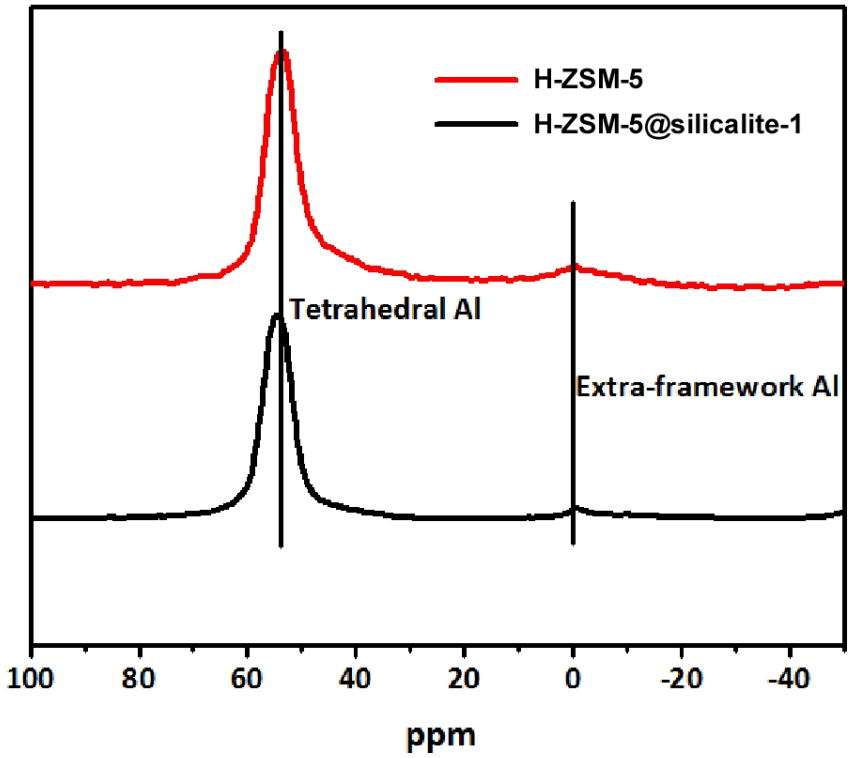

Figure 3.4 ^{27}Al NMR spectra of H-ZSM-5 (core) and H-ZSM-5@silicalite-1 (core-shell). The intensities at 60 ppm and 0 ppm correspond to framework and extra-framework alumina, respectively. The ^{27}Al NMR results were provided by our collaborator, Prof. Crossley, and his group.

Two probe chemical reactions were used to confirm the surface passivation of H-ZSM-5 and the unhindered access to Brønsted acid sites within H-ZSM-5@silicalite-1.

Triisopropylbenzene (TIPB) is a bulky molecule with three reactive isopropyl groups and a kinetic diameter of 8.5 Å, which is larger than the pores of MFI (5.5 Å). This limits the reactivity of TIPB to the external surface of the zeolite.[99-101] The second probe molecule selected for this study was acetic acid, which reacts via decarboxylative ketonization over Brønsted sites in zeolites to produce acetone.[102] The kinetic diameters of acetic acid and the reaction products (acetone, CO_2 and H_2O) are small enough to diffuse through the micropores of MFI. Figure 3.5A shows a dramatic reduction in the reactivity of TIPB over H-ZSM-5@silicalite-1 when compared to H-ZSM-5. On an equivalent acid site basis, the surface activity is limited to less than 6% of the activity of the parent zeolite, indicating a near complete silicalite-1 coating on H-ZSM-5. The removal of external surface Brønsted acid sites in H-ZSM-5@silicalite-1 was also demonstrated by infrared (IR) spectroscopy of an adsorbed bulky pyridine, di-tertbutyl pyridine (see Figure A4 of Appendix A). A signal at 1616 cm^{-1}, corresponding to protonation of di-tertbutyl pyridine,[103-104] is observed for the core, with little to no peak in this region for the core-shell sample, indicating the absence of external Brønsted acid sites. The rate of acetic acid conversion normalized per total acid site, as shown in Figure 3.5B, is identical for the samples with and without a silicalite-1 shell. The rate of catalyst deactivation as a function of time is identical for both catalysts as well. This identical catalytic activity after incorporating the silicalite-1 shell demonstrates that the internal acid sites are accessible for this reaction, which is consistent with the results from HRTEM and BET analysis. This finding also confirms our ability to passivate ZSM-5 surfaces without hindering the intrinsic activity of the catalyst, which is a significant advancement in zeolite core-shell design.

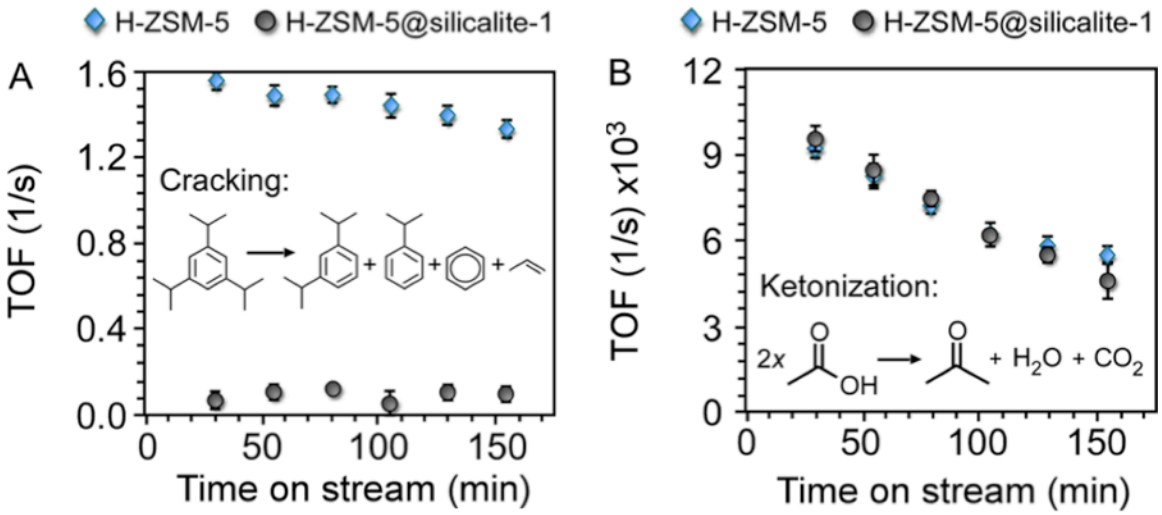

Figure 3.5 Gas phase turnover frequency (TOF) in a flow reactor of (A) triisopropylbenzene and (B) acetic acid over H-ZSM-5@silicalite-1 prepared with a 10 nm silicalite-1 shell, as well as the H-ZSM-5 core. Details of the reactions are provided in chapter 2. The probe reaction results were provided by our collaborator, Prof. Crossley, and his group.

3.2.3 Tailoring the silicalite-1 shell thickness

We investigated two approaches to tune the shell thickness. The synthesis can either be quenched at a specific time of hydrothermal treatment to achieve the desired thickness (leaving a fraction of unreacted silica in the growth solution), or an exact concentration of TEOS can be selected such that shell growth is terminated once the solution reaches thermodynamic equilibrium (i.e., silicalite-1 solubility). We carried out the first approach and monitored the rate of shell growth using ex situ DLS measurements of ZSM-5@silicalite-1 particles that were heated for various times in a silicalite-1 growth solution. In order to measure shell growth over a reasonable timescale, we used a silicalite-1 growth solution with lower pH (molar composition 14 TEOS:7 TPAOH: 9500 H_2O), which increases the rate of crystallization. As shown in Figure 3.6, DLS

measurements revealed a monotonic increase in the hydrodynamic diameter of ZSM-5@silicalite-1 with heating time. The linear rate of silicalite-1 growth is consistent with trends in the literature.[105] The measured growth rate of 3.8 nm/h (i.e., change in hydrodynamic diameter with time) is approximately equal to the 4.0 nm/h value reported by Li et al.[106] in their study of silicalite-1 growth at similar conditions.

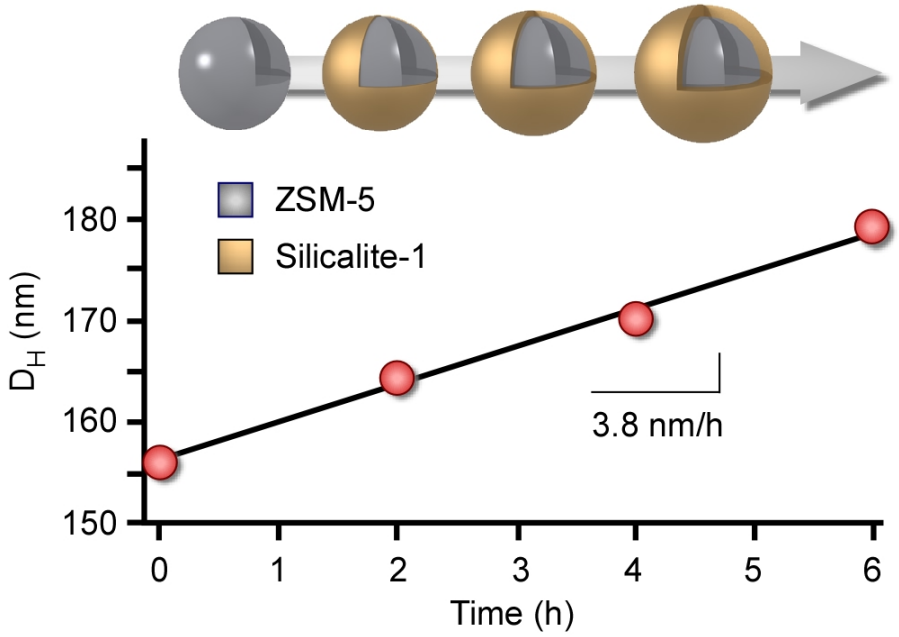

Figure 3.6 Ex situ DLS measurements of ZSM-5@silicalite-1 growth. The symbols are an average of three measurements with standard deviation of ± 2 nm (less than the size of the symbols).

CONTIN analysis[107-108] of the DLS autocorrelation functions revealed a single particle size distribution for all extracted samples, which suggests that homogeneous silicalite-1 nucleation and crystal growth is negligible. Indeed, if the latter were to occur with any appreciable frequency, we would anticipate the presence of a bimodal size distribution. The absence of a smaller particle size population in the DLS data suggests that ZSM-5@silicalite-1 growth is the dominant pathway.

A disadvantage of the previous approach is that silicalite-1 growth is terminated prior to reaching silicalite-1 solubility. As such, TEOS is wasted in this process and the extraction of crystals from the supernatant could lead to the potential deposition of amorphous silica from solution to the exterior surfaces of ZSM-5@silicalite-1 (thereby leading to pore blockage). An alternative, and more practical approach, is to select the exact amount of TEOS needed to achieve the desired thickness, such that silicalite-1 growth is terminated once equilibrium is reached. The ability to control the thickness of the silicalite-1 shell, however, requires knowledge of solution chemistry and the approximate solubility of MFI crystals. Prior studies have shown that silicalite-1 growth solutions prepared with TEOS are comprised of silica nanoparticle precursors (1 – 6 nm) that self-assemble at a critical aggregation concentration (CAC), which is defined by the silica concentration at a 1:1 molar ratio of *x* TEOS:*y* TPAOH.[109-110] The kinetic phase diagram for silicalite-1 growth solutions depicted in Figure 3.7A reveals the presence of two distinct regions divided by the CAC (solid line). Region I ($x/y < 1$) consists of soluble silica species (i.e., silicic acid and silica oligomers), while region II ($x/y > 1$) consists of silica molecules in quasi-equilibrium with silica nanoparticles. There have been many studies that focused on characterizing the physicochemical properties of silica nanoparticles and identifying their putative role(s) in silicalite-1 crystallization.[111-115] During the course of silicalite-1 crystallization, silica molecules and nanoparticles in the growth solution are progressively consumed, resulting in a temporal shift from right to left along the dashed line in Figure 3.7A. The final stage of silicalite-1 growth involves an exothermic-to-endothermic transition in the heat of crystallization when crossing the CAC that is accompanied by an increase in pH.[116] Crystal growth is complete once the

concentration of silica in solution reaches the thermodynamic solubility of silicalite-1 (estimated as the dotted line in Figure 3.7A).

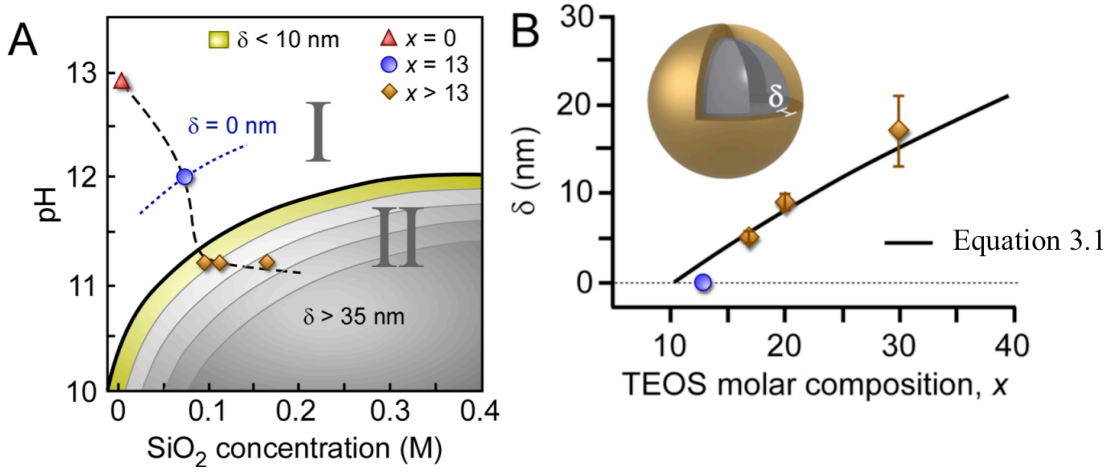

Figure 3.7 (A) The kinetic phase diagram of silicalite-1 growth solutions. The pH was measured for solutions of molar composition x TEOS:14 TPAOH: 9500 H_2O where $x > 13$ (orange diamonds) was used for shell growth, $x = 13$ (blue circle) is an estimate of the silicalite-1 solubility c_e, and $x = 0$ (red triangle) is a silica-free solution. The dashed line is interpolated between experimental data points. The color-coded segments in Region II illustrate the progressive increase in δ with increased silica supersaturation. (B) The shell thickness of ZSM-5@silicalite-1 can be tailored by adjusting the molar composition of TEOS. Growth solutions with ZSM-5 crystals (0.01 g seeds per 1 g solution) were heated for 24 hours at 100 °C, followed by 12 days of annealing at 170 °C. The solid line corresponds to equation (3.1) where $c_e = 0.06$ M ($x \approx 10$) and $x/c = 171\ L\ mol^{-1}$. Data points are the average of 3 measurements and error bars equal two standard deviations.

The design of ZSM-5@silicalite-1 must take into account the relative concentrations of ZSM-5 seeds and TEOS. We used a concentration of 2.5×10^{15} seeds/L growth solution (i.e., N = 6.3×10^{13} seeds). If the concentration of seeds is sufficiently low, there is a higher probability of silicalite-1 nucleation and growth occurring in solution rather than on the surface of ZSM-5 seeds. This would lead to a mixture of ZSM-5, silicalite-1, and/or ZSM-5@silicalite-1 crystals in the final product. There is evidence in the

literature[117] that suggests silicalite-1 crystallites can attach to the surface of ZSM-5 crystals, thus generating fractal aggregates as opposed to a continuous epitaxial silicalite-1 shell. Depending on the size of silicalite-1 crystals and their coverage on ZSM-5 surfaces, these layers may appear to be a uniform shell that would go undetected by cursory inspection using bulk characterization techniques such as DLS or SEM, whereas higher resolution techniques, such as TEM, are capable of discerning these differences.

The preparation of ZSM-5@silicalite-1 with predictable shell thickness also requires the selection of an appropriate silica supersaturation. To this end, we prepared several growth solutions of varying silica concentration and measured the resulting shell thickness δ (Figure 3.7B). For these studies we used 0.09 – 0.2 M SiO_2 to adjust δ between 5 and 30 nm. We observed a monotonic increase in δ with silica concentration that enables the silicalite-1 layer to be selectively tuned. Molecular layers of silica ($\delta < 2$ nm) can be achieved by working at lower silica concentrations; however, for the purpose of this study, we used an appreciable shell thickness (ca. 10 nm) in order to confirm silicalite-1 growth on ZSM-5 seeds. The shell thickness can be adjusted using equation (3.1) with the judicious selection of silica concentration c for seeded crystallization,

$$c(\delta, T, \mathrm{pH}) = \frac{4\pi N \rho_{SiO_2}}{3V M_{SiO_2}} \cdot ((R+\delta)^3 - R^3) + c_e(T, \mathrm{pH}). \quad (3.1)$$

The parameter R is the average radius of ZSM-5 seeds, N is the number of crystal seeds, ρ is density of silicalite-1, V is the total volume of the growth solution, M is molar mass of SiO_2, and c_e is the silica concentration at silicalite-1 solubility. The value of c_e establishes a lower limit of TEOS concentration for the preparation of ZSM-5@silicalite-1. When $c = c_e$ the solution is at equilibrium and there is no growth of silicalite-1 (i.e., $\delta = 0$ nm), whereas $c > c_e$ leads to the formation of a silicalite-1 shell. Without a priori

knowledge of c_e, we used this parameter to fit the experimental data in Figure 3.7B assuming 2.0 g/cm^3 as the silicalite-1 density and 78 nm as the average radius of ZSM-5 seeds. A value of c_e = 0.06 ± 0.01 M (Figure 3.7B, solid line) provided the best fit. To validate this estimate of c_e, we first measured the pH of a seeded growth solution after 24 hours of heating when the silicalite-1 shell was fully grown and the solution reached solubility. We then prepared non-seeded growth solutions by varying the molar composition x TEOS:14 TPAOH: 9500 H_2O until the seeded and non-seeded solutions had similar pH (11.8 and 12.0, respectively). This occurred at x = 13 or c_e = 0.07 M SiO_2 (Figure 3.7, blue circles), which is comparable to the silicalite-1 solubility from equation (3.1).

3.3 Conclusions

In summary, we have demonstrated an ability to synthesize a core-shell zeolite with compositionally distinct, but structurally identical domains. For this study we selected the MFI framework structure, which is one of the most commercially relevant zeolites in heterogeneous catalysis. Using a broad combination of experimental techniques, we have shown that ZSM-5@silicalite-1 can be prepared with tunable shell thickness. Electron microscopy and textural analysis confirmed that silicalite-1 forms an epitaxial layer on ZSM-5 crystals without blocking pore openings. SEM and DLS were used in combination to confirm that the shell thickness can be tailored with nanometer resolution. XPS, EDS, and TPD measurements revealed the presence of a siliceous shell, while probe reactions using molecules that were either too large or adequately sized to access MFI pores confirmed the uniform shell coverage. Moreover, these studies revealed that the activity of ZSM-5 catalysts is not compromised by the overgrowth of a passivation

layer. This finding highlights a distinct advantage of our synthetic protocol relative to alternative techniques that have been used to passivate zeolite surfaces.

The synthesis of ZSM-5@silicalite-1 offers a pathway for tuning the physicochemical properties of MFI-type materials. The generation of passivation layers is particularly beneficial for heterogeneous catalysis where the inactive shell enhances product selectivity. Knowledge of solution chemistry for aluminosilicate zeolites and their siliceous analogues affords the opportunity to selectively design novel materials with tailored properties. To this end, the method described here may prove to be a general platform for core-shell design that could potentially be applied to other zeolite frameworks structures.

Chapter 4 Periodic, vdW-corrected density functional theory investigation of the effect of Al siting in H-ZSM-5 on chemisorption properties and site-specific acidity

The material discussed in this chapter has been published. Figure and table numbers have been changed for dissertation consistency.

4.1 Introduction

Zeolites are versatile materials with the broadest range of applications among heterogeneous catalysts.[118] The activity of these aluminosilicates in catalytic processes is attributed to their acidity, which derives from the replacement of a silicon atom at a tetrahedral site (T site) in the zeolite framework with an aluminum atom. Properties of these acid sites and their respective influence on catalytic activity are of great interest and have been investigated both experimentally and theoretically. To further improve zeolite catalyst performance and enable the design of zeolites with specific properties, a fundamental understanding of the active sites and reliable theoretical methods for the prediction of zeolite functionality are needed.

Theoretical simulations of zeolites have been carried out for more than two decades through force-field approaches and quantum mechanical methods. Among the latter, density functional theory (DFT) has gained significant attention, especially due to its applicability to chemical reactions (contrary to force-field approaches) and its lower computational cost compared to other higher order ab-initio methods, such as MP2 (second-order Møller-Plesset perturbation theory).[119] However, the typically complex structure of zeolite crystals, which are comprised of unit cells containing as many as hundreds of atoms in a 3-dimensional (3D) configuration, imposes many challenges for

modeling. The unit cell of siliceous MFI (termed H-ZSM-5 in its acidic aluminosilicate form) is composed of 96 T atoms (Si or Al) and 192 oxygen atoms, with a 3D pore network exhibiting two types of interconnected channels, straight channels oriented along the b direction and sinusoidal channels oriented along the a direction (see Figure 4.1). When creating an acid site in an MFI orthorhombic unit cell model, there are 12 geometrically distinguishable T site locations that can be occupied by Al.

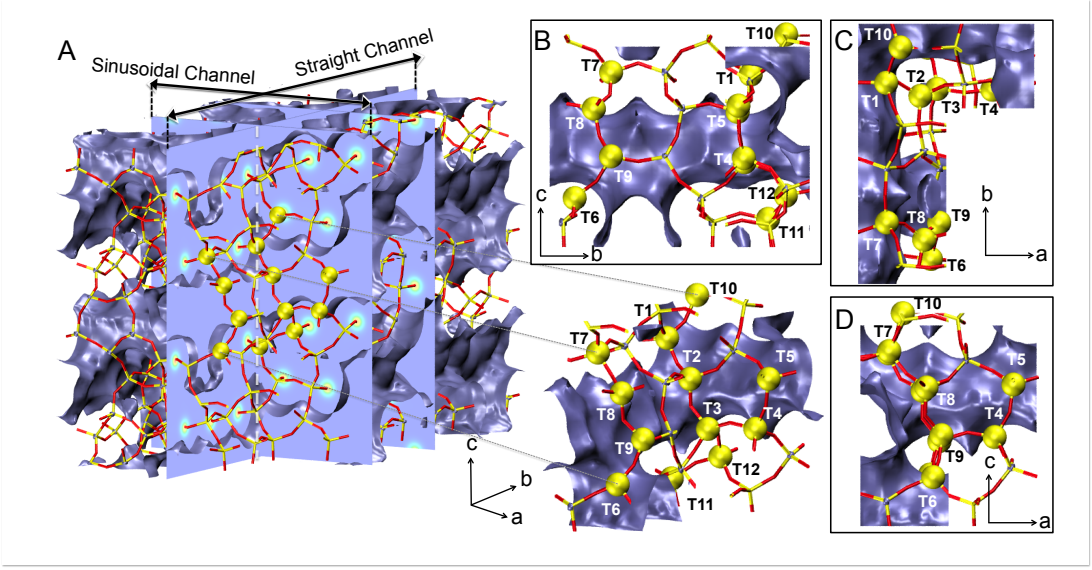

Figure 4.1 (A) 3-dimensional (3D) overview of the MFI framework (Si – yellow, O – red). The sinusoidal channel along the a direction and the straight channel along the b direction are approximated by an isosurface (purple) of the calculated charge density at 0.004 e/Å^3. The two parallel planes along the a direction cut through the center of two adjacent sinusoidal channels. The plane parallel to the b direction cuts through the center of a straight channel. All 12 crystallographically distinct T sites are marked in the enlarged version of the 3D representation and in the corresponding 2D projections in all three directions (panels B-D).

Early modeling efforts used cluster models containing as little as 3 to 5 T sites to represent the active catalytic site.[119-122] The dangling bonds resulting from isolation of the

cluster from the remaining zeolite are saturated with hydrogen atoms. It is evident that this approach is not capable of mimicking the complex environment (i.e., confinement) of active sites and long-range interactions, e.g., the exclusion of van der Waals forces. With embedded cluster methods, such as ONIOM or QM/MM, more sophisticated zeolite framework models can be realized at significantly lower computational cost compared to full ab-initio techniques.[22, 123-126] However, embedded cluster models suffer from the strong sensitivity of adsorbate binding energies to the selected force-field and the difficult assignment of the QM/MM boundary.[127] The current availability of powerful computational resources, optimized DFT codes, and increasingly accurate exchange-correlation functionals permits fully periodic DFT simulations to be performed, even on large zeolite unit cells, which eliminates many of the shortcomings mentioned above. Nevertheless, in their careful review of periodic DFT simulations applied to catalytic reactions in zeolites, Hafner et al. emphasize the importance of dispersion forces and the challenge associated with selecting a proper exchange-correlation functional.[128]

In addition to the judicious selection of the simulation method, the location of the modeled acid site within a given zeolite structure must be carefully considered. As shown in Figure 4.1, a Brønsted acid (BA) site in H-ZSM-5 can be located at 12 distinguishable T sites. Prior studies that attempted to experimentally characterize Al siting in the MFI framework report disparate results,[19, 23, 129] and generally conclude that Al siting is highly sensitive to synthesis protocols.[23] This is consistent with calculated Al site stabilities reporting small variations of ca. 0.2 eV, which is approximately equal to the error of DFT simulations.[130] In efforts to avoid computational expense, theoretical investigations of H-ZSM-5 have often focused on specific T site locations, notably T7 and T12, as the most

representative active site model(s).[120, 124, 131-133] This selection is typically based on the relative stability of the site (i.e., T7) and/or its accessibility to reactants/adsorbates (i.e., T12), although other T sites have been modeled as well.[125] The heterogeneity of acid sites in zeolite frameworks, however, is an area of active debate.[128] Brändle and Sauer[131] used an embedded cluster approach to study the influence of crystal structure on BA site properties, and reported that the acidity assessed by the deprotonation energy can vary as much as 30 kJ/mol among four different zeolite framework types, including MFI. In contrast, an experimental study by Liu et al.[134] concluded that BA sites in zeolites with MFI and MWW structures exhibit similar behavior. Mihaleva et al.[135] reported significant variations in adsorption and acidity properties of two chabazite clusters of different shapes. Yang et al.,[136] Gounder and Iglesia,[98] and Chu et al.[137] have shown that location dependent confinement effects can alter the catalytic properties of acid sites. Evidently, a comprehensive investigation of the sensitivity of the catalytic properties of BA sites to their location within the zeolite crystal is needed. In the present study, we report structural, vibrational, and energetic properties of all 12 crystallographically distinguishable Al-substituted T sites of zeolite H-ZSM-5 using thorough periodic DFT simulations and a dispersion-corrected functional (vdW-DF).[138-139] Particular attention is given to properties that have been suggested as a measure of acid strength, including NH_3 and pyridine adsorption energy, O—H stretch frequency, O—H bond length, and the Si—OH—Al bond angle. Moreover, we also examined the adsorption of CO, CH_4, and CH_3OH given their relevance to many zeolite catalyzed reactions. An improved understanding of the influence of Al siting combined with novel characterization and synthesis methods that allow for controlled placement of Al atoms in a zeolite framework

have the potential to impact the design of tailored zeolites with improved catalytic properties.

4.2 Computational methods

All DFT calculations were performed using the Atomic Simulation Environment (ASE),[140] the Vienna ab-initio simulation package (VASP),[42, 141] and the projector-augmented wave (PAW) method. For benchmarking purposes, the PBE, RPBE, PW91, DFT-D2,[36] and the vdW-DF[138-139] exchange-correlation functionals were employed. Conclusions regarding the properties of individual T sites are based on results obtained from the vdW-DF functional, which was identified as the most accurate functional that self-consistently accounts for van der Waals (vdW) interactions, in contrast to the semi-empirical DFT-D type functionals by Grimme.[36, 142] Periodic boundary conditions in all three directions of the MFI unit cell were employed with the plane-wave kinetic energy cutoff set at 540 eV. Brillouin-zone sampling was restricted to the Γ-point and Gaussian smearing with k_bT = 0.1 eV was used. All atoms in the unit cell were relaxed and the convergence criterion for the net force on each atom was 0.02 eV/Å. The optimized lattice constants of the siliceous MFI unit cell are a = 20.29 Å, b = 19.94 Å, c = 13.27 Å, which are ca. 1% larger than experimental reference values.[143] The same lattice parameters were used for calculations with one Al substitution per unit cell (Si/Al = 95). Binding energies are reported as negative values for exothermic adsorption. VdW contributions were directly extracted from the VASP vdW-DF output, which tends to overestimate the relative contribution of the vdW forces. Vibrational frequencies were obtained in the harmonic oscillator approximation with a displacement of 0.01 Å.

4.3 Results and discussion

4.3.1 Benchmark data

Our benchmark studies of several well known exchange-correlation functionals were performed by comparing chemisorption energies on 3T zeolite cluster models (two Si atoms and one Al atom) with benchmark data from high level calculations[122] and evaluation of the siliceous MFI unit cell constants. The interactions of this cluster with probe molecules CH_4, C_2H_4, C_2H_6, and H_2O were studied by Zhao and Truhlar[122] using several density functional methods. Their data were compared with the second-order Møller-Plesset perturbation theory (MP2) result as the best estimate. The same approach was followed in this study. Adsorption energies are reported as negative values for exothermic adsorption steps. DFT simulations were carried out using the Vienna ab-initio simulation package (VASP).[42, 141, 144-145] Here, we tested the PBE,[146] RPBE,[147] PW91,[148] DFT-D2,[36] and vdW-DF[138-139] exchange-correlation functionals. The results are shown in Table 4.1. The energy of adsorption of CO is also included, and is compared to the theoretical value calculated for a 2T cluster with the MP2 method reported by Civalleri et al.[149]

As accuracy criterion we used the mean absolute error (MAE) for each functional, which was calculated as the average absolute error between our calculated adsorption energy and the best estimate value reported for CH_4, C_2H_6, C_2H_4, C_2H_4-alkoxide, and H_2O by Zhao and Truhlar[122] or for CO by Civalleri et al.[149] The lowest MAE value of 0.06 eV is obtained for the self-consistent vdW-DF exchange-correlation functional, suggesting that it has a similar accuracy for binding energy calculations as the MP2 level of theory.

Table 4.1 Energy of adsorption of several probe molecules on a 3T cluster model calculated with various exchange-correlation functionals and VASP against best estimates from Zhao and Truhlar[122] and Civalleri et al.,[149] along with mean absolute errors (all energy values are in eV).

Complex	PBE	RPBE	PW91	DFT-D2	vdW-DF	Best estimate
HZ…CH_4	-0.10	-0.02	-0.11	-0.17	-0.14	-0.15
HZ…C_2H_6	-0.05	-0.03	-0.08	-0.10	-0.12	-0.19
HZ…C_2H_4	-0.29	-0.18	-0.30	-0.39	-0.37	-0.34
HZ…C_2H_4alkoxide	-0.78	-0.54	-0.79	-0.95	-0.86	-0.85
HZ…H_2O	-0.83	-0.63	-0.86	-0.93	-0.81	-0.65
HZ…CO	-0.18	-0.08	-0.20	-0.22	-0.17	-0.22
Mean absolute error	0.09	0.15	0.08	0.09	0.06	_

Lattice constants of the siliceous MFI unit cell were optimized (Table 4.2) and the results were compared to reference values,[143] i.e.: a = 20.09 Å, b = 19.74 Å, c = 13.14 Å where each number within parentheses in Table 4.2 represents the percent error of the lattice constant relative to the corresponding reference value. All the functionals except RPBE result in an approximately 1% relative error for each lattice constant. While RPBE predicts the most accurate lattice constants, it has the largest MAE in our adsorption energy calculations. Therefore, RPBE is not an appropriate choice for our computations. Overall, vdW-DF yields the smallest MAE with an acceptable lattice constant error. To

this end, we selected vdW-DF as the exchange-correlation functional to be applied to the rest of our calculations.

Table 4.2 MFI lattice constants optimized with various exchange-correlation functionals and VASP.[a]

Lattice constants (Å)	**PBE**	**RPBE**	**PW91**	**DFT-D2**	**vdW-DF**
a	20.29 (1.0)	20.11 (0.1)	20.28 (0.9)	20.26 (0.9)	20.29 (1.0)
b	19.93 (1.0)	19.73 (0.0)	19.92 (0.9)	19.91 (0.9)	19.94 (1.0)
c	13.27 (1.0)	13.22 (0.6)	13.26 (0.9)	13.25 (0.9)	13.27 (1.0)

[a] Numbers within parentheses represent percent errors (%) relative to the corresponding reference values.

4.3.2 Site-specific properties

To investigate site-specific properties, we first substituted Al in all 12 distinct T site locations of MFI and considered each of the four neighboring oxygen atoms as possible binding sites for the BA proton. The most stable arrangement for each T site substitution was chosen for vibrational analysis and adsorption calculations unless the resulting BA proton was inaccessible to adsorbates due to steric hindrance. In latter cases, the next most energetically stable (and accessible) BA site was selected, which imparted an energy penalty of less than 0.2 eV. The exact proton location clearly increases the complexity of creating computational models, but in practice the proton is frequently exchanged with the adsorbed intermediate(s) and can easily change between the accessible O atoms around a given Al atom during catalytic turnover. Its exact location is therefore of lesser importance in catalytic applications than the Al siting. Table 4.3 lists

the relative stabilities, vibrational frequencies, and geometrical properties for all 12 distinct BA sites (the maximum and minimum values of each column are bolded).

Table 4.3 Properties of different Al-substituted T sites in H-ZSM-5.

Active site identifier[a]	Location[b]	Stability[c] (eV)	O—H frequency (cm^{-1})	O—H frequency shift[d] (cm^{-1})	O—H bond length (Å)	Si—OH—Al bond angle
1—2	intersection	0.26	**3723**	-321	**0.976**	**127.8**
2—1	intersection	0.28	3716	-331	**0.976**	128.9
3—4	intersection	0.26	**3109**	-90	**1.005**	136.5
4—3	sinusoidal	0.10	3125	**13**	1.004	139.4
5—1	intersection	0.32	3654	**-367**	0.978	134.0
6—3	intersection	0.35	3128	3	**1.005**	139.4
7—8	intersection	**0.00**	3392	-75	0.991	129.3
8—7	straight	0.21	3368	-27	0.992	130.9
9—9	intersection	**0.38**	3666	-352	0.978	133.5
10—1	sinusoidal	0.17	3667	-291	0.978	134.7
11—5	straight	0.26	3362	-74	0.994	**140.4**
12—12	intersection	0.20	3671	-342	0.978	134.7

In the columns of Table 4.3, the leftmost number of each index, which is within the range 1 to 12, represents the T site that is occupied by aluminum, and the rightmost number refers to the silicon atom connected to the BA oxygen. Location determines the type of channel where a T site can be found; i.e., straight, sinusoidal, or intersection of both. Relative stabilities are reported with respect to the most stable T7 site. O—H

frequency shift represents the difference between the O—H stretch frequency of a CO-adsorbed BA site and that of the same adsorbate-free BA site.

In order to show the sensitivity towards the proton position around a specific T site, these properties were also calculated for the other three possible proton locations around the T12 site and the results are presented in Table 4.4. We observed only small variations in the relative stability; however, the O—H stretch frequency and Si—OH—Al bond angle span a notable range of values.

Table 4.4 Properties of all Al-substituted T12 sites in H-ZSM-5.

Active site identifier[a]	**Location**[b]	**Stability**[c] **(eV)**	**O—H frequency (cm^{-1})**	**O—H frequency shift**[d] **(cm^{-1})**	**O—H bond length (Å)**	**Si—OH—Al bond angle**
12—12	intersection	0.20	3671	-342	0.978	134.7
12—3	intersection	0.30	3661	-335	0.977	131.3
12—8	inaccessible	0.25	3166	_	1.003	139.0
12—11	intersection	0.34	3621	-287	0.981	137.5

Calculated O—H stretch frequencies shown in Table 4.3 can be grouped into three frequency ranges centered around 3720-3670, 3370, and 3120 cm^{-1}. Calculated O—H bond lengths are correlated with the corresponding frequency value and decrease as the stretch frequency increases. This observation can be rationalized by the explanation that stronger O—H bonds result in shorter bond lengths and a deeper potential energy well, leading to a larger curvature and higher frequencies in the harmonic oscillator approximation. Strong O—H bonds lower the ability of a BA site to donate a proton and imply a lower acid strength. Thus, BA sites in H-ZSM-5 exist in three different acid

strengths as judged by the three frequency groupings. Notable O—H frequency shifts upon CO adsorption are only found for acid sites in the 3720-3670 cm^{-1} group. On these sites CO adsorption lowers the O—H stretch frequency from 291 to 367 cm^{-1}, which is in good agreement with the experimentally determined shift of 310 cm^{-1}.[150] We did not observe correlations between the Si—OH—Al bond angles, O—H stretch frequency shifts, or O—H bond lengths.

To determine the preferred position of Al substitution, we first considered the thermodynamic stability of each substitution site; however, in agreement with Schröder et al., no significant thermodynamic preference was observed.[130] The least stable T9 site is 0.38 eV less stable than the most stable T7 site. This is consistent with experimental studies suggesting that Al siting is primarily determined by the synthesis conditions.[23] Hence, thermodynamic stabilities alone do not provide a satisfactory criterion for selecting an active site. The accessibility of T sites is often considered as an alternative criterion; however, 8 of the 12 T sites are easily accessible at the channel intersection, with the exception of T4 and T10 (sinusoidal), and T8 and T11 (straight). After using the observed CO frequency shift (-310 cm^{-1}) to narrow down the choice of T site substitution, there are still five site models at channel intersections remaining: T12 > T1, T2 > T5 > T9 (listed with decreasing stability). Clearly, on the basis of DFT results and structural considerations alone there is no unique choice for a representative BA site model in H-ZSM-5. Only detailed experimental characterization of H-ZSM-5 samples synthesized under various conditions and a better understanding of zeolite crystallization can further elucidate the preferred T site(s) for Al substitution.

Variations in catalytic activity of the 12 different BA sites are assessed through the binding energy (BE) of five probe molecules frequently used in zeolite characterization and/or catalytic reactions. The adsorption energy of basic ammonia and pyridine molecules is widely accepted as a measure of zeolite active site acidity.[151] Ammonia, methane, carbon monoxide, and methanol are common reactants for important catalytic applications, which include De-NO_x, syngas reactions, upgrade of natural gas, and methanol-to-gasoline or methanol-to-olefins (MTG or MTO). The strongest and weakest binding sites reported in Table 4.5 are labeled in bold to highlight the domain of binding strength variation for each molecule over different T sites.

Table 4.5 Binding energies of several probe molecules on potential active sites of H-ZSM-5.[a]

Active site identifier[b]	CH_4	NH_3	CO	C_5H_5N	CH_3OH
1—2	-0.49 (-0.02)	-1.45 (-0.98)	-0.63 (-0.22)	-2.02 (-0.16)	-1.19 (-0.53)
2—1	-0.48 (0.04)	-1.55 (-0.99)	-0.56 (-0.15)	**-1.94** (-0.05)	-1.13 (-0.55)
3—4	**-0.56** (0.04)	**-1.77** (-1.18)	-0.67 (-0.09)	-2.12 (-0.15)	-1.16 (-0.26)
4—3	-0.50 (0.08)	-1.57 (-0.94)	-0.55 (-0.01)	-2.09 (-0.11)	-1.24 (-0.30)
5—1	-0.48 (0.01)	-1.64 (-1.10)	-0.53 (-0.12)	**-2.56** (-1.03)	-1.13 (-0.49)

Table 4.5 (continued)

6—3	-0.49 (0.13)	**-1.31** (-0.69)	**-0.45** (0.08)	-2.22 (-0.39)	**-1.09** (-0.19)
7—8	**-0.40** (0.16)	-1.47 (-0.92)	-0.57 (-0.13)	-2.39 (-0.92)	-1.28 (-0.57)
8—7	**-0.40** (0.11)	-1.49 (-0.90)	-0.49 (-0.08)	-2.38 (-0.98)	-1.19 (-0.53)
9—9	-0.48 (0.04)	-1.64 (-1.12)	-0.59 (-0.16)	-2.42 (-0.86)	-1.34 (-0.63)
10—1	-0.50 (-0.02)	-1.54 (-0.99)	**-0.70** (-0.16)	-2.42 (-1.09)	-1.15 (-0.46)
11—5	-0.51 (0.11)	-1.62 (-1.03)	-0.55 (-0.07)	-2.52 (-0.63)	-1.19 (-0.37)
12—12	**-0.40** (0.01)	-1.63 (-1.12)	-0.62 (-0.13)	-2.32 (-0.50)	**-1.36** (-0.58)
Boltzmann average[c]	-0.40 (0.08)	-1.47 (-0.83)	-0.57 (0.03)	-2.39 (-0.18)	-1.28 (-0.22)
Standard deviation	0.05 (0.06)	0.11 (0.12)	0.07 (0.10)	0.19 (0.36)	0.08 (0.18)

[a] All energy values are in eV. Numbers within parentheses reflect chemisorption only, i.e., exclude vdW interactions.

[b] In each index of this column, the leftmost number, which is within the range 1 to 12, represents the T site that is occupied by aluminum, and the rightmost number refers to the silicon atom connected to the BA oxygen.

[c] The Boltzmann average is calculated assuming a Boltzmann distribution of binding energies weighted with the relative stability of the sites.

A comparison of the binding energies with and without vdW contributions clearly demonstrates the importance of including dispersion forces in zeolite models. For smaller adsorbates (i.e., CH_4, NH_3, and CO), the vdW contribution is about -0.5 eV, while this contribution for the larger molecules (i.e., C_5H_5N and CH_3OH) can be as large as -2.0 eV. The interactions of CH_4 and CO with H-ZSM-5 are dominated by vdW contributions, while marginal binding is observed in the absence of dispersion corrections. These remarkable differences can significantly alter both quantitative and qualitative conclusions from theoretical studies. While the relative vdW contributions may be overestimated, we note that the calculated absolute binding energies for NH_3 and pyridine are in good agreement with experimental data. Parrillo et al.[152] reported adsorption energies of -1.50 eV for NH_3 and -2.07 eV for pyridine, which is in good agreement with our Boltzmann averaged values of -1.47 eV and -2.39 eV calculated for NH_3 and pyridine, respectively.

The binding energies reported in Table 4.5 provide further support that not all T sites exhibit identical behavior. For instance, CH_4 and CO binding energies on all T sites vary by approximately 0.2 eV, CH_3OH and NH_3 by 0.3 – 0.4 eV, and pyridine by just over 0.5 eV. These variations are reflected in the standard deviations of 0.05 - 0.07 eV for CH_4 and CO, 0.10 eV for CH_3OH and NH_3, and 0.19 eV for pyridine. The sensitivity to zero point energy corrections was tested for CO and pyridine, but no significant effect was found, because the high frequencies that primarily contribute to the zero point energy remain approximately constant during adsorption from the gas phase. Interestingly, the strongest and weakest binding site is predominantly different for probe molecules in this study, i.e., there exists no universally ‘strong’ or ‘weak’ BA site. The choice of active site

model may also be adsorbate or reaction dependent as illustrated by the strong adsorption of NH_3 and CH_3OH on the thermodynamically least stable T9 site. Binding energies calculated in the absence of vdW contributions show significantly larger variations. For example, the binding energies of pyridine, the largest molecule among the five compounds studied, covers a range of 1.0 eV with a standard deviation of 0.36 eV. These data suggest that while the local interaction of adsorbates and/or intermediates with a BA is strongly dependent upon the BA site location, the influence of dispersion interactions with the surrounding pore walls renders acid sites more similar in nature. Likewise, this degeneracy contributes, in part, to the difficulty associated with the experimental detection of adsorption energy differences. In contrast, the stability of transition states is expected to be more sensitive to the specific acidity and local electronic structure of the active site, thereby leading to a more pronounced difference in the rate constants of elementary steps.

The acid strength and acid site concentration in zeolites is often characterized through ammonia (or pyridine) binding energy measurements and titration experiments, respectively. However, interpreting the binding energy of basic molecules to acidic sites as measure of acidity is complicated, largely because the adsorption process depends on adsorbate and catalyst proton affinities as well as the interaction of the protonated adsorbate with the acid site.[153] While the ammonia and pyridine binding energies in Table 4.5 indicate different levels of acidity at different T sites, these measures of acidity fail to follow any evident trends or heuristic guidelines. This observation can be rationalized by the unique local site geometry and confinement effects around each individual T site. Adsorption geometries of NH_3 are shown in Figure 4.2 with views along the sinusoidal

and straight channels, which are approximated by an isosurface of the calculated charge density 0.004 e/Å^3. Although NH_3 commonly abstracts the BA proton and the resulting NH_4^+ cation is generally oriented towards the channel center, a large variety of adsorbed configurations is observed.

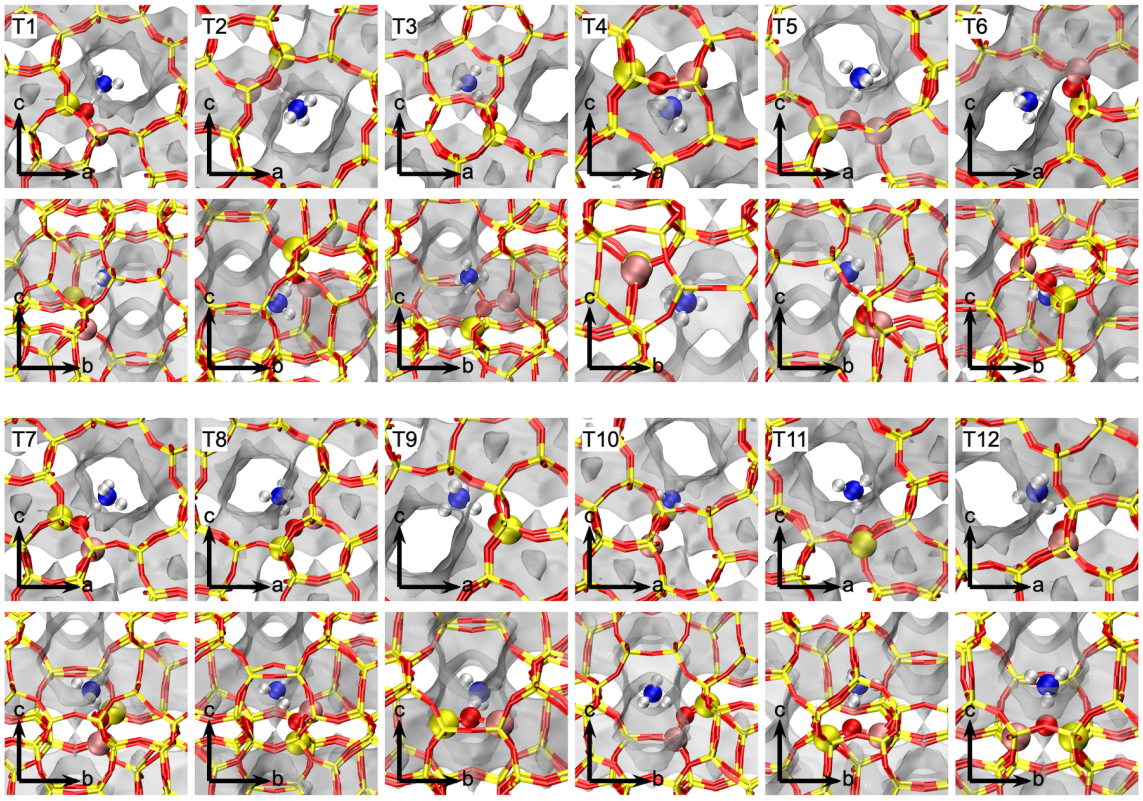

Figure 4.2 Ammonia adsorption geometries on various acid sites of H-ZSM-5 (Si – yellow, O – red, Al – maroon, N – blue, H – white). For each T site, two views are provided, i.e., along the a and b directions.

In agreement with an earlier study, no relationship between the binding energies of NH_3 or C_5H_5N and the O—H stretch frequency as an intrinsic property of acid sites can be identified.[151] The best intrinsic measure of acidity remains the deprotonation energy of a BA site, which unfortunately cannot be reliably obtained from our energetically accurate simulations due to the use of periodic boundary conditions. The same restriction

applies to available experimental methods and, hence, the deprotonation energy is omitted from the discussion of acidity scales.

4.4 Conclusions

Periodic density functional theory (DFT) calculations using the dispersion-corrected vdW-DF functional were used to determine the thermodynamic stability, O—H bond length and stretch frequency, Si—OH—Al bond angle, and binding energies of various probe molecules on Brønsted acid sites located at all 12 T sites of H-ZSM-5. Adsorption energies proved to be strongly dependent on the inclusion of dispersion forces, which are best described in a periodic unit cell and through the self-consistent treatment in the vdW-DF functional. No correlation between commonly used acidity scales (e.g., O—H stretch frequency, NH_3 and pyridine adsorption) could be identified. Notably, the binding strengths of CH_4, CO, CH_3OH, NH_3, and C_5H_5N do not follow a common trend; however, variations of the physical and chemical properties for different T sites in H-ZSM-5 suggest that conclusions from theoretical studies, particularly the predictions of activation barriers, may depend quantitatively and even qualitatively on the specific T site chosen as a computational model. Interestingly, the lowest Si/Al ratio for ZSM-5 synthesis is ca. 10, which is similar to the number of unique T sites (i.e., 12). To this end, it is evident that varying the Si/Al ratio of H-ZSM-5 catalysts is insufficient to experimentally assess the effects of Al site acidity without knowledge of occupied BA site locations within the framework.

The results of this study clearly demonstrate the challenges of modeling catalytic reactions in complex zeolites possessing a high level of heterogeneity, such as the MFI crystal structure. Theoretical modeling of these complex systems could be improved

through advanced experimental synthesis and characterization techniques that lead to a fundamental understanding of the distribution of aluminum atoms derived from differences in synthesis conditions.

Chapter 5 Computational assessment of the dominant factors governing the mechanism of methanol dehydration over H-ZSM-5 with heterogeneous Al distribution

The material discussed in this chapter has been submitted for publication. Figure and table numbers have been changed for dissertation consistency.

5.1 Introduction

Conversion of methanol to hydrocarbons (MTH) over acidic zeolites has attracted considerable attention as an effective route to produce commodity chemicals (olefins) and liquid fuels (gasoline). Although the overall process leading to the formation of aromatics and aliphatics is complicated, it has widely been accepted that the first step is the dehydration of methanol to dimethyl ether (DME).[154-157] It is believed that DME, as well as methanol, is added to a hydrocarbon scaffold within the zeolite structure to form olefins, paraffins, and aromatic products, a mechanism known as the "hydrocarbon pool".[18, 158-160] DME can also appear as an intermediate in C_1 chemistry or methane/syngas chemistry,[161] and it can be transformed catalytically to methyl acetate,[162] formaldehyde,[163] triptane,[164] and ethanol.[161, 165] Furthermore, DME may also be used in place of LPG (liquefied petroleum gas) or as diesel fuel due to its high cetane number, sootless combustion, lower NO_x and SO_x emission, and environmentally benign and non-toxic nature.[161, 166-168]

Prior studies have identified and discussed two possible pathways for the dehydration of methanol to DME over acidic catalysts.[169-173] Scheme 5.1 shows the various intermediates and transition states involved in the conversion of methanol to DME for both pathways.

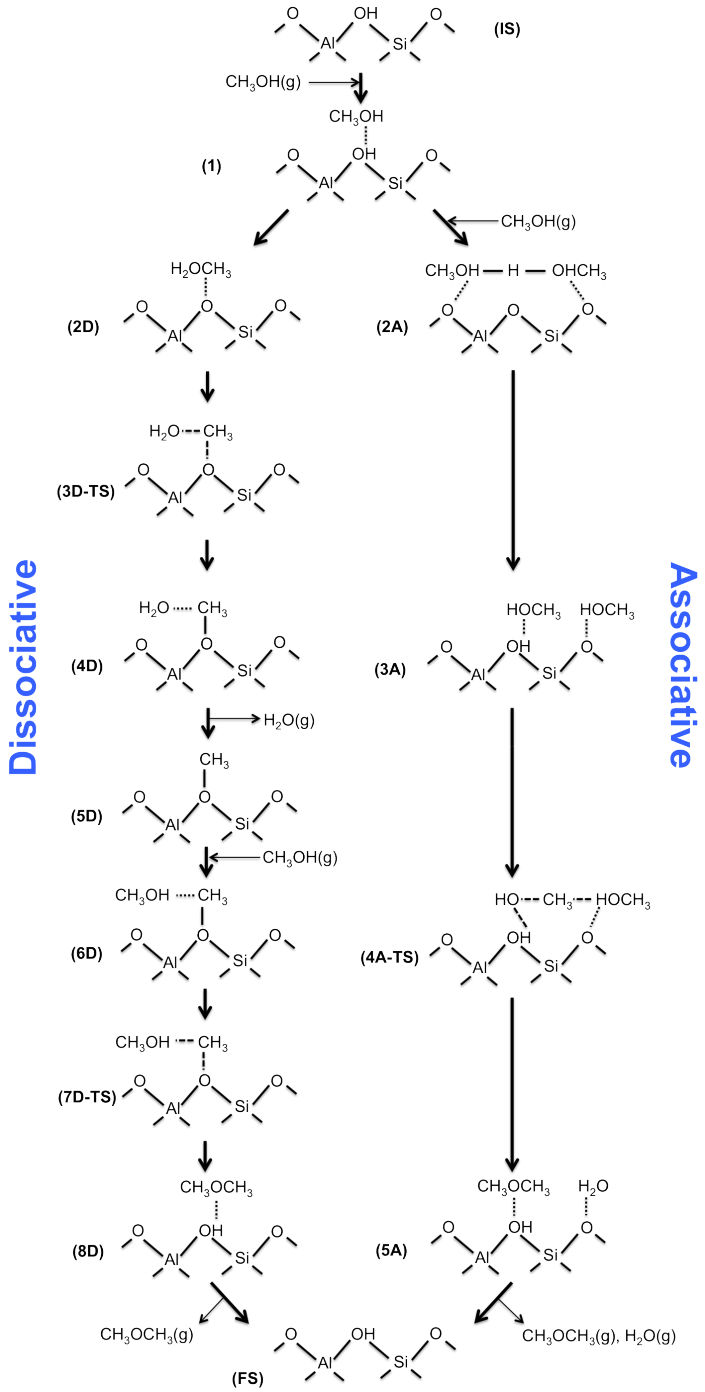

Scheme 5.1 The dissociative (left) and associative (right) reaction pathways for the conversion of methanol to DME catalyzed by an H-form zeolite. States labeled 'D' and 'A' belong to the dissociative and the associative routes, respectively. Labels that contain 'TS' represent the transition states. Electrostatic interactions between adsorbates and active sites are shown by "…", while transition state complex interactions are denoted by "---".

Provided the reaction is conducted on an H-form zeolite, both pathways are catalyzed by Brønsted acid sites, each located at the oxygen atom bridging an aluminum atom and a silicon atom of the zeolite framework.[171, 174-175]

The dissociative pathway (or the step-wise pathway) begins with the adsorption of a methanol molecule at the Brønsted acid site (**1**). The subsequent formation of a surface methoxy group is accompanied by the elimination of a water molecule (**3D-TS**, **4D**, **5D**). The reaction then proceeds with the nucleophilic attack of a second methanol molecule on the methoxy group (**6D**), which leads to formation of DME (**7D-TS**, **8D**). In the associative pathway (or the concerted pathway), the formation of DME and water (**4A-TS**, **5A**) occurs after the co-adsorption of two methanol molecules at the Brønsted acid site (**2A**, **3A**). There are several experimental and computational studies in the literature that have attempted to reveal the preferred mechanism of methanol dehydration to DME on acidic zeolites. These investigations report contradictory results. Blaszkowski and van Santen[169-170] propose the concerted route is the dominant mechanism on the basis of the lower activation barrier estimated for this pathway using density functional theory (DFT) calculations on zeolite clusters. This conclusion has been confirmed by another more recent DFT investigation using a small cluster model.[156] Jones and Iglesia[176] provided additional evidence for this pathway derived from a combination of kinetic analysis of reaction rate vs. methanol pressure and also from their DFT calculations of Gibbs free energies for a single active site location in the periodic H-ZSM-5 structure. On the contrary, Kubelková et al.[177] through infrared (IR) spectroscopy of surface species over zeolites HY and H-ZSM-5 at conditions relevant to the methanol-to-DME reaction suggested that the reaction occurs through the step-wise mechanism. A similar result was

obtained by Moses and Nørskov[174] via DFT modeling of the reaction for a periodic representation of H-ZSM-22 (TON). Generally, one should treat the results obtained from DFT simulation on small cluster models composed of 3[170] and 5[156] tetrahedral sites (T sites) with caution, because this simplistic approach is not capable of capturing the complex active site environment solvating the reaction species and the long-range guest-host interactions inside the zeolite pores. A few DFT studies have been conducted with periodic boundary conditions for CHA[175, 178] and TON zeolites.[174] To the best of our knowledge, there has been only one periodic DFT study of the methanol-to-DME reaction mechanism for H-ZSM-5,[176] which along with SAPO-34 is the most commonly used catalyst for the methanol-to-hydrocarbon (MTH) process.[167, 179]

In the present study, we perform a thorough mechanistic investigation of the methanol-to-DME reaction over H-ZSM-5 via DFT calculations with periodic boundary conditions and a van der Waals exchange correlation functional (vdW-DF).[37-38] We compare the energetics of the two reaction routes not only by the calculation of ground state electronic energies, but also by the computation of the reaction components' Gibbs free energies at typical conditions. The complexity of H-ZSM-5 with its two types of channels, its large unit cell, and the presence of 12 crystallographically distinguishable T sites in its orthorhombic structure render this study more challenging compared to similar studies previously performed on simpler zeolite structures, such as CHA (with only one unique T site)[175, 178] and TON (with 1D straight channels).[174] In order to get a better understanding of the possible heterogeneity of active sites in H-ZSM-5 (MFI-type zeolite) and their effect on the catalysis of methanol dehydration, we conduct our calculations for various Brønsted acid site locations representative of MFI's straight and sinusoidal channels, and

channel intersections. The consequences of varying active site properties, such as specific acidity and confinement that may influence its kinetic performance are also investigated.[50, 98, 137, 180-181] Here, acidity is tuned by various heteroatom substitutions (i.e., aluminum, gallium, and indium), and is estimated through the strength of acid site interaction with a probe base, pyridine.

Jones et al.[182] showed that the first order rate constant of the methanol-to-DME reaction increases with enhanced confinement of the transition state by comparison of several zeolite framework types with similar acid strength of active sites. This observation was attributed to the stronger vdW interactions in more confined environments. The significance of vdW effects on the stabilization of transition states has also been indicated by Artioli et al., who observed much higher (by factors of 10^4) NO oxidation rates on several purely siliceous microporous zeolites than in the homogeneous reaction.[183] The use of a dispersion-corrected exchange correlation functional in our DFT modeling enables us to assess the consequence of H-ZSM-5 active site local environment and its imposed vdW contribution to the stabilization of various transition states that form during the dehydration of methanol to DME. We show that the heterogeneous distribution of active sites causes varying interactions between reaction intermediates and the framework of zeolite pores, which influences the catalytic behavior of H-ZSM-5 in the methanol dehydration reaction at different reaction conditions (e.g., temperature and pressure). Conversely, other factors such as active site acid strength seemingly play a less important role in the reaction mechanism. This theoretical study of the methanol-to-DME reaction on H-ZSM-5 provides a better understanding of the reaction mechanism on one

of the most frequently used catalysts in the methanol conversion process, and may prove to be influential in the enhanced design of optimal catalysts and process conditions.

5.2 Computational methods

DFT calculations were performed using the Atomic Simulation Environment (ASE),[140] the Vienna ab initio simulation package (VASP),[41-42] and the projector-augmented wave (PAW) method.[43] The vdW-DF exchange-correlation functional,[37-38] which self-consistently accounts for dispersion interactions within a porous-structured material, was employed. Periodic boundary conditions in all three directions of the MFI unit cell were used with the plane-wave energy cutoff set at 540 eV. Brillouin-zone sampling was restricted to the Γ-point and Gaussian-smearing with k_bT = 0.1 eV was used. The optimized lattice constants of the siliceous MFI unit cell are a = 20.29 Å, b = 19.94 Å, c = 13.27 Å, which are slightly larger (~1%) than experimental values.[20] These lattice constants were used in all subsequent calculations of the acidic zeolite. Connected to each Brønsted acid site heteroatom are four oxygen atoms to accommodate the proton in the H-form zeolite. As described previously,[184] we chose the most energetically stable arrangement for each T site substitution as long as the resulting Brønsted acid proton was accessible to reactant molecules. In cases where steric hindrance restricted access to the acid site, the next most stable (and accessible) proton location was selected. vdW contributions were directly extracted from the VASP vdW-DF output. Gibbs free energies were estimated in the ideal gas condition for gas phase compounds and in the harmonic oscillator approximation for the O—H group of the Brønsted acid site and adsorbed species using vibrational frequencies obtained with a displacement of 0.01 Å. Spurious imaginary frequencies appear due to computational inaccuracies in the

vibrational analysis of floppy modes, which is common in such calculations.[185-186] These imaginary modes were replaced with 12 cm^{-1}, i.e., approximately the translational frequency of a particle in a box.[185] Reaction transition states were optimized through the climbing image nudged elastic band (NEB) approach.[187] The convergence criterion was set to 0.02 eV/Å per atom for reactants, products, and intermediates, and 0.05 eV/Å per atom for transition states.

5.3 Results and discussion

Both the associative and dissociative pathways of the methanol-to-DME reaction were modeled over different Brønsted acid sites of H-form zeolite MFI (H-ZSM-5). Initial, final, and intermediate states as well as the transition states were optimized for several T sites, i.e., T12 (Al12—OH—Si12, at channel intersection), T11 (Al11—OH—Si5, in the straight channel), T10 (Al10—OH—Si1, in the sinusoidal channel), and T3 (Al3—OH—Si4, at channel intersection). Details of the T site locations are provided elsewhere and we use the notation Al12, for example, to refer to an aluminum substitution at the T12 site.[184] While there are 12 crystallographically distinguishable locations for heteroatom substitution in the MFI structure, these positions were selected to represent a spectrum of active sites and allow for a comparison of their respective kinetic behavior. The evaluation of both T3 and T12 sites at channel intersections also makes it possible to compare the performance of two different active site locations with a similar geometry. These considerations are important, in particular because prior studies have shown that aluminum siting in ZSM-5 is highly influenced by synthesis conditions such that it is neither restricted to one specific T site nor occurs in a random manner.[22-23, 188] In Figure

5.1 the commonly studied T12 site is shown as it catalyzes three key elementary reaction steps.

Kinetic analyses of the reaction presented by Moses and Nørskov[174] and Jones and Iglesia[176] show that at moderate pressures the relative rates of the two reaction pathways strongly depend on the difference of their transition state Gibbs free energies referenced to the initial state, i.e., the clean zeolite and gas phase methanol. Thus, we base our discussion on Gibbs free energy calculations at typical conditions instead of ground state electronic energies at 0 K. The Gibbs free energy is calculated as

$$G(T) = E_{\text{elec.}} + E_{\text{ZPE}} + \int_0^T C_P \, \mathrm{d}T - TS\,(T), \tag{5.1}$$

where G is the Gibbs free energy, $E_{\text{elec.}}$ is the DFT-computed electronic energy, E_{ZPE} is the zero point energy, C_P is heat capacity at constant pressure, T is temperature, and S is entropy. A rigorous assessment of the dominant reaction mechanism requires that all terms appearing in equation (5.1) be taken into account, including the calculation of heat capacity and entropic terms as functions of temperature. The entropic effects, in particular, have a significant impact as discussed in more detail in section 5.3.4.

5.3.1. The dissociative pathway

The next step in this mechanism is the reaction of a second methanol molecule with the surface methoxy to form a dimethyloxonium group (**6D**, **7D-TS**). DME may then desorb into the gas phase after the rearrangement of the cationic species and proton transfer to the zeolite framework (**8D**, **FS**) to regenerate the Brønsted acid site. The transition state structures in both steps of this pathway are identified by an umbrella flip of a CH_3 group where all four atoms lie on the same plane (Figure 5.1A–D).

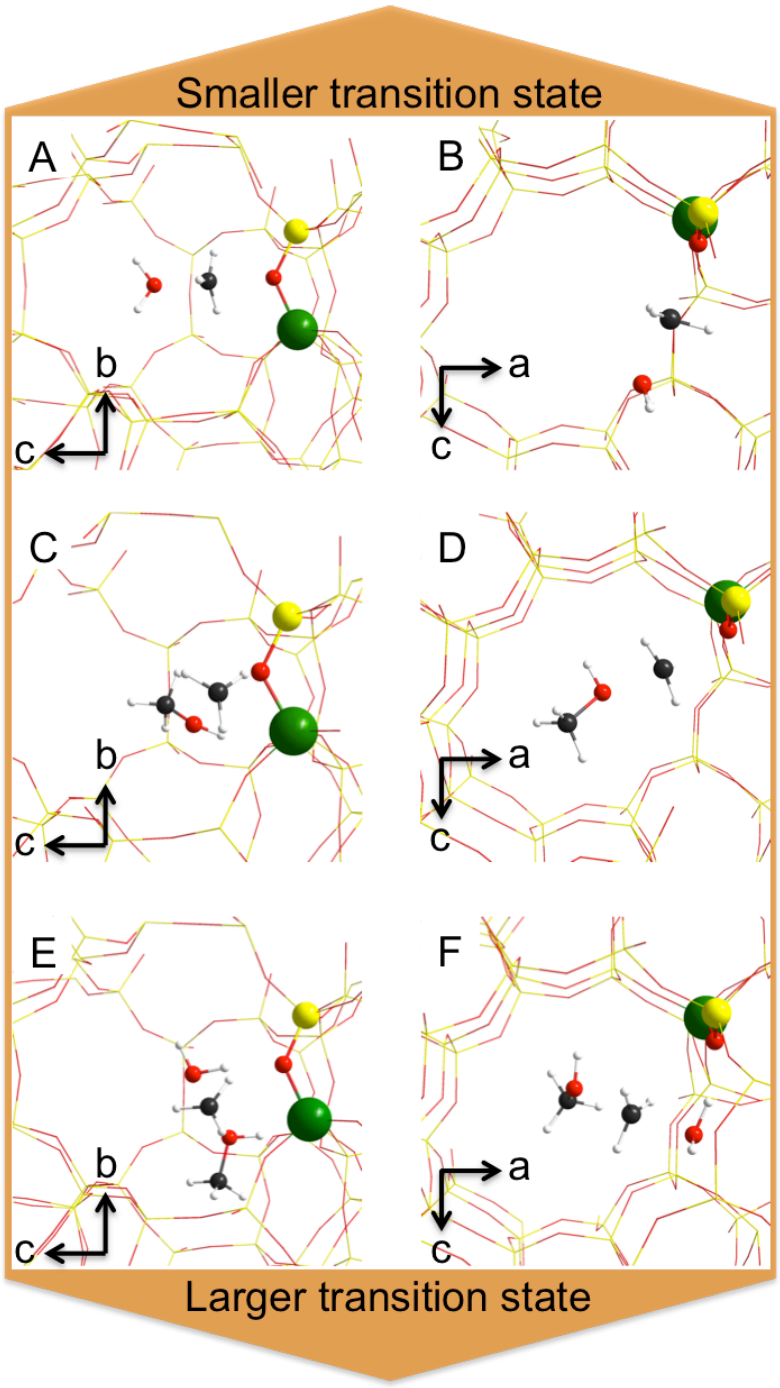

Figure 5.1 Transition state structures for the dissociative pathway. H_2O elimination (**3D-TS**, A and B), DME formation (**7D-TS**, C and D), and the associative pathway (**4A-TS**, E and F) of the methanol-to-DME reaction on H-ZSM-5 with aluminum located at the T12 position of the MFI framework (Si – yellow, O – red, Al – green, C – black, H – white).

Figure 5.2 shows the Gibbs free energy diagram for the dissociative pathway at T = 450 K and P = 0.1 bar of each gas compound partial pressure, which is within a typical range of experimental conditions applied for methanol dehydration to DME over H-ZSM-5.[176, 189-191] Energy values corresponding to each step of the pathway are presented in Tables 5.1 – 5.4 for Al sitings Al12, Al11, Al10, and Al3, respectively.

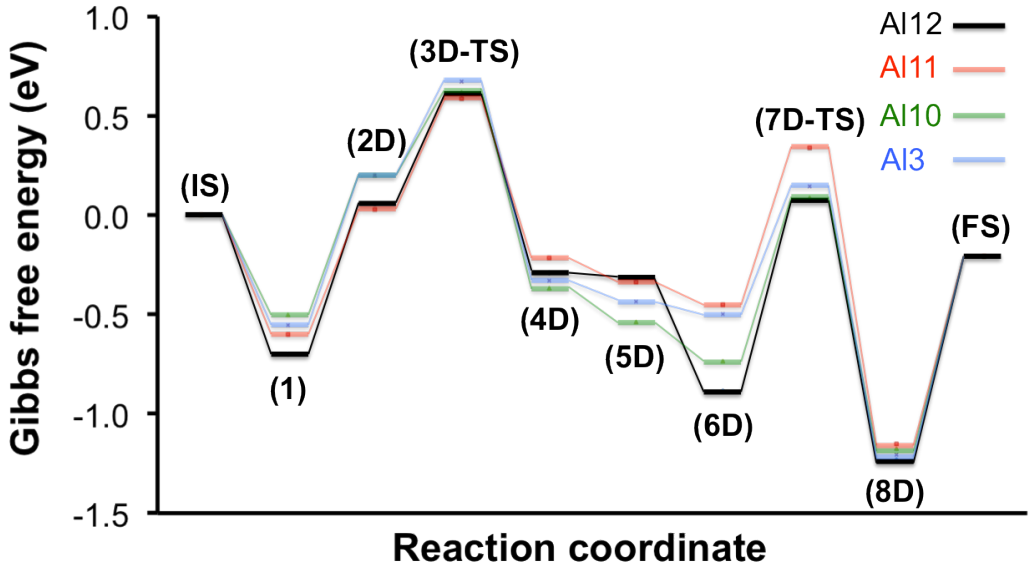

Figure 5.2 Gibbs free energy diagram of the dissociative pathway of the methanol-to-DME reaction over H-ZSM-5 with the active site located at the T12, T11, T10, and T3 positions. The energy of each state along the reaction coordinate is expressed relative to the energy of the clean zeolite structure and two gas phase methanol molecules as the reference (**IS**).

The dissimilar reaction behavior of H-ZSM-5 active sites in catalyzing the methanol dehydration reaction is evident by the variations in the Gibbs free energy profiles (Figure 5.2) of the step-wise mechanism at various active site locations. Considering for example the relatively large adsorption complex of methoxy and methanol in state **6D**, we can clearly discern that the heterogeneous site distribution in H-ZSM-5 can have a great impact on the adsorbate-host interaction and lead to Gibbs free energy variations as large

as 0.43 eV. More importantly, the Gibbs free energy profiles cross each other along the reaction coordinate and do not follow a common trend. For instance, the T12 site, the most frequently used site for computational investigations, is a clear outlier because it binds methoxy (**5D**) most weakly, but provides the strongest adsorption site for the co-adsorption of methoxy and methanol (**6D**). We will compare this observation with the performance of the active sites in the associative mechanism and discuss the implications of heterogeneous site distributions in further detail in section 5.3.3.

5.3.2 The associative pathway

The associative pathway also begins with methanol adsorption at a Brønsted acid site. The adsorption of a second methanol molecule results in a protonated methanol dimer configuration bound to the zeolite active site (**2A**). This configuration involves proton abstraction from the Brønsted acid site such that the proton links the two methanol molecules through hydrogen bonds and the positively charged dimer interacts with the Lewis base site of the zeolite framework. However, prior to the reaction the methanol dimer undergoes a necessary rearrangement to a less stable configuration, by 0.45 eV, 0.33 eV, 0.16 eV, and 0.51 eV for Al12, Al11, Al10, and Al3, respectively (Tables 5.1 – 5.4). During this rearrangement a proton is transferred back to the zeolite structure regenerating the Brønsted acid site and one of the methanol molecules rotates, as a result of which the hydroxyl group of the second methanol molecule approaches the methyl group of the first molecule (**3A**). This precursor state, immediately prior to the transition state, is in agreement with the one identified by Moses and Nørskov,[174] and Jones and Iglesia[176] in their study of methanol dehydration on H-ZSM-22 and H-ZSM-5, respectively.

Table 5.1 Gibbs free energies and the constituent contributions along the reaction coordinate for Al located at the T12 position of H-ZSM-5.[a]

	State[b]	G	$E_{elec.}$	E_{ZPE}	$\int_0^T C_P \, dT$	TS
	IS	0.00 (-2218.94)	0.00 (-2219.80)	0.00 (3.12)	0.00 (0.47)	0.00 (2.73)
	1	-0.70	-1.36	0.02	0.01	-0.62
Dissociative	**2D**	0.06	-0.66	0.07	0.00	-0.64
	3D-TS	0.61	0.05	-0.01	0.04	-0.52
	4D	-0.29	-0.79	0.01	0.07	-0.42
	5D	-0.33	-0.18	-0.07	0.06	0.14
	6D	-0.88	-1.25	-0.05	0.12	-0.30
	7D-TS	0.08	-0.45	-0.07	0.08	-0.51
	8D	-1.23	-1.74	-0.06	0.07	-0.49
Associative	**2A**	-1.26	-2.58	0.07	0.03	-1.23
	3A	-0.81	-2.02	0.04	0.07	-1.09
	4A-TS	0.07	-1.28	0.08	0.04	-1.23
	5A	-0.74	-1.86	0.03	0.09	-1.00
	FS	-0.21	-0.22	-0.05	0.03	-0.04

[a] All energy values are in eV. Energies at each state are reported relative to the initial state (**IS**); the absolute values at **IS** are indicated within parentheses.

[b] Readers are referred to Scheme 5.1 to locate each state.

Table 5.2 Gibbs free energies and the constituent contributions along the reaction coordinate for Al located at the T11 position of H-ZSM-5.[a]

	State[b]	G	$E_{elec.}$	E_{ZPE}	$\int_0^T C_P \, dT$	TS
	IS	0.00 (-2218.86)	0.00 (-2219.74)	0.00 (3.13)	0.00 (0.46)	0.00 (2.71)
	1	-0.60	-1.18	0.02	0.04	-0.53
Dissociative	**2D**	0.03	-0.63	0.04	0.03	-0.59
	3D-TS	0.59	-0.09	-0.01	0.04	-0.65
	4D	-0.22	-0.68	0.00	0.09	-0.37
	5D	-0.34	-0.24	-0.07	0.07	0.10
	6D	-0.45	-0.88	-0.06	0.13	-0.36
	7D-TS	0.34	-0.21	-0.07	0.09	-0.54
	8D	-1.15	-1.64	-0.06	0.08	-0.47
Associative	**2A**	-1.14	-2.36	0.05	0.05	-1.11
	3A	-0.81	-2.01	0.04	0.08	-1.09
	4A-TS	0.13	-1.20	0.07	0.05	-1.21
	5A	-1.06	-2.09	0.00	0.10	-0.93
	FS	-0.21	-0.22	-0.05	0.03	-0.04

[a] All energy values are in eV. Energies at each state are reported relative to the initial state (**IS**); the absolute values at **IS** are indicated within parentheses.

[b] Readers are referred to Scheme 5.1 to locate each state.

Table 5.3 Gibbs free energies and the constituent contributions along the reaction coordinate for Al located at the T10 position of H-ZSM-5.[a]

	State[b]	G	$E_{elec.}$	E_{ZPE}	$\int_0^T C_P \, dT$	TS
	IS	0.00 (-2218.98)	0.00 (-2219.84)	0.00 (3.12)	0.00 (0.47)	0.00 (2.73)
	1	-0.50	-1.15	0.04	0.02	-0.59
Dissociative	**2D**	0.20	-0.49	0.06	0.02	-0.62
	3D-TS	0.62	0.00	-0.02	0.04	-0.60
	4D	-0.37	-0.88	0.02	0.07	-0.42
	5D	-0.54	-0.39	-0.07	0.06	0.14
	6D	-0.73	-1.17	-0.05	0.11	-0.38
	7D-TS	0.09	-0.47	-0.07	0.08	-0.54
	8D	-1.17	-1.66	-0.06	0.07	-0.47
Associative	**2A**	-1.28	-2.56	0.06	0.04	-1.18
	3A	-1.12	-2.34	0.03	0.06	-1.12
	4A-TS	-0.12	-1.48	0.08	0.04	-1.23
	5A	-1.09	-2.24	0.02	0.08	-1.05
	FS	-0.21	-0.22	-0.05	0.03	-0.04

[a] All energy values are in eV. Energies at each state are reported relative to the initial state (**IS**); the absolute values at **IS** are indicated within parentheses.

[b] Readers are referred to Scheme 5.1 to locate each state.

Table 5.4 Gibbs free energies and the constituent contributions along the reaction coordinate for Al located at the T3 position of H-ZSM-5.[a]

	State[b]	G	$E_{elec.}$	E_{ZPE}	$\int_0^T C_P \, dT$	TS
	IS	0.00 (-2218.86)	0.00 (-2219.74)	0.00 (3.12)	0.00 (0.46)	0.00 (2.70)
	1	-0.55	-1.16	0.02	0.04	-0.54
Dissociative	**2D**	0.20	-0.47	0.06	0.04	-0.57
	3D-TS	0.67	0.01	-0.01	0.05	-0.62
	4D	-0.33	-0.80	0.02	0.08	-0.49
	5D	-0.44	-0.27	-0.06	0.07	0.10
	6D	-0.50	-1.04	-0.03	0.12	-0.32
	7D-TS	0.14	-0.25	-0.06	0.09	-0.53
	8D	-1.21	-1.68	-0.05	0.09	-0.46
Associative	**2A**	-1.13	-2.43	0.07	0.05	-1.18
	3A	-0.62	-1.73	0.03	0.10	-0.98
	4A-TS	0.29	-1.10	0.06	0.06	-1.27
	5A	-1.06	-2.28	-0.01	0.12	-0.87
	FS	-0.21	-0.22	-0.05	0.03	-0.04

[a] All energy values are in eV. Energies at each state are reported relative to the initial state (**IS**); the absolute values at **IS** are indicated within parentheses.

[b] Readers are referred to Scheme 5.1 to locate each state.

The transition state is formed after proton transfer from the zeolite acid site to the first methanol hydroxyl group while methyl moves toward the second methanol hydroxyl (**4A-TS**). As in the dissociative route, this complex reaches its maximum energy when the methyl group undergoes an umbrella flip and its three hydrogen atoms and the carbon atom form a planar structure (Figure 5.1, E and F). The CH_3 species then keeps moving toward the other methanol hydroxyl to form dimethyloxonium. The latter then rearranges and the proton is transferred back to the zeolite structure, regenerating the Brønsted acid site. The Gibbs free energy diagram of the associative pathway is presented in Figure 5.3 for T = 450 K and P = 0.1 bar of each gas compound partial pressure. Energy values corresponding to each step of the pathway are presented in Tables 5.1 – 5.4 for Al sitings Al12, Al11, Al10, and Al3, respectively.

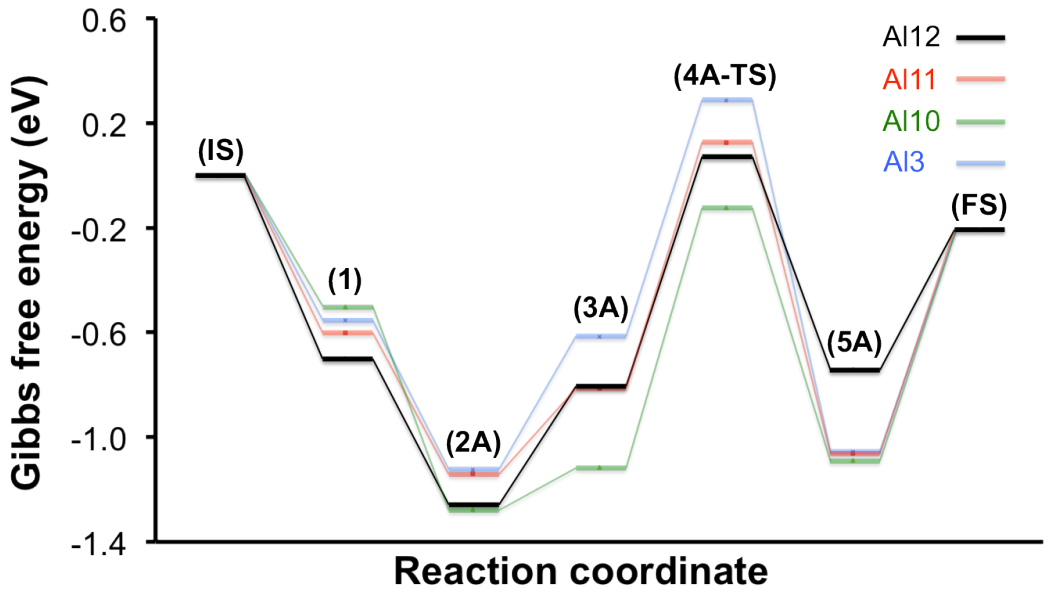

Figure 5.3 Gibbs free energy diagram of the associative pathway of the methanol-to-DME reaction over H-ZSM-5 with the active site located at the T12, T11, T10, and T3 positions. The energy of each state along the reaction coordinate is expressed relative to the energy of the clean zeolite structure and two gas phase methanol molecules (**IS**).

Gibbs free energy diagrams for the concerted mechanism over the various active site locations indicate their unlike kinetic behavior (Figure 5.3). The transition state energy for **4A-TS** varies from -0.12 eV for the most stable location (T10) to 0.29 eV for the least stable one (T3), thus spanning a range of 0.41 eV. The 0.22 eV difference in transition state free energies at T3 and T12 sites, both located at channel intersections, shows that two active sites within the ZSM-5 structure with a similar geometry will not necessarily render equally stabilized transition states.

5.3.3 Heterogeneity of active sites

Our finding that active site locations can alter the Gibbs free energy profiles in a non-systematic way are in agreement with our earlier investigation of the structural and chemisorption properties of potential active sites in H-ZSM-5, where large variations in active site properties were observed.[184] Gounder and Iglesia have also shown a strong dependence of cationic transition state free energy on local channel environment in their study of monomolecular cracking and dehydrogenation of propane and n-butane over H-MOR.[98]

Before we discuss the impact of active site heterogeneity on the dominant reaction mechanism, we first argue that the observed scatter among intermediates and transition state free energies for the various Al sitings is not an entropic effect. In Figures 5.4 and 5.5 we show that similar scatter exists for the respective electronic energies in the absence of entropy corrections. Entropic effects generally destabilize reaction intermediates and transition states with increasing temperature. The entropy loss is mainly due to the frustration of the translational/rotational degrees of freedom when transferred to the adsorbed phase. Table 5.5 summarizes the Gibbs free energies and

electronic energies of all three transition states on the four studied active site locations. The transition state Gibbs free energies vary by 0.41, 0.26, and 0.08 eV for the associative route, DME formation, and H_2O elimination, respectively. Similarly, the variations of the corresponding electronic energies are 0.38, 0.26, and 0.14 eV, respectively. Because Gibbs free and electronic energies exhibit nearly identical trends, we may conclude that the temperature dependent entropy correction does not vary significantly with the zeolite active site location, and thus, the origin of the disparate reaction energy diagrams is not of entropic nature.

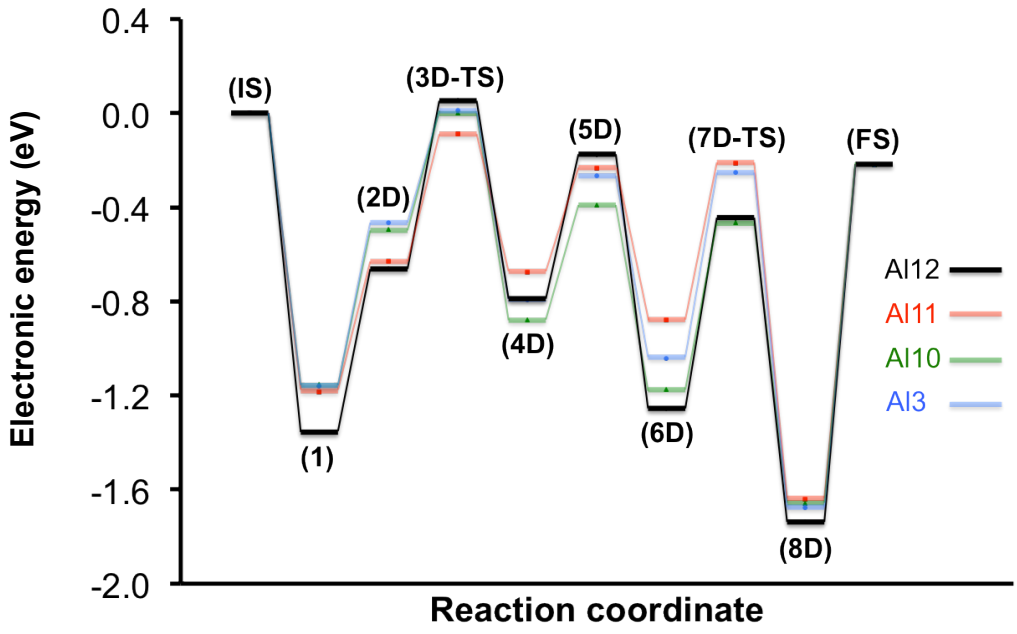

Figure 5.4 Electronic energy diagram of the dissociative pathway of the methanol-to-DME reaction over H-ZSM-5 with the active site located at the T12, T11, T10, and T3 positions. The energy of each state along the reaction coordinate is expressed relative to the energy of the clean zeolite structure and two gas phase methanol molecules as the reference (**IS**).

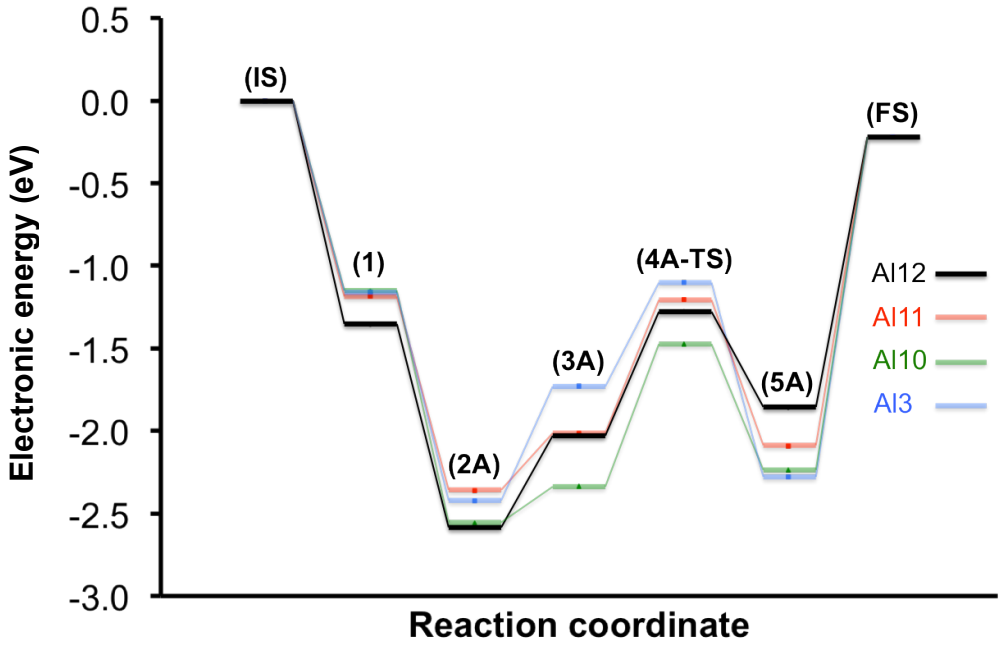

Figure 5.5 Electronic energy diagram of the associative pathway of the methanol-to-DME reaction over H-ZSM-5 with the active site located at the T12, T11, T10, and T3 positions. The energy of each state along the reaction coordinate is expressed relative to the energy of the clean zeolite structure and two gas phase methanol molecules as the reference (**IS**).

A comparison of the transition state Gibbs free energies given in Table 5.5 reveals that the transition state for H_2O elimination (**3D-TS**) is always of higher energy than the transition state for DME formation (**7D-TS**) regardless of active site location. We will show later that this holds true for a broad range of pressure and temperature as well. This allows us to simplify the preferred pathway determination to a comparison of the transition states **3D-TS** (dissociative) and **4A-TS** (associative).[174] The direct comparison of these two transition states at the considered temperature and pressure conditions using the data in Table 5.5 indicates that the associative path is always more favorable than the

dissociative path, irrespective of the active site location. The influence of temperature and pressure on reaction pathways will be investigated in sections 5.3.4 and 5.3.5.

Table 5.5 Gibbs free energies (ΔG_{TS})[a] and electronic energies (ΔE_{TS}) of the three transition states forming in the methanol-to-DME reaction associative and dissociative pathways relative to gaseous methanol and clean H-ZSM-5.[b]

Al siting	**H_2O elimination (3D-TS)**		**DME formation (7D-TS)**		**Associative (4A-TS)**	
	ΔG_{TS}	**ΔE_{TS}**	**ΔG_{TS}**	**ΔE_{TS}**	**ΔG_{TS}**	**ΔE_{TS}**
12	0.61	0.05	0.08	-0.45	0.07	-1.28
11	0.59	-0.09	0.34	-0.21	0.13	-1.20
10	0.62	0.00	0.09	-0.47	-0.12	-1.48
3	0.67	0.01	0.14	-0.25	0.29	-1.10

[a] Gibbs free energies were calculated at T = 450 K and P = 0.1 bar of each gas compound partial pressure.
[b] All energy values are in eV.

To pinpoint the root cause for the energy variations between different active site locations we turn our attention to the three transition states shown in Figure 5.1. The range in Gibbs free energy of 0.41 eV (spanning highest to lowest values) was calculated for the associative transition state (**4A-TS** in Figure 5.1 E and F, Table 5.5), while the variation for the transition states is much smaller for DME formation (0.26 eV, **7D-TS** in Figure 5.1 C and D, Table 5.5), and H_2O elimination (0.08 eV, **3D-TS** in Figure 5.1 A and B, Table 5.5). The level of variation shows a correlation with the transition state complex size. The associative pathway possesses the largest transition state and largest

energy variation, whereas the H_2O elimination step has the smallest transition state and the smallest site-dependent energy differences.

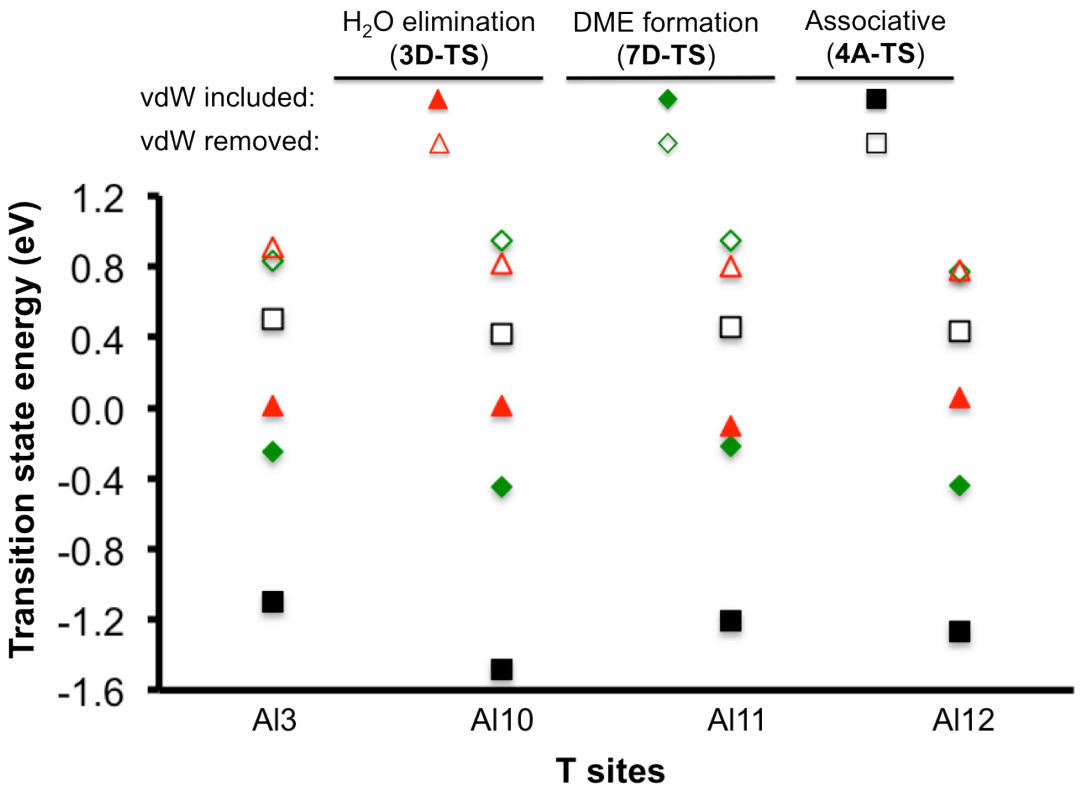

Figure 5.6 Transition state electronic energies for various active site locations obtained from calculations with vdW included (filled symbols) as well as vdW removed (open symbols). The average vdW stabilization decreases with transition state size in the order **4A-TS** (1.72 ± 0.11 eV) > **7D-TS** (1.22 ± 0.12 eV) > **3D-TS** (0.83 ± 0.07 eV) for all four active site locations.

A correlation with the transition state size is also evident for the extent of attractive vdW stabilization for different Al sitings in MFI. Figure 5.6 systematically contrasts the transition state electronic energies between the vdW included (filled symbols) and vdW removed (open symbols) calculations. Here, we use electronic energies rather than Gibbs free energies to focus on the immediate impact of dispersion forces and not on secondary contributions originating from zero point energy, heat capacity, or entropy changes. The

average vdW stabilization for the four active site locations, i.e., the difference between open and filled symbols in Figure 5.6, decreases with decreasing transition state size for the associative pathway (**4A-TS**), DME formation (**7D-TS**), and H_2O elimination (**3D-TS**) steps, respectively. Notably, none of the transition states, even in the concerted route, is large enough to establish repulsive interactions with the zeolite framework.

The magnitude of the vdW stabilization of all three transition states varies between 0.83 and 1.72 eV, and is about as large as the difference between the highest and lowest lying states in the calculated potential energy diagrams shown in Figures 5.2 and 5.3. The large magnitude of vdW contributions suggests that the use of a computational method or active site model incapable of taking these contributions into account can result in binding and activation barriers far from realistic values.[40, 97]

More importantly, attractive vdW interactions can change the relative stability of the transition states, which is important to determine dominant pathways and selectivities if applicable. For example, we stated above that the transition state for H_2O elimination (**3D-TS**) is always more energetic than the transition state for DME formation (**7D-TS**). This statement is confirmed when comparing the filled triangle (**3D-TS**) and diamond (**7D-TS**) symbols representing vdW corrected energies, but it would be incorrect if the open symbols in absence of vdW interactions were compared. In other words, vdW interactions are of such critical importance that they can change not only quantitative results, but also qualitative comparisons.

The magnitude of vdW interactions is not widely distributed over the four sites; yet, they cause a slightly more heterogeneous behavior of the active sites. In particular, a greater stabilization effect of the T10 site environment on the bulkier transition states of

the associative path (**4A-TS**) and DME formation (**7D-TS**) can be distinguished. This may be a result of the more tortuous shape of the sinusoidal channel where T10 is located and the better fit it can provide for the transition states via dispersion forces imposed by the surrounding zeolite pore walls. Similarly, state **3A** in Figure 5.3, which occurs just before **4A-TS**, is strongly stabilized at the T10 position, which turns the T10 motif from the initially least stable structure (**1**) into the most stable one. An exception to our preceding discussion is the adsorption complex **2A**, which is of equal size as **3A**, or **4A-TS**; yet, it is about equally stable at all active site locations. We attribute this difference primarily to the ionic interactions of **2A** with the active site, which masks the effects of size and location-dependent vdW interactions.

The general correlation between vdW stabilization and transition state size is not unexpected since larger size species will be more confined in the zeolite porous environment and their stabilization will therefore be more location/geometry dependent. This finding is in line with the theoretical study of the physisorption energies of C_1-C_4 primary alcohols on H-ZSM-5 and silicalite-1 by Nguyen et al., where a larger difference between the binding strengths of straight and sinusoidal channels was observed for heavier alcohols.[192] Brogaard et al.[193] have also obtained a linear increase of alkane adsorption enthalpies with the number of carbon atoms in their DFT study for H-ZSM-22 using the BEEF-vdW functional.[194]

5.3.4 Reaction mechanism variation with temperature

The methanol-to-DME reaction can be conducted on H-ZSM-5 over a range of temperatures, which may contribute to the conflicting literature reports regarding the dominant reaction mechanism.[176-177] To quantify the impact of temperature variations on

the reaction mechanism, we consider the temperature dependent Gibbs free energy change, equation (5.1), of the transition states (ΔG_{TS}) for the associative route (**4A-TS**), H_2O elimination (**3D-TS**), and DME formation (**7D-TS**) relative to the Gibbs free energy of the clean zeolite structure (G_{clean}) and gaseous compounds as follows:

$$\Delta G_{TS(associative)} = G_{TS(associative)} - G_{clean} - 2G_{CH_3OH(g)}, \quad (5.2)$$

$$\Delta G_{TS(H_2O\ elimination)} = G_{TS(H_2O\ elimination)} - G_{clean} - G_{CH_3OH(g)}, \text{ and} \quad (5.3)$$

$$\Delta G_{TS(DME\ formation)} = G_{TS(DME\ formationn)} + G_{H_2O(g)} - G_{clean} - 2G_{CH_3OH(g)}. \quad (5.4)$$

This approach is analogous to the one taken by Moses and Nørskov.[174] As indicated in equation (5.2), two gas phase molecules are lost in the transition state of the associative pathway, while only one gaseous molecule is lost during the formation of each transition state of the dissociative pathway, equations (5.3) and (5.4). Consequently, ΔG_{TS} of the associative path exhibits a stronger temperature dependence, which is reflected by a greater slope of the ΔG_{TS}-temperature curve (black lines for **4A-TS**) in Figure 5.7 than for the dissociative path (red lines for **3D-TS** and green lines for **7D-TS**). As previously discussed in section 5.3.3, the trend is consistent for all active site locations and H_2O elimination (**3D-TS**) is always less energetically favorable than DME formation (**7D-TS**).

The greater slope of the associative pathway curves results in a crossover temperature at which the associative free energy change (**4A-TS**) becomes larger than the free energy changes of both steps in the dissociative pathway, in particular the more activated H_2O elimination (**3D-TS**). Above this crossover temperature we expect the dominant mechanism to shift from the associative to the dissociative route. If aluminum atoms occupied only one T site in the MFI framework, we could identify a specific crossover temperature for a given pressure condition. In practice, however, this is unlikely and a

distribution of site occupations must be considered. Our study considers a realistic scenario where Al occupies different T sites, thus generating heterogeneous aluminum occupation in the zeolite that in turn leads to a temperature window for the transition from the associative mechanism to the dissociative mechanism. The lower limit of this temperature window at ca. 700 K suggests that for typical reaction temperatures, methanol conversion to DME proceeds primarily along the concerted mechanism. It is only above 700 K that DME formation via the stepwise pathway becomes competitive and ultimately dominant above ca. 1000 K. For a temperature range as large as 300 K or more (gray zone in Figure 5.7), both mechanisms are feasible due to the possible heterogeneity of active site locations in H-ZSM-5.

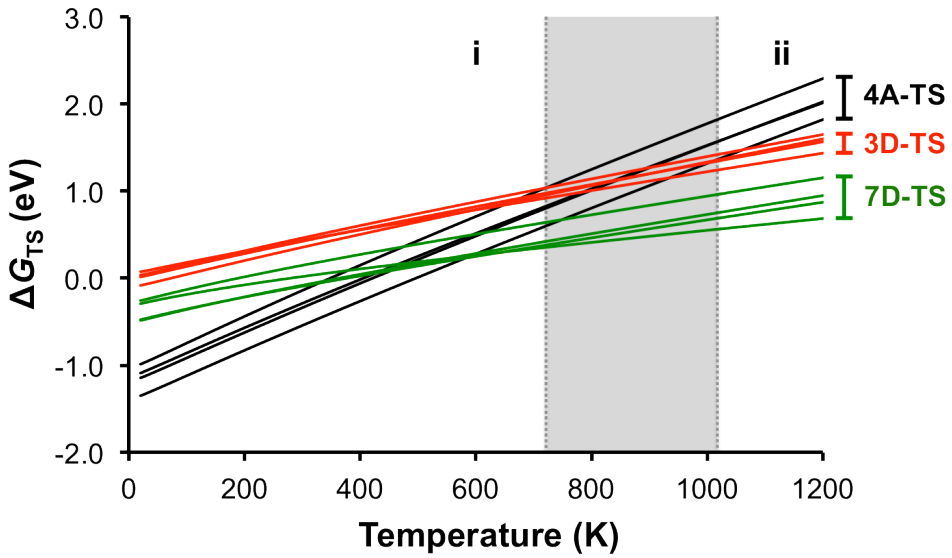

Figure 5.7 Variation of the transition state Gibbs free energies relative to gaseous methanol and clean H-ZSM-5 (**IS**). Partial pressure of gas phase compounds was set to 0.1 bar. Each set of curves shows the free energy variation for the four investigated Al sitings. A transition of the reaction mechanism from the associative route (i) to the dissociative route (ii) occurs with increase in temperature. The heterogeneity of active site locations and their dissimilar kinetic behavior result in a temperature window (gray zone) wherein dual mechanisms are possible.

These results are in agreement with the DFT study of methanol dehydration to DME using zeolite clusters by Blaszkowski and van Santen[170] and also with the recent study of Jones and Iglesia[176] on H-ZSM-5, where theoretical and experimental evidence points to the associative mechanism as dominant at 433 K. The presence of a dual mechanism region in Figure 5.7 explains the possibility of simultaneously observing kinetic results compatible with a model based on the associative route (Jones and Iglesia[176]) and measuring spectroscopic evidence for the presence of surface methoxy groups, indicative of the dissociative pathway (Kubelková et al.[177]). The seemingly contradictory conclusions reached by the two latter groups for the same catalyst, H-ZSM-5, at similar reaction conditions can likely be attributed to the fact that both reaction pathways are accessible during the reaction.

Moreover, our results in Figure 5.7 can be used to rationalize why the MTH processes involving surface methoxy species needed in the methylation of alkenes over acid zeolites are typically conducted at temperatures above 600 K.[157, 176, 195] The lowest temperature for the dissociative reaction (including methoxy formation) to take place is around 700 K, while below this temperature methanol is converted to DME through the associative path without forming the methoxy intermediate.

It must be noted that the 700 K value in our calculations as the lower limit of the dual mechanism region is a theoretical estimate, and should not be interpreted to be quantitatively accurate. In an actual H-ZSM-5 catalyst, it is likely that a number of T sites other than the four chosen in this study will also be occupied by aluminum, and the possibility of neighboring acid sites leading to cooperative effects exists.[196-197] This higher level of heterogeneity may widen the dual mechanism window and shift the lower

end of the temperature window below 700 K. In addition, Moses and Nørskov concluded from a similar analysis that the crossover occurs at temperatures near 300 K for H-ZSM-22.[174] H-ZSM-22 is a one-dimensional zeolite with a pore structure similar to the straight channel of H-ZSM-5; therefore, the subtle difference in framework topology is an unlikely reason for the large deviation in the crossover temperature. The discrepancy is much more likely caused by the neglect of vdW effects in the computational method used by Moses and Nørskov (GGA-RPBE). For confirmation we removed the vdW contributions from our computational results and obtained a crossover temperature for the four T sites considered in our study at 200 – 250 K, in reasonable agreement with the value reported by Moses and Nørskov. The crossover temperature shift stems from the different contributions of dispersion forces to transition state stabilization in the associative and dissociative pathways. We note the vdW-DF type functionals have been shown to overestimate the effect of vdW attraction by ca. 10 – 15 kJ/mol for C_2 complexes in zeolites.[39-40] Thus, we expect that a more accurate description of dispersion forces will shift the crossover temperature to lower values such that the dual mechanism zone overlaps with the typical condition of the methanol-to-DME reaction (~500 K).

The impact of vdW interactions on the stability of transition states prevails inside the porous structure of the zeolite catalyst and is less significant on the exterior zeolite surface. For small catalyst particles having a significant external surface area we anticipate a larger contribution of the dissociative route on the exterior surface of the zeolite crystals at lower temperatures. The effect can be intensified by the phenomenon known as “Al zoning” during ZSM-5 synthesis, which leads to Al enrichment in the crystal rim compared to the crystal interior.[92, 198] For such small ZSM-5 crystals

exhibiting Al zoning, there is presumably a larger contribution of acid sites on the exterior surface, in which case the mechanistic crossover temperature would shift to values well below 700 K. Under these conditions, both mechanisms would be active under typical reaction conditions.

5.3.5 Reaction mechanism variation with pressure

In the discussion of the dominant reaction mechanism in sections 5.3.1–5.3.4, the partial pressure of each gaseous compound was assumed to be 0.1 bar. Although this is a reasonable assumption for the methanol partial pressure in its catalytic conversion on zeolites, the process can be conducted over a range of pressures. In the kinetic model proposed by Jones and Iglesia,[176] a linear correlation between the rate of reaction at 433 K over H-ZSM-5 and methanol pressure is observed for up to ca. 0.03 bar. For higher pressures there is a gradual increase in the rate, consistent with the Langmuir-type behavior of the associative pathway. A change in pressure can also change the crossover temperature between the two reaction pathways. We now assess the sensitivity of the crossover temperature to pressure changes. The partial pressure has a direct effect on the entropy of gas phase species according to equation (5.5) for an ideal gas

$$S_{\mathrm{gas}}(T,P) = S_{\mathrm{gas}}^{\circ}(T) - k_b \ln\left(\frac{P}{P^{\circ}}\right), \tag{5.5}$$

where P is the pressure, $P°$ is the pressure at standard state, k_b is the Boltzmann constant, S_{gas} is the entropy, and $S_{\mathrm{gas}}°$ is the entropy at standard pressure. While the entropy of the solid catalyst and the adsorbed species do not vary with pressure, the entropy of gas-phase compounds decreases as pressure increases. Thus, surface bound transition states become more stable with increasing pressure. The extent of the Gibbs free energy change and transition state stabilization will be larger for the transition state of the associative

path, because it consumes one gas molecule more than each step of the dissociative path. This entropic difference causes the associative mechanism to be dominant over a wider temperature range and a shift of the mechanism crossover temperature to higher values with increasing pressure.

Figure 5.8 shows that the crossover temperature for each individual T site increases linearly with the logarithm of pressure, but we discern at least two different slopes; T10 and T11 in channel locations have larger slopes compared to T3 and T12 at channel intersections. We now investigate the reason. If ln(P) becomes larger by an amount of k (i.e., $k = \ln(P_2) - \ln(P_1)$), we obtain

$$S_{\text{gas},2}(T, P_2) - S_{\text{gas},1}(T, P_1) = k_b \ln(P_1) - k_b \ln(P_2) = -k_b k. \quad (5.6)$$

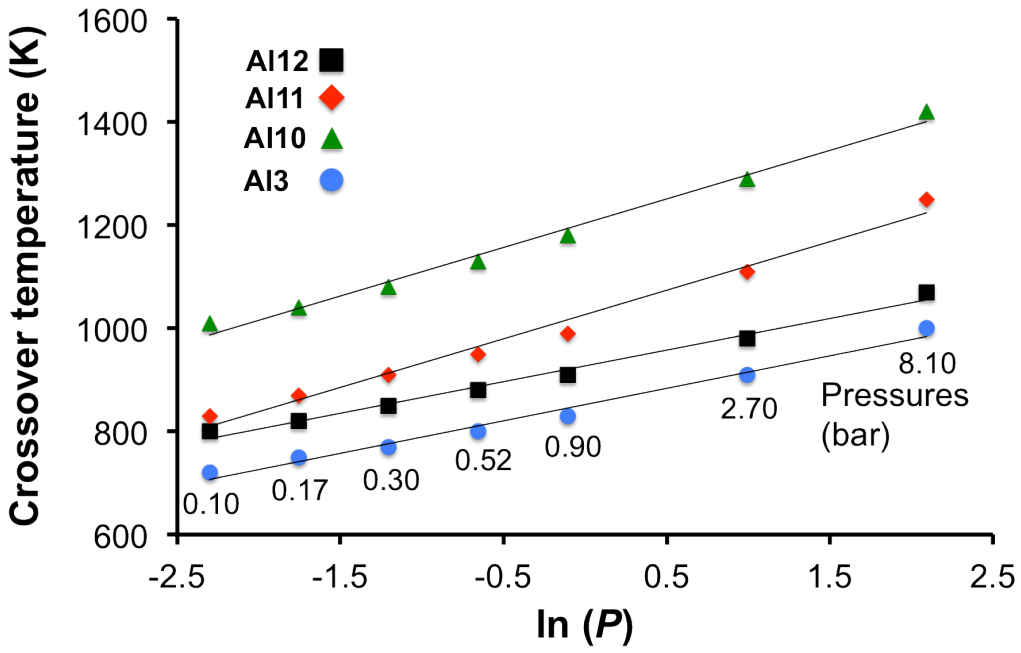

Figure 5.8 Methanol dehydration mechanism crossover temperature as a function of partial pressure. Each pressure condition applies to every gas compound involved in the reaction.

We also have

$$G_{\text{gas}} = H_{\text{gas}} - TS_{\text{gas}}, \tag{5.7}$$

where G_{gas} and H_{gas} are the gas Gibbs free energy and gas enthalpy, respectively.

For the Gibbs free energy change of the transition state (ΔG_{TS}) with reference to the Gibbs free energies of the clean zeolite (G_{clean}) and the gas phase reactant (G_{gas}), $\Delta G_{\text{TS}} = G_{\text{TS}} - G_{\text{clean}} - G_{\text{gas}}$, we can write

$$\Delta G_{\text{TS},2} - \Delta G_{\text{TS},1} = -2Tk_b k, \tag{5.8}$$

for the associative path, and

$$\Delta G'_{\text{TS},2} - \Delta G'_{\text{TS},1} = -Tk_b k, \tag{5.9}$$

for the H_2O elimination reaction of the dissociative path. Note that we only consider the transition state Gibbs free energy change of the H_2O elimination reaction in the dissociative path since it always has a greater value than that of the DME formation reaction, and the crossover temperature is determined by the higher energetic barrier relative to the transition state Gibbs free energy change of the associative path. We also note that the associative Gibbs free energy change is twice that of H_2O elimination since the former consumes two gas molecules while the latter consumes only one.

The ΔG_{TS}-temperature curves may be approximated as straight lines according to

$$\Delta G_{\text{TS},1} = \alpha T + \beta, \tag{5.10}$$

and

$$\Delta G_{\text{TS},2} = \Delta G_{\text{TS},1} - 2Tk_b k = \alpha T + \beta - 2Tk_b k, \tag{5.11}$$

for the associative path. Similarly, for the dissociative path we obtain

$$\Delta G'_{\text{TS},1} = \alpha' T + \beta', \tag{5.12}$$

and

$$\Delta G'_{\mathrm{TS},2} = \Delta G'_{\mathrm{TS},1} - Tk_b k = \alpha' T + \beta' - Tk_b k. \quad (5.13)$$

At the temperature where the two curves intersect, the Gibbs free energy changes of the two pathways are equal. At pressure condition 1:

$$\alpha T_1 + \beta = \alpha' T_1 + \beta' \rightarrow T_1 = \frac{\beta' - \beta}{\alpha - \alpha'}, \quad (5.14)$$

and at pressure condition 2:

$$\alpha T_2 + \beta - 2T_2 k_b k = \alpha' T_2 + \beta' - T_2 k_b k \rightarrow T_2 = \frac{\beta' - \beta}{\alpha - \alpha' - k_b k}. \quad (5.15)$$

Therefore, we have the following expression for the crossover temperatures at pressures P_1 and P_2:

$$\frac{T_2 - T_1}{\ln(P_2) - \ln(P_1)} = \frac{T_2 - T_1}{k} = \frac{1}{k}\left(\frac{\beta' - \beta}{\alpha - \alpha' - k_b k} - \frac{\beta' - \beta}{\alpha - \alpha'}\right) = \frac{k_b(\beta' - \beta)}{(\alpha - \alpha' - k_b k)(\alpha - \alpha')}. \quad (5.16)$$

Finally, we let $\mathrm{d}P \rightarrow 0$, which implies that $k = \ln(P_2) - \ln(P_1) \rightarrow 0$ and we arrive at the final expression for the slope of the crossover temperature as a function of ln(P):

$$\frac{\mathrm{d}T}{\mathrm{d}\ln(P)} = \frac{k_b(\beta' - \beta)}{(\alpha - \alpha')^2}. \quad (5.17)$$

A comparison between equation (5.7) and the linearized equations (5.10) and (5.12) suggests the linearization parameters $\alpha = -\Delta S$ and $\beta = \Delta H$, if we assume the entropy and enthalpy changes to be constant, i.e., independent of temperature. Indeed, we can use equation (5.17) and Tables 5.1 – 5.4 to calculate the slopes and show the result in Table 5.6. Here, the enthalpy change ΔH (or β) was approximated as the sum of the electronic and zero point energies at the ground state. The slope values in Table 5.6 are in good qualitative agreement with the curves in Figure 5.8. The two sites at the channel intersection (T12, T3) have smaller slopes than the locations inside the channels (T11, T10). Because equation (5.17) shows that both entropic and enthalpic effects contribute to the pressure sensitivity of the crossover temperature it is not possible to attribute the

grouping of slopes in Figure 5.8 to only entropic confinement or environment dependent van der Waals stabilization at intersections vs. channel locations.

Table 5.6 Estimated slope of the crossover temperature vs. ln(P) curves for various Al sitings.

Al siting	α[a]	α'[a]	β[b]	β'[b]	$\frac{dT}{dln(P)}$
Al12	0.00273	0.00116	-1.20	0.04	43.35
Al11	0.00269	0.00144	-1.13	-0.10	56.80
Al10	0.00273	0.00133	-1.40	-0.02	60.67
Al3	0.00282	0.00138	-1.04	0.00	43.22

[a] α and α' are in eV/K.
[b] β and β' are in eV.

Figure 5.8 indicates that the crossover temperature is strongly dependent on Al siting. As such, an accurate prediction of the crossover temperature requires characterization techniques with very high spatial resolution to resolve Al sitings in the actual catalyst. In turn, advanced synthesis methods are needed to control the location of Al incorporation during ZSM-5 growth for rational catalyst design. Assuming Al could be purposely placed at certain T sites during zeolite synthesis, the activity region of the dissociative pathway (including methoxy formation) could be moved to lower temperatures per DFT predictions. Selecting synthesis conditions that result in Al zoning in ZSM-5 crystals may also diminish the effect of vdW interactions and favor the dissociative reaction. This information provides us with fundamental insight for the rational design of ZSM-5 catalysts applied in the MTH process, where less severe temperature conditions could minimize coke formation and extend the catalyst lifetime.

5.3.6 Effect of active site acidity on kinetic performance

The term 'acidity' may be interpreted as the density of acid sites or the intrinsic acid strength of each individual acid site. The latter is investigated in this section. Unfortunately, solution-phase acidity quantification such as the Hammett function are not accessible to characterize the acid strength of solid acids.[151] However, a number of experimental techniques such as temperature-programmed desorption (TPD) of amines/alkylamines,[95] IR spectroscopy of adsorbed pyridine and 2,6-ditertbutyl pyridine,[199-200] and estimation of a basic compound adsorption energy through calorimetry[151, 201] have been introduced as alternatives. Among the computational methods for zeolite acid strength assessment, the deprotonation energy (DPE) has widely been used as a measure of intrinsic acidity.[202-204] The determination of the DPE through periodic DFT calculations, however, is unpractical because it requires simulations in charged systems. As discussed in chapter 4, we have previously investigated various measures of acidity, e.g., binding energies of probe bases (NH_3, pyridine) and O—H frequency shifts upon CO adsorption, and found that no common acidity scale exists.[184]

To emulate common experimental practice we base our investigation of the impact of active site acidity on its activity on the binding energy of pyridine. Since the zero point energy, heat capacity, and entropy contributions are not immediately correlated with the active site intrinsic acid strength, we base this discussion on electronic energies rather than on the Gibbs free energies. We note that varying acid site locations within the zeolite framework may impose different extents of solvation and electrostatic interactions on reaction intermediates and transition states, which will be difficult to separate from the effect of intrinsic site acidity. Thus, we employ an approach that allows us to alter acid

strength at the same location of zeolite structure. It has previously been shown that heteroatom substitutions at T sites with elements other than aluminum can alter MFI active site performance in catalytic conversion of methanol to light olefins.[205] Jones et al.[97] measured exponentially decreasing rate constants with increasing calculated deprotonation energy (lower intrinsic acidity) when using different heteroatom dopants (Al, Ga, Fe, and B) in MFI. A similar correlation between reaction barriers of the methanol-to-DME reaction and deprotonation energy of more acidic Keggin tungsten polyoxometalate clusters was reported by Carr et al.[171] Moses and Nørskov[174] used Al, Ga, and In substitutions in their DFT study of methanol dehydration over zeolite TON, and obtained a linear correlation between transition state energies associated with these substitutions and the ammonia binding energy as the measure of acidity. However, the range of transition state energy variation for each reaction step was only around 0.2 eV from the most acidic condition (Al substitution) to the least acidic one (In substitution). We found that the range of ammonia binding energies for these three heteroatom substitutions in MFI was within the error of DFT simulations (~0.1 eV) and did not provide a meaningful measure of acidity of the different active sites. Likewise, Wang et al.[206] used DFT-computed ammonia binding energy as the reactivity descriptor of acid sites formed by Al and Ga substitutions in zeolites CHA, AEI, and AFI, but the difference between the NH_3 binding energies of the two substitutions was only around 0.1 eV for each zeolite framework. To improve upon these previous attempts we also used Al, Ga, and In as heteroatom dopants, but instead characterized the change in acidity using the pyridine binding energy, which spans a larger range than that of ammonia. The

outcome is presented in Figure 5.9, which shows the transition state electronic energy variation with acidity for M (M = Al, Ga, In) substituted at the T12 location.

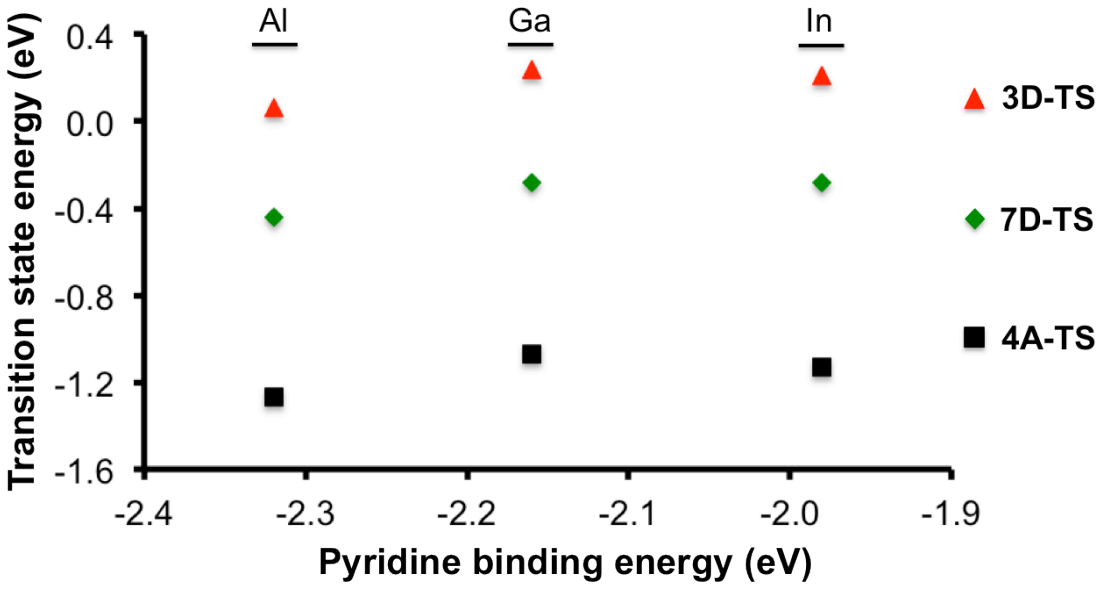

Figure 5.9 Transition state electronic energies of the associative route (**4A-TS**, black squares), and the H_2O elimination (**3D-TS**, red triangles) and DME formation (**7D-TS**, green diamonds) steps of the dissociative route as a function of pyridine binding energy (i.e., measure of acidity). Data are presented for heteroatoms M substituted at the T12 location. Transition state energies are expressed with reference to gaseous methanol and the clean MFI structure (**IS**).

As expected, the data in Figure 5.9 show that the most stable transition states in both pathways are obtained for Al substitution, which also gives the highest acidity. A stronger pyridine binding energy may be interpreted as an easier donation of a Brønsted proton (deprotonation) and a higher stabilization of the pyridinum ion next to the negatively charged zeolite framework. The interaction of the transition states in the methanol-to-DME reaction with the zeolite framework is of a similar nature; here, a positively charged species (transition state complex) must be stabilized instead of the

pyridinum ion. Somewhat unexpected, however, is the result that the transition state energies in the case of Ga and In substitutions do not differ significantly from Al and no clear trend was obtained. The variation of transition state energies is as little as ~0.2 eV. This is consistent with the theoretical study by Wang et al.,[207] who have also shown that Al, Ga, and In doping of CHA zeolite results in an insignificant acidity change, and almost equal transition state energies for the methylation of propene by methanol. We have also confirmed the minimal variation of calculated transition state energies with pyridine binding energy for heteroatom substitutions at the T10 and T11 locations (see Figures 5.10 and 5.11).

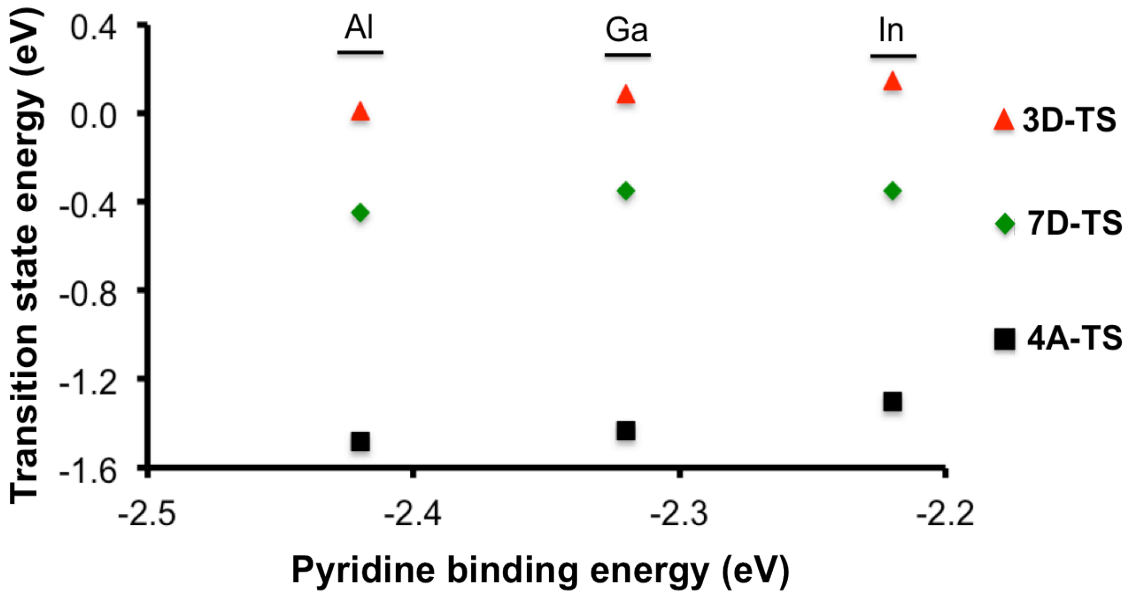

Figure 5.10 Transition state electronic energies of the associative route (**4A-TS**, black squares), and H_2O elimination (**3D-TS**, red triangles) and DME formation (**7D-TS**, green diamonds) steps of the dissociative route as a function of pyridine binding energy (i.e., measure of acidity). Data are presented for heteroatoms M substituted at the T10 location. Transition state energies are expressed with reference to gaseous methanol and the clean MFI structure (**IS**).

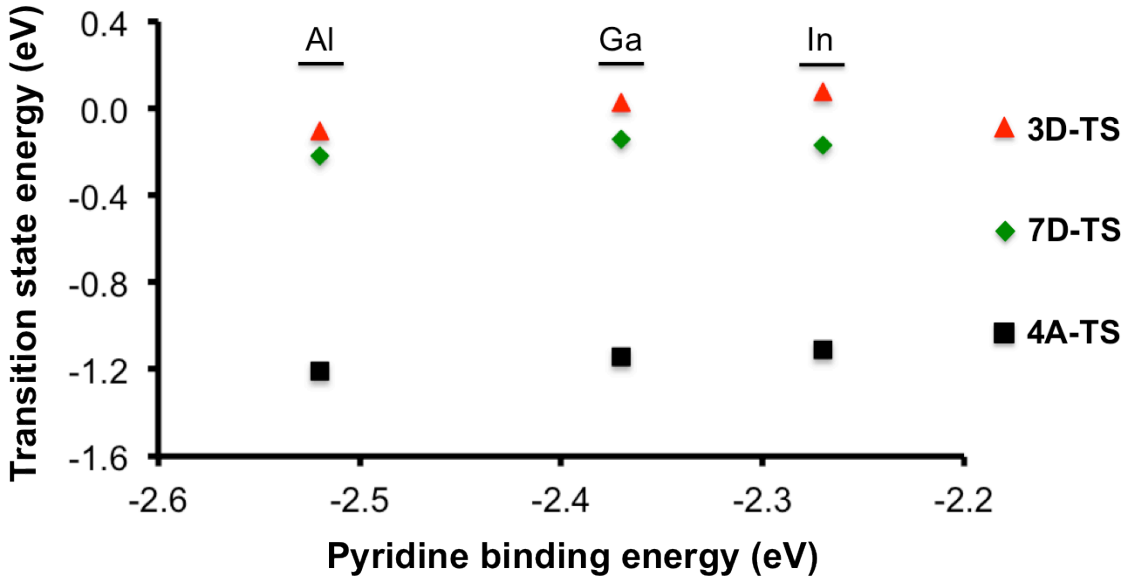

Figure 5.11 Transition state electronic energies of the associative route (**4A-TS**, black squares), and H_2O elimination (**3D-TS**, red triangles) and DME formation (**7D-TS**, green diamonds) steps of the dissociative route as a function of pyridine binding energy (i.e., measure of acidity). Data are presented for heteroatoms M substituted at the T11 location. Transition state energies are expressed with reference to gaseous methanol and the clean MFI structure (**IS**).

The absence of a linear trend between the transition state energy and acidity (binding strength of pyridine) may be attributed to the compensation of the Brønsted acid site deprotonation energy with the stabilization of the positively-charged transition state located next to the zeolite Lewis base site.[97, 170] The consistency of this observation for different active site locations suggests that the extent of compensation is independent of solid acid structure and the local environment of the pore.[97, 171] Finally, one may argue that the vdW interactions between the transition state complex and the zeolite pore walls could mask the acidity effects and render different heteroatoms more similar in nature.[206]

Yet, Figures 5.12 – 5.14 show identical behavior in the absence of vdW interactions and therefore provide no support for this argument.

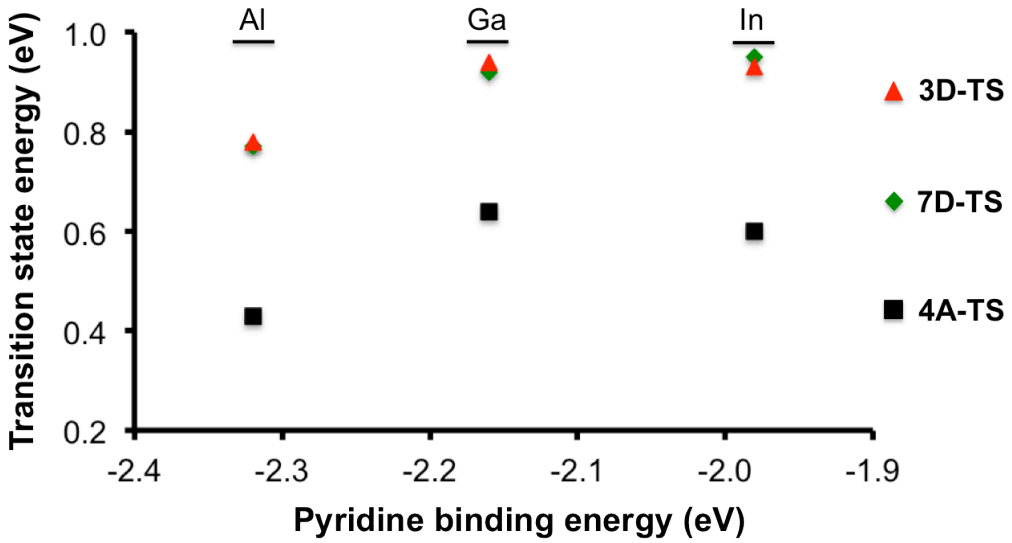

Figure 5.12 vdW-removed transition state electronic energies of the associative route (**4A-TS**, black squares), and H_2O elimination (**3D-TS**, red triangles) and DME formation (**7D-TS**, green diamonds) steps of the dissociative route as a function of pyridine binding energy (i.e., measure of acidity). Data are presented for heteroatoms M substituted at the T12 location.

Overall, we find that the transition state stabilization is a stronger function of the acid site location (the largest transition state **4A-TS** varies by ~0.4 eV when the heteroatom is Al), while it has a weaker dependence on the intrinsic acidity (variations of only ~0.2 eV were obtained when considering the substitution of Al, Ga, In at the same location). Thus, the existence of linear scaling relations of certain transition state energies with base sorbate binding energies is not necessarily an indication for a fundamental relationship between intrinsic acid strength, which is best assessed by DPE calculations, and zeolite activity.[207-208]

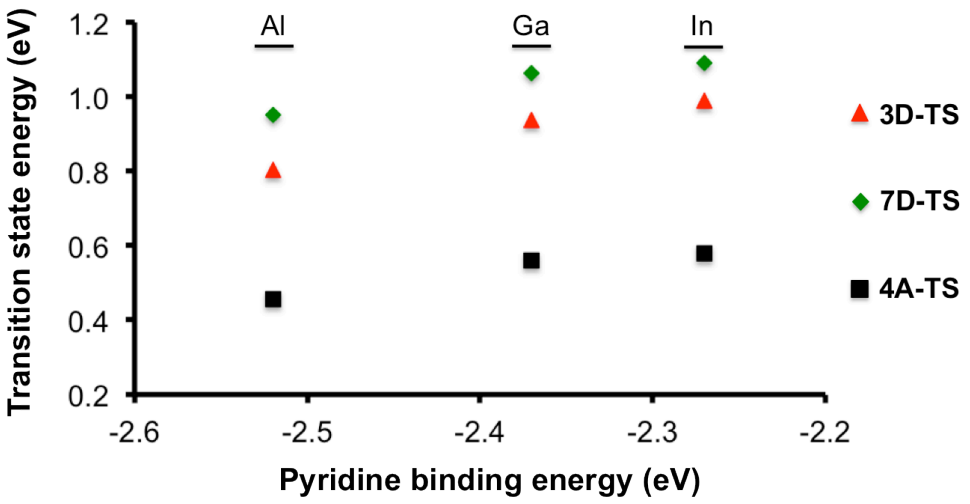

Figure 5.13 vdW-removed transition state electronic energies of the associative route (**4A-TS**, black squares), and H_2O elimination (**3D-TS**, red triangles) and DME formation (**7D-TS**, green diamonds) steps of the dissociative route as a function of pyridine binding energy (i.e., measure of acidity). Data are presented for heteroatoms M substituted at the T11 location.

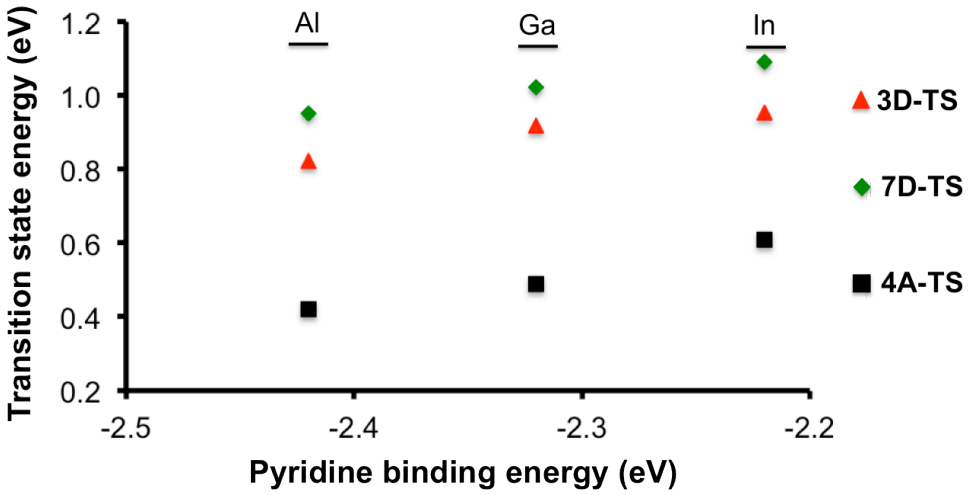

Figure 5.14 vdW-removed transition state electronic energies of the associative route (**4A-TS**, black squares), and H_2O elimination (**3D-TS**, red triangles) and DME formation (**7D-TS**, green diamonds) steps of the dissociative route as a function of pyridine binding energy (i.e., measure of acidity). Data are presented for heteroatoms M substituted at the T10 location.

5.4 Conclusions

This mechanistic investigation of the methanol dehydration reaction over MFI zeolite through periodic DFT calculations demonstrates non-identical behavior of active sites located at the T12, T11, T10, and T3 positions of the MFI zeolite framework. On the basis of Gibbs free energies calculated along the competing associative and dissociative pathways, the former mechanism is dominant for a set of representative reaction conditions regardless of the active site location. The increase of entropic contributions at higher temperatures, however, results in a crossover temperature for each active site location, above which the dominant mechanism shifts from associative to dissociative. This crossover temperature varies for the studied Al sitings and results in a dual mechanism window where both mechanisms can be active at different sites. The simultaneous occurrence of both pathways under the same reaction conditions offers an explanation to previous contradictory observations of methoxy intermediates indicative of the dissociative pathway and rate behavior indicative of the associative pathway. Increasing pressure favors the associative route and shifts the window of crossover temperatures to higher values. The importance of vdW contributions to transition state stabilization has been confirmed and we demonstrate the extent to which dispersion forces affect mechanistic conclusions. Notably, the crossover temperature may shift by as much as ~500 K to lower values when vdW contributions are neglected. In contrast, varying active site acid strength via different heteroatom substitutions and quantified by the binding energy of pyridine did not result in a considerable change in the kinetic behavior of the methanol dehydration reaction over zeolite MFI. These mechanistic and fundamental insights regarding the relative importance of acidity and confinement on

catalytic reactions in zeolites can ultimately inform the rational design of improved zeolite catalysts and the optimization of reaction conditions for methanol conversion processes.

Chapter 6 Structural, adsorption, and kinetic properties of paired acid sites in H-ZSM-5

6.1 Introduction

The zeolite models used in chapters 4 and 5 consider only one aluminum atom in the MFI unit cell, i.e an Si/Al ratio of 95, which is a much lower aluminum content of ZSM-5 than that in many of its industrial applications. It has been reported in some studies that the catalytic activity of high-silica zeolites such as ZSM-5 increases linearly with the Al content e.g., in alkane cracking reactions.[127] This implies that the active sites act independently and form no collaborative interaction with the reaction species. However, Al content and its distribution in the zeolite crystal structure have been shown to be dependent on the synthesis conditions to a great extent. Therefore, it is reasonable to postulate that there will be a higher probability of finding neighboring acid sites in the ZSM-5 structure at lower Si/Al ratios. Dědeček et al.[209] were able to increase the fraction of Al located in the next-next nearest-neighbor paired configuration (Al—O—(Si—O)$_2$—Al) to 68% by means of using TEOS as silicon source, $AlCl_3$ as aluminum source (vs. $Al(NO_3)_3$), TPAOH as structure directing agent, eliminating Na^+ from the synthesis solution, and through testing various sequences of synthesis components mixing. The product contained an Si/Al ratio of 25 ($(Si/Al)_{gel}$ = 30). We can assume that a higher fraction of paired Al sites, as defined above, or even next nearest-neighbor configuration of Al sites (Al—O—Si—O—Al) may occur at lower Si/Al ratios or by using different synthesis conditions. We note that a nearest-neighbor configuration, i.e., Al—O—Al, is not possible due to Löwenstein's rule in zeolite structures.

The presence of two or more acid sites close to each other in the zeolite framework can alter the electron density and lattice polarization near the acid site. Opalka and Zhu studied the structural and electronic changes in the H-ZSM-5 structure with varying Al content and its distribution through DFT modeling.[210] They obtained a lower lattice and Brønsted O—H polarization at lower Si/Al ratios; this trend, however, went inverse when the additional Al sites were placed in the next-next nearest-neighbor configuration. The adsorption energy of isopropyl amine was found to be more negative as large as ~30 kJ/mol on paired T6 sites than on an isolated T6 sites with the same Si/Al ratio. The same qualitative trend was observed for the physisorption of n-pentane.

The kinetic consequences of the presence of neighboring acid sites in zeolites compared to the isolated acid site model have not been investigated extensively. In one of the few studies, the selectivity of 1-butene cracking over H-ZSM-5 has been shown to decrease in favor of the hydrogen transfer and aromatization reactions with increase in the fraction of next-next nearest-neighbor Al sites.[211] Jones et al. showed a sudden increase in the measured first-order rate constant of methanol dehydration over H-ZSM-5 with increase in the Brønsted acid site concentration to 3.6 per unit cell.[97] They, however, attributed this observation solely to the preferred siting of framework Al atoms at more confined locations of the MFI framework at higher Al contents. The effect of Al siting at nearby locations in H-ZSM-5 on the kinetics of methanol-to-DME reaction has not been reported in any previous study in the literature. Here, we introduce models of next nearest-neighbor Al siting in H-ZSM-5 and look into its impact on zeolite active site structural properties, binding energies of probe molecules discussed in chapter 4, and kinetic behavior in the most likely dominant mechanism of the methanol-to-DME

reaction at its typical reaction conditions proposed in chapter 5, i.e., the associative pathway, as well as the rate determining step of its dissociative route, i.e., the H_2O elimination step.

6.2 Computational methods

The computational methods reported in chapters 4 and 5 were also used here. Electronic charges of atoms were computed through Bader charge analysis. The Bader charge is calculated within the Bader volume of each atom, and the latter is defined by a 2-D zero flux surface on which the charge density is a minimum perpendicular to the surface.[212]

There are many ways to construct next nearest-neighbor models of Al siting in H-ZSM-5. In order to facilitate a comparison with the performance of single acid sites, we focused on the Al—O—Si—O—Al models that could be made starting with Al at the T12 site. This Al atom is connected to four Si atoms through bridging oxygens and each of these four Si atoms is in turn linked to three other T sites. T1 and T12 are not among these 12 T sites, while T2 and T7 are found twice. Therefore, we selected our acid site pair models as Al12—Si3—Al2, Al12—Si8—Al2, Al12—Si8—Al7, and Al12—Si11—Al7 (bridging oxygen atoms are not shown). This choice enables us to also compare the performance of the same two Al sites linked through two crystallographically different Si atoms. For the acid site pair models mentioned above, we use 12—3—2, 12—8—2, 12—8—7, and 12—11—7 as active site identifiers, respectively.

6.3 Results and discussion

6.3.1 Properties of clean structures

For each of the acid site pair models, there are 16 possible combinations of proton locations since each of the two protons has four Al-linked oxygen atoms to sit on. Our previous calculations for single acid sites given in Table 4.4, showed that there are no significant variations among the stabilities of various proton locations for a specific T site, and the Brønsted acid proton can readily be exchanged among the bridging oxygen atoms. This is not, however, true for the acid site pair models considered in our study. We calculated the stabilities of all 16 possibilities for each of the models and the stabilities span variation ranges as large as 0.56, 0.36, 0.67, and 0.54 eV for 12—3—2, 12—8—2, 12—8—7, and 12—11—7, respectively. The most narrow variation range belongs to the only model where the two Al atoms are located in two different channels and cannot provide collaborative interactions with adsorbates/reaction species, i.e., 12—8—2. We also noted that in the most stable configuration of each model, the two protons occupied distant positions, which is a reasonable observation due to the repulsive force between protons. Using the most stable configurations, the stability of each paired acid site structure was compared with the stability of an H-ZSM-5 unit cell containing the same Al sitings but at distant positions (unpaired). The energies of both structures were very close (less than 0.1 eV different) for all the four acid site pair models. Therefore, the pairing of acid sites neither was favorable nor imposed a penalty in terms of structure stability against isolated acid sites.

Table 6.1 shows the calculated Brønsted O—H bond length, the Si—OH—Al bond angle, and the Brønsted O—H polarization of the Al12 site for the acid site pair models.

The O—H polarization is calculated as the difference between the partial charges of the O and H atoms of the Brønsted acid site. In order to make a direct comparison with the properties of the isolated site, we placed the Al12 associated proton over the same oxygen atom as that considered in the isolated Al12 site as indicated in Table 4.3 (active site identifier 12—12; i.e., Al12 connected to Si12 via the bridging oxygen). The second proton location was selected so that the highest stability would be obtained. Table 6.1 includes the data for the 12—12 isolated site as well.

As seen in Table 6.1, the O—H bond length remains almost constant when a second acid site is created close to the Al12 site. The maximum 0.002 Å decrease in the bond length is not large enough to deduce a decrease in acid strength based on this structural parameter, in particular when compared to the 0.029 Å variation range that is observed in Table 4.3 over different acid site locations. The Si—OH—Al bond angle does not show a trend from the isolated site to the paired sites. While the 12—8—7 model gives the widest angle, 1.1° larger than that of 12—12, 12—11—7, i.e., the model with the same Al sites linked through a different Si shows the smallest angle of all models.

The O—H polarizations indicated in Table 6.1 are identical for the two acid site pair models formed by Al12 and Al2, which are also almost equal to the isolated Al12 O—H polarization. The O—H polarizations of both models formed by Al12 and Al7 possess considerably higher values than those of 12—3—2, 12—8—2, and 12—12. If the Brønsted acid site polarization is used as a measure of acidity, this observation may be interpreted as the higher acidity of Al12 site when it is paired with Al7 regardless of the linking Si, while the acidity remains constant when the second acid site is located T2. We

will see in the next section if this trend leads to corresponding results in terms of probe base binding energies.

Table 6.1 Brønsted acid O—H bond length, Si—OH—Al bond angle, and Brønsted O—H polarization of the Al12 acid site for the paired and isolated acid site models of H-ZSM-5.

	12—3—2	**12—8—2**	**12—8—7**	**12—11—7**	**12—12**
O—H bond length (Å)	0.977	0.977	0.978	0.976	0.978
Si—OH—Al bond angle	132.8	132.3	135.8	131.6	134.7
O—H polarization	2.07	2.07	2.20	2.17	2.08

6.3.2 Adsorption behavior of paired acid sites

Binding energies of the five probe molecules mentioned in chapter 4, on the Brønsted acid site located at T12 were calculated for the four acid site pair models. These results are shown in Table 6.2. Binding energies were computed with reference to the clean zeolite structures with the most stable proton locations. Numbers within parentheses reflect the vdW-excluded binding energies.

The positions of adsorbates with respect to the active site and zeolite channels in the acid site pair models were selected exactly as those in the single acid site model for a direct comparison. The ultimate orientations of adsorbates after geometry optimization were very similar in both the paired and single acid site models. The converged geometry of CH_3OH adsorbed over the four paired acid sites is shown along the b view in Figure 6.1.

Table 6.2 Binding energies of several probe molecules on the Al12 Brønsted acid site for the paired and isolated acid site models of H-ZSM-5. Values in parentheses are obtained in the absence of vdW corrections.

Active site identifier	CH_4	NH_3	CO	C_5H_5N	CH_3OH
12—3—2	-0.57 (0.03)	-1.71 (-1.12)	-0.65 (-0.14)	-2.41 (-0.54)	-1.48 (-0.58)
12—8—2	-0.40 (0.18)	-1.49 (-0.94)	-0.47 (0.02)	-2.23 (-0.37)	-1.17 (-0.39)
12—8—7	-0.71 (-0.09)	-1.69 (-1.13)	-0.78 (-0.24)	-2.34 (-0.50)	-1.46 (-0.54)
12—11—7	-0.49 (0.10)	-1.54 (-0.97)	-0.57 (-0.06)	-2.24 (-0.40)	-1.26 (-0.43)
12—12	-0.40 (0.01)	-1.63 (-1.12)	-0.62 (-0.13)	-2.32 (-0.50)	-1.36 (-0.58)

The binding energies in Table 6.2 indicate that different adsorption behavior may be shown by the same acid site, here Al12, when it is paired with another acid site. There is no systematic trend in weakening or strengthening of binding energies in the presence of the second acid site. Yet, for most of the adsorbates, 12—3—2 and 12—8—7 generally result in a stronger binding than 12—12, while 12—8—2 and 12—11—7 tend to form weaker interactions than the isolated acid site. The only exception is CH_4 whose binding energy did not decrease in magnitude when Al12 was paired with Al2 and Al7 sites. CH_4 is the only nonpolar molecule among the tested molecules and is adsorbed in the zeolite porous framework mostly via long-range vdW interactions. The vdW-excluded adsorption energies of CH_4 over some of the paired sites are more positive than that over the isolated 12—12 site. We may thus attribute the stronger binding of CH_4 to the stronger vdW interactions emerging in the presence of neighboring acid sites. Opalka and Zhu argued that lower lattice ionicity, or higher lattice covalency, leads to stronger vdW interactions imposed by the zeolite framework.[210] Hence, we calculated the unit cell

lattice ionicity as the sum of the atomic partial charge absolute values, which turned out to be 613.37, 613.69, 613.75, 613.64, and 613.89 for the 12—3—2, 12—8—2, 12—8—7, 12—11—7, and 12—12 models, respectively. We find that all site pair models result in a lower ionicity than the lattice with the isolated Al12 site. Thus, the observed trend is in agreement with the argument of Opalka and Zhu. The proposed correlation between lattice ionicity and vdW interactions, however, seems counterintuitive since one would expect stronger vdW interactions at higher lattice polarization, which in turn means more heterogeneous distribution of atomic charges, i.e., higher ionicity.

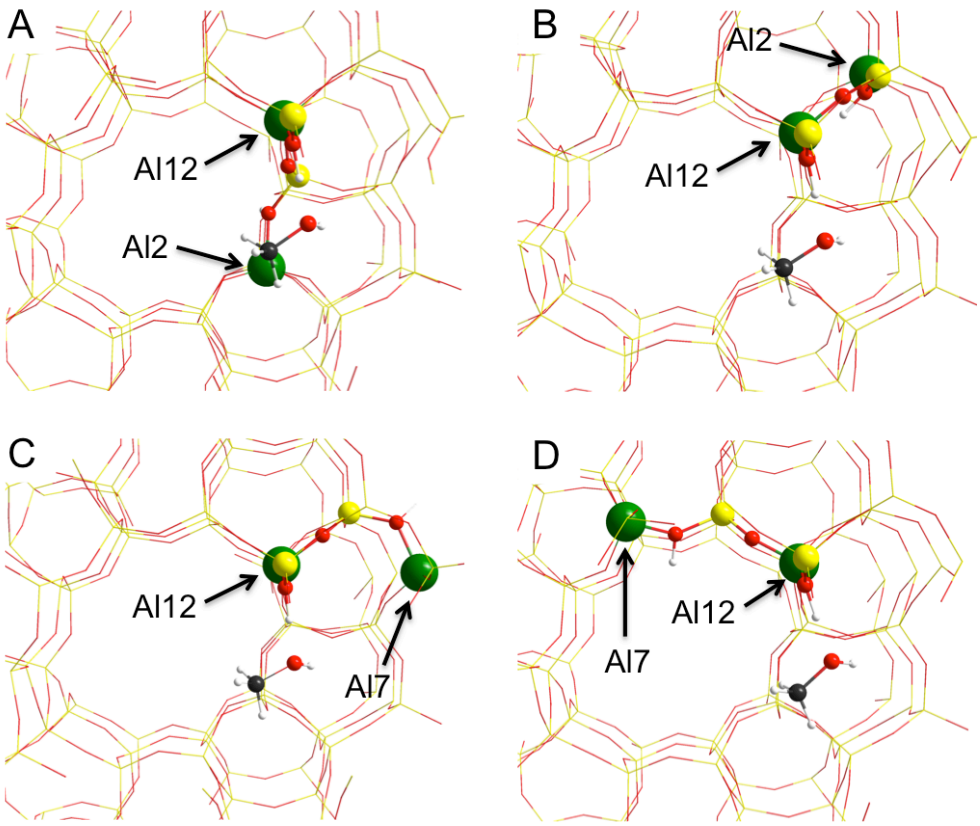

Figure 6.1 The optimized geometry of a methanol molecule adsorbed over the Al12 Brønsted acid site of H-ZSM-5 in: A) 12—3—2, B) 12—8—2, C) 12—8—7, and D) 12—11—7 acid site pair models, along the b direction (Si – yellow, O – red, Al – green, C – black, H – white).

The adsorption of probe molecules other than CH_4, however, is dependent to a great extent on their local interactions with the Brønsted acid site. The nonidentical behavior in the binding of NH_3, CO, C_5H_5N, and CH_3OH to the Al12 Brønsted acid site when paired with other Al sites in the four considered models allows us to speculate about the underlying reasons. The Brønsted O—H polarizations reported in Table 6.1 show no correlation with the binding energies of probe bases such as NH_3 and C_5H_5N. Thus it is not possible to predict the binding strength of H-ZSM-5 paired acid sites from the charge distribution over the Brønsted O—H bond as an intrinsic acidity descriptor.

While we are unable to attribute the variations in binding energy to a particular property of the acid site pairs, it is interesting to note that among the four acid site pair models, the weakest binding of all the five studied molecules occurs over 12—8—2, i.e., the only configuration whose two Al sites belong to two different zeolite channels and are separated by a section of the zeolite framework.

6.3.3 Kinetic behavior of paired acid sites

To investigate the impact of a neighboring acid site on the kinetic behavior of H-ZSM-5, we optimized the transition state of the rate determining step in the dissociative pathway of the methanol-to-DME reaction as introduced in chapter 5, i.e., the H_2O elimination step, as well as that of the associative pathway. This was done for the 12—3—2, 12—8—2, 12—8—7, and 12—11—7 models and the transition state electronic energies were compared to those of the isolated Al12 site discussed earlier in chapter 5. The $CH_3OH_2^+$ adsorption and the coadsorption of methanol molecules over the paired sites were modeled with the same configuration as that over the single Al12 site. Thus, the initial geometries in the NEB calculations for both the paired and single sites were

essentially the same. Table 6.3 shows the converged transition state energies, which are reported with reference to the most stable clean zeolite structure and two gas phase methanol molecules. The transition state geometries, in particular the planar configuration of CH_3 species, were common among all the considered paired and single site models.

Comparison of transition state energies listed in Table 6.3 shows the cooperative effect of the neighboring acid site on lowering the transition state energies of both pathways in most cases. This is true even in the case of 12—8—2 where the second Al site is located in a different channel. The only exception is 12—11—7 which renders more unstable transition states in both pathways compared to the 12—12 site. The largest stabilization is found for 12—3—2, in which the second acid site stabilizes the transition state for H_2O elimination by as much as 0.5 eV, equivalent to a 5 orders of magnitude increase in rate constant at 500 K or an 8 orders of magnitude increase at room temperature.

Table 6.3 Transition state electronic energies of the dissociative pathway H_2O elimination step and of the associative pathway in the methanol-to-DME reaction over the single and paired Al12 sites of H-ZSM-5.

	12—3—2	**12—8—2**	**12—8—7**	**12—11—7**	**12—12**
H_2O elimination	-0.45	-0.23	-0.26	0.22	0.05
Associative	-1.43	-1.38	-1.34	-1.17	-1.28

The kinetic behavior of the paired acid sites cannot be grouped based on which T site is paired with Al12; two of the models with Al2 and Al7 as the second sites in vicinity of Al12 result in almost equal transition state energies (12—8—2 and 12—8—7), while two others (12—3—2 and 12—11—7) show very different kinetic behavior. Yet, the stabilizing (or destabilizing) effect of the presence of a neighboring acid site shows a consistent trend for both H_2O elimination and the associative reaction; if the neighboring

site has a collaborative impact on H_2O elimination, it will have a collaborative impact on the associative pathway as well, and vice versa. Figure 6.2 illustrates this observation.

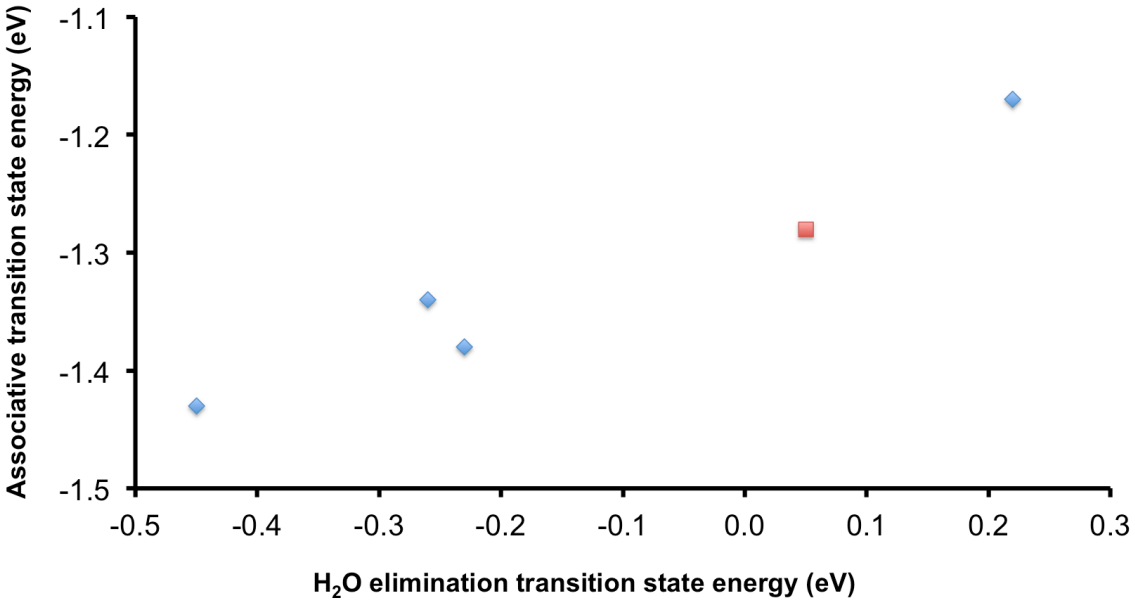

Figure 6.2 The associative route transition state energy vs. the H_2O elimination transition state energy for the four studied paired acid sites (diamonds) as well as the single Al12 acid site (square). Numerical values are given in Table 6.3.

It is interesting to note that the effect of adding the second acid site on stabilizing or destabilizing of the transition states is more significant in H_2O elimination than in the associative reaction for all the paired acid site models. We previously observed that the variation of transition state energies at different locations of single acid sites in H-ZSM-5 is larger for the associative pathway than that for the H_2O elimination step. This was attributed to the pore confinement effects through vdW interactions that have a larger impact on the transition state with a larger size. The local electronic variations due to the presence of a second neighboring acid site, however, appears to have a more significant impact than the change in vdW interactions on the stabilization of methanol dehydration transition states, so that the H_2O elimination step with the smaller transition state size

undergoes a larger energetic variation. This can subsequently influence the location of the associative/dissociative crossover temperature introduced in the mechanistic study of the methanol-to-DME reaction in chapter 5. Additional work and detailed electronic structure analyses are necessary in the future to identify the key property change of the T12 site when neighboring acid sites are present. These investigations are outside the scope of this thesis.

6.4 Conclusions

The structural, adsorption, and kinetic performance of the Al12 Brønsted acid site of H-ZSM-5 shows that the presence of a next nearest-neighbor acid site may result in dramatic variations in acid site properties. The heterogeneous behavior that was reported for the isolated acid sites located at various positions of H-ZSM-5 exists in the case of acid site pairing as well. The adsorption energies of the nonpolar methane molecule show evidence for a possible increased vdW interactions imposed by the zeolite framework in the presence of two neighboring acid sites. The other nonpolar molecules' binding, however, is more dependent on the local adsorbate-acid site interactions and indicates a higher level of heterogeneity. The kinetic behavior of the investigated models in the methanol-to-DME reaction shows a possibility for both stabilization and destabilization of the transition states. This effect shows a consistent trend for the associative route and H_2O elimination step of the dissociative route; the stabilizing (or destabilizing) effect of each paired acid site applies to both reaction pathways. The impact of acid site pairing on transition states was more significant in the H_2O elimination step for all of the studied neighboring site models. This can potentially result in mechanistic variations at typical reaction conditions in the presence of paired Brønsted acid sites.

Chapter 7 Summary and outlook

Improvement of zeolite catalysts' functionality requires a thorough understanding of the impact of framework topology, crystal morphology, and active sites distribution through the zeolite structure, on their activity, selectivity, and lifetime in catalytic reactions. The porous structure of zeolite catalysts provides the possibility for the formation of active sites both on the exterior and in the interior (bulk) of zeolite crystals. External and internal active sites are expected to indicate different behavior due to structural and chemical differences. Moreover, internal active sites of different zeolite structures, or even internal sites within the same zeolite framework are not crystallographically equivalent. The presence of Al atoms at these nonidentical locations is expected to lead to different catalytic performance, which can be utilized in catalytic processes to enhance activity and selectivity.

One method to benefit from a heterogeneous distribution of actives sites is to passivate the active sites on the external surface in order to suppress the reaction of bulky molecules without affecting the reactivity and diffusion of those species whose molecular size correspond to the dimensions of zeolite porous network. In the experimental efforts reported in this dissertation, I have developed a robust protocol to synthesize ZSM-5 catalysts with an Al-free passivating shell of the same structure (silicalite-1). Several characterization techniques demonstrate that the passivating overlayer provides a uniform coverage over the active core particles. In a properly selected probe reaction, the core-shell particles proved to appropriately suppress the access of a bulky reactant with a kinetic diameter greater than ZSM-5 pore openings to the catalyst active sites, while a reaction with adequately small reactants and products indicated the same activity as that

of the core catalyst particles. To minimize the adverse mass transfer limitations resulting from the grown shell, a procedure based on the knowledge of the silicalite-1 crystallization chemistry was also proposed to systematically tune the passivating shell thickness to very low values.

Computational modeling in this work mostly focused on revealing the intrinsic differences among potential active sites in H-ZSM-5 with respect to their chemical binding and ability to stabilize transition states. DFT results showed a large range of variations among the properties of H-ZSM-5 acid sites and their binding strength when interacting with several probe molecules. Many of the quantified properties such as Brønsted acid site O—H bond length, Si—OH—Al bond angle, Brønsted O—H stretch frequency and its shift upon carbon monoxide adsorption, and the binding energies of probe bases such as ammonia and pyridine have traditionally been used as descriptors of the acid strength of zeolite active sites. Despite the large variations, no clear correlations were observed among most of these acidity descriptors, which indicates the difficulty of introducing a unique acidity descriptor for zeolite systems. We ultimately conclude that each active site in H-ZSM-5 is unique and a generalization is not straightforward.

However, our computational method allows us to assess the impact of vdW contributions to adsorption energies and we provide evidence that dispersion forces are proportional to the size of the adsorbed species and play a major role in the adsorption of nonpolar molecules such as methane.

We investigated the heterogeneity of H-ZSM-5 active sites in the reaction of methanol dehydration to DME. DFT results were indicative of significant variations of transition state energies for the associative pathway and the H_2O elimination and DME formation

steps of the dissociative pathway of the reaction. This mechanistic study introduced the associative route and the dissociative route to be the dominant mechanisms at relatively low and relatively high reaction temperatures, respectively. At intermediate temperatures, which overlap with the typical temperature range of the MTH process, however, a dual mechanism region was predicted due to the nonidentical kinetic behavior of the four studied active sites of H-ZSM-5. The evaluation of pore confinement effects through vdW interactions showed they had significant contributions to the stabilization of the transition states, thereby underlining the importance of using vdW-corrected modeling approaches in the precise prediction of zeolite kinetic behavior. The predicted reaction mechanism was found to be dramatically impacted by the acid site location dependent pore confinement effects.

The consequences of zeolite active site distribution were also studied in the case of neighboring Brønsted acid sites in H-ZSM-5. The presence of Al sites in the next nearest-neighbor configuration was found to have significant impacts on the adsorption of probe molecules and stabilization of transition states in the methanol dehydration reaction.

The collection of experimental and modeling studies carried out and reported in this dissertation demonstrates the significant impacts of heterogeneous distribution of the ZSM-5 zeolite active sites on its catalytic activity and selectivity. My experimental design of core-shell structured MFI zeolite showed how this concept could be used to enhance catalytic selectivity while not compromising the activity of internal acid sites. The strategy employed here may be extended to other zeolite frameworks as well. It will also be of interest to try synthesis conditions without the use of OSDAs, which are not

commercially favorable. It must, however, be noted that the control of synthesis conditions will be a more challenging task in the absence of OSDAs.

The high level of heterogeneity of H-ZSM-5 active sites shows the significance of finding experimental techniques to systematically tune the position of framework Al atoms in the zeolite structure. This in turn requires a thorough knowledge of the solution chemistry and the interactions between alumina and silica species, structure directing agents, etc. at different stages of crystallization. One example of how the rational adjustment of active site locations within the zeolite structure can result in catalytic improvements was pointed out in chapter 5; the placement of Al atoms at those T sites where the dissociative pathway (including methoxy formation) is the active route of the methanol dehydration reaction at some specific reaction conditions can be in favor of the alkene methylation reactions, while other Al sitings may benefit the production of DME via the associate route.

The experimental and theoretical work presented in this dissertation focused solely on H-form zeolites, which are employed in acid-catalyzed reactions such as fluid catalytic cracking (FCC). However, the metal-exchanged forms of zeolites are also used in redox reactions such as ammonia-assisted selective catalytic reduction (SCR) of NO_x.[18] The location of metal species within the zeolite structure and their chemistry, i.e., single cation, hydrated, etc., can impose an even higher level of heterogeneity in the catalytic performance. Knowledge of controlled adjustment of zeolite active site distribution combined with the large variety of topologies, pore shape and dimensions indicated by different zeolite frameworks can provide a great potential in the enhanced design of zeolite-catalyzed reactions to obtain the optimal catalytic performance. As such, my

dissertation provides motivation for further refinements of existing zeolite synthesis techniques and improvements, or even development of new characterization techniques that allow for an exact, i.e., atomic scale, determination of acid site locations in complex zeolite frameworks.

References

1. Martinez, C.; Corma, A., *Coord. Chem. Rev.* **2011,** *255* (13-14), 1558-1580.

2. Rimer, J. D.; Kumar, M.; Li, R.; Lupulescu, A. I.; Oleksiak, M. D., *Catal. Sci. Technol.* **2014,** *4* (11), 3762-3771.

3. Choi, M.; Na, K.; Kim, J.; Sakamoto, Y.; Terasaki, O.; Ryoo, R., *Nature* **2009,** *461* (7261), 246-U120.

4. Arsenova-Hartel, N.; Bludau, H.; Schumacher, R.; Haag, W. O.; Karge, H. G.; Brunner, E.; Wild, U., *J. Catal.* **2000,** *191* (2), 326-331.

5. Kim, J. H.; Kunieda, T.; Niwa, M., *J. Catal.* **1998,** *173* (2), 433-439.

6. Kim, K.; Ryoo, R.; Jang, H. D.; Choi, M., *J. Catal.* **2012,** *288*, 115-123.

7. Gounder, R.; Iglesia, E., *Chem. Commun.* **2013,** *49* (34), 3491-3509.

8. Eder, F.; Lercher, J. A., *J. Phys. Chem. B* **1997,** *101* (8), 1273-1278.

9. Eder, F.; Lercher, J. A., *Zeolites* **1997,** *18* (1), 75-81.

10. Eder, F.; Stockenhuber, M.; Lercher, J. A., *J. Phys. Chem. B* **1997,** *101* (27), 5414-5419.

11. Chiang, H.; Bhan, A., *J. Catal.* **2010,** *271* (2), 251-261.

12. Bhan, A.; Allian, A. D.; Sunley, G. J.; Law, D. J.; Iglesia, E., *J. Am. Chem. Soc.* **2007,** *129* (16), 4919-4924.

13. Moses, P. G., *J. Catal.* **2015,** *328*, 19-25.

14. Abild-Pedersen, F.; Greeley, J.; Studt, F.; Rossmeisl, J.; Munter, T. R.; Moses, P. G.; Skulason, E.; Bligaard, T.; Norskov, J. K., *Phys. Rev. Lett.* **2007,** *99* (1).

15. Andersson, M. P.; Bligaard, T.; Kustov, A.; Larsen, K. E.; Greeley, J.; Johannessen, T.; Christensen, C. H.; Norskov, J. K., *J. Catal.* **2006,** *239* (2), 501-506.

16. Norskov, J. K.; Bligaard, T.; Logadottir, A.; Bahn, S.; Hansen, L. B.; Bollinger, M.; Bengaard, H.; Hammer, B.; Sljivancanin, Z.; Mavrikakis, M.; Xu, Y.; Dahl, S.; Jacobsen, C. J. H., *J. Catal.* **2002,** *209* (2), 275-278.

17. Wang, S.; Petzold, V.; Tripkovic, V.; Kleis, J.; Howalt, J. G.; Skulason, E.; Fernandez, E. M.; Hvolbaek, B.; Jones, G.; Toftelund, A.; Falsig, H.; Bjorketun, M.; Studt, F.; Abild-Pedersen, F.; Rossmeisl, J.; Nørskov, J. K.; Bligaard, T., *Phys. Chem. Chem. Phys.* **2011,** *13* (46), 20760-20765.

18. Van Speybroeck, V.; Hemelsoet, K.; Joos, L.; Waroquier, M.; Bell, R. G.; Catlow, C. R. A., *Chem. Soc. Rev.* **2015,** *44* (20), 7044-7111.

19. Van Bokhoven, J. A.; Lee, T. L.; Drakopoulos, M.; Lamberti, C.; Thiess, S.; Zegenhagen, J., *Nat. Mater.* **2008,** *7* (7), 551-555.

20. Baerlocher, Ch.; McCusker, L. B. Database of Zeolite Structures: http://www.iza-structure.org/databases/.

21. Pinar, A. B.; Verel, R.; Perez-Pariente, J.; van Bokhoven, J. A., *Microporous Mesoporous Mat.* **2014,** *193*, 111-114.

22. Sklenak, S.; Dedecek, J.; Li, C.; Wichterlova, B.; Gabova, V.; Sierka, M.; Sauer, J., *Phys. Chem. Chem. Phys.* **2009,** *11* (8), 1237-1247.

23. Kim, C. W.; Heo, N. H.; Seff, K., *J. Phys. Chem. C* **2011,** *115* (50), 24823-24838.

24. Vjunov, A.; Fulton, J. L.; Huthwelker, T.; Pin, S.; Mei, D. H.; Schenter, G. K.; Govind, N.; Camaioni, D. M.; Hu, J. Z.; Lercher, J. A., *J. Am. Chem. Soc.* **2014,** *136* (23), 8296-8306.

25. Yokoi, T.; Mochizuki, H.; Namba, S.; Kondo, J. N.; Tatsumi, T., *J. Phys. Chem. C* **2015,** *119* (27), 15303-15315.

26. Ristanovic, Z.; Hofmann, J. P.; Deka, U.; Schulli, T. U.; Rohnke, M.; Beale, A. M.; Weckhuysen, B. M., *Angew. Chem., Int. Ed.* **2013,** *52* (50), 13382-13386.

27. Danilina, N.; Krumeich, F.; Castelanelli, S. A.; van Bokhoven, J. A., *J. Phys. Chem. C* **2010,** *114* (14), 6640-6645.

28. Vonballmoos, R.; Meier, W. M., *Nature* **1981,** *289* (5800), 782-783.

29. Chao, K. J.; Chern, J. Y., *Zeolites* **1988,** *8* (1), 82-85.

30. Althoff, R.; Schulzdobrick, B.; Schuth, F.; Unger, K., *Microporous Mater.* **1993,** *1* (3), 207-218.

31. Zhang, X.; Liu, D.; Xu, D.; Asahina, S.; Cychosz, K. A.; Agrawal, K. V.; Al Wahedi, Y.; Bhan, A.; Al Hashimi, S.; Terasaki, O.; Thommes, M.; Tsapatsis, M., *Science* **2012,** *336* (6089), 1684-1687.

32. Corma, A.; Fornes, V.; Martinez-Triguero, J.; Pergher, S. B., *J. Catal.* **1999,** *186* (1), 57-63.

33. Groen, J. C.; Zhu, W.; Brouwer, S.; Huynink, S. J.; Kapteijn, F.; Moulijn, J. A.; Pérez-Ramírez, J., *J. Am. Chem. Soc.* **2007,** *129* (2), 355-360.

34. Lupulescu, A. I.; Rimer, J. D., *Angew. Chem., Int. Ed.* **2012,** *51* (14), 3345-3349.

35. Argaman, N.; Makov, G., *Am. J. Phys.* **2000,** *68* (1), 69-79.

36. Grimme, S.; Antony, J.; Ehrlich, S.; Krieg, H., *J. Chem. Phys.* **2010,** *132* (15).

37. Klimeš, J.; Bowler, D. R.; Michaelides, A., *J. Phys.: Condens. Matter* **2010,** *22* (2), 1-5.

38. Klimeš, J.; Bowler, D. R.; Michaelides, A., *Phys. Rev. B* **2011,** *83* (19), 195131.

39. Lee, K.; Murray, É. D.; Kong, L.; Lundqvist, B. I.; Langreth, D. C., *Phys. Rev. B* **2010,** *82* (8), 081101.

40. Göltl, F.; Sautet, P., *J. Chem. Phys.* **2014,** *140* (15).

41. Kresse, G.; Furthmüller, J., *Comput. Mater. Sci.* **1996,** *6* (1), 15-50.

42. Kresse, G.; Hafner, J., *Phys. Rev. B* **1993,** *47* (1), 558-561.

43. Blöchl, P. E., *Phys. Rev. B* **1994,** *50* (24), 17953-17979.

44. Seo, Y.; Cho, K.; Jung, Y.; Ryoo, R., *ACS Catal.* **2013,** *3* (4), 713-720.

45. Rollmann, L. D. US4088605, 1978.

46. Chang, C. D.; Rodewald, P. G. US5475179, 1995.

47. Wichterlova, B.; Cejka, J., *Catal. Lett.* **1992,** *16* (4), 421-429.

48. Bartholomew, C. H., *Appl. Catal., A* **2001,** *212* (1–2), 17-60.

49. Corbin, D. R.; Schwarz, S.; Sonnichsen, G. C., *Catal. Today* **1997,** *37* (2), 71-102.

50. Foster, A. J.; Jae, J.; Cheng, Y. T.; Huber, G. W.; Lobo, R. F., *Appl. Catal., A* **2012,** *423*, 154-161.

51. Kwak, B. S.; Sung, J., *Catal. Lett.* **1998,** *53* (1-2), 125-129.

52. Yan, Z. M.; Ding, M. A.; Zhuang, J. Q.; Liu, X. C.; Liu, X. M.; Han, X. W.; Bao, X. H.; Chang, F. X.; Xu, L.; Liu, Z. M., *J. Mol. Catal. A: Chem.* **2003,** *194* (1-2), 153-167.

53. Zheng, S. R.; Jentys, A.; Lercher, J. A., *J. Catal.* **2003,** *219* (2), 310-319.

54. Choplin, A., *J. Mol. Catal.* **1994,** *86* (1-3), 501-512.

55. Cheng, Y. T.; Wang, Z. P.; Gilbert, C. J.; Fan, W.; Huber, G. W., *Angew. Chem., Int. Ed.* **2012,** *51* (44), 11097-11100.

56. Niwa, M.; Kato, S.; Hattori, T.; Murakami, Y., *J. Chem. Soc., Faraday Trans. 1* **1984,** *80*, 3135-3145.

57. Tominaga, K.; Maruoka, S.; Gotoh, M.; Katada, N.; Niwa, M., *Microporous Mesoporous Mat.* **2009,** *117* (3), 523-529.

58. Weber, R. W.; Fletcher, J. C. Q.; Moller, K. P.; O'Connor, C. T., *Microporous Mater.* **1996,** *7* (1), 15-25.

59. Zheng, S.; Heydenrych, H. R.; Roger, H. P.; Jentys, A.; Lercher, J. A., *Top. Catal.* **2003,** *22* (1-2), 101-106.

60. Chaudhuri, R. G.; Paria, S., *Chem. Rev.* **2012,** *112* (4), 2373-2433.

61. Dabbousi, B. O.; Rodriguez-Viejo, J.; Mikulec, F. V.; Heine, J. R.; Mattoussi, H.; Ober, R.; Jensen, K. F.; Bawendi, M. G., *J. Phys. Chem. B* **1997,** *101* (46), 9463-9475.

62. Reiss, P.; Protiere, M.; Li, L., *Small* **2009,** *5* (2), 154-168.

63. Zhu, Y. F.; Shi, J. L.; Shen, W. H.; Dong, X. P.; Feng, J. W.; Ruan, M. L.; Li, Y. S., *Angew. Chem., Int. Ed.* **2005,** *44* (32), 5083-5087.

64. Alayoglu, S.; Nilekar, A. U.; Mavrikakis, M.; Eichhorn, B., *Nat. Mater.* **2008,** *7* (4), 333-338.

65. Zhang, X.; Su, Z. H., *Adv. Mater.* **2012,** *24* (33), 4574-4577.

66. Kim, W. G.; Zhang, X. Y.; Lee, J. S.; Tsapatsis, M.; Nair, S., *ACS Nano* **2012,** *6* (11), 9978-9988.

67. Ji, Y. J.; Zhang, B.; Xu, L.; Wu, H. H.; Peng, H. G.; Chen, L.; Liu, Y. M.; Wu, P., *J. Catal.* **2011,** *283* (2), 168-177.

68. Porcher, F.; Dusausoy, Y.; Souhassou, M.; Lecomte, C., *Mineral. Mag.* **2000,** *64* (1), 1-8.

69. Okubo, T.; Wakihara, T.; Plevert, J.; Nair, S.; Tsapatsis, M.; Ogawa, Y.; Komiyama, H.; Yoshimura, M.; Davis, M., *Angew. Chem., Int. Ed.* **2001,** *40* (6), 1069.

70. Zheng, J. J.; Zhang, X. W.; Wang, Y.; Bai, Y. D.; Sun, W. F.; Li, R. F., *J. Porous Mat.* **2009,** *16* (6), 731-736.

71. Bouizi, Y.; Rouleau, L.; Valtchev, V. P., *Microporous Mesoporous Mat.* **2006,** *91* (1-3), 70-77.

72. Bouizi, Y.; Rouleau, L.; Valtchev, V. P., *Chem. Mater.* **2006,** *18* (20), 4959-4966.

73. Bouizi, Y.; Diaz, I.; Rouleau, L.; Valtchev, V. P., *Adv. Funct. Mater.* **2005,** *15* (12), 1955-1960.

74. Pirngruber, G. D.; Laroche, C.; Maricar-Pichon, M.; Rouleau, L.; Bouizi, Y.; Valtchev, V., *Microporous Mesoporous Mat.* **2013,** *169*, 212-217.

75. Bouizi, Y.; Majano, G.; Mintova, S.; Valtchev, V., *J. Phys. Chem. C* **2007,** *111* (12), 4535-4542.

76. Lovallo, M. C.; Boudreau, L.; Tsapatsis, M., Preparation of supported zeolite films and layers: Processing of zeolite suspensions and in situ growth from homogeneous solutions. In *Microporous and Macroporous Materials*, Lobo, R. F.; Beck, J. S.; Suib, S. L.; Corbin, D. R.; Davis, M. E.; Iton, L. E.; Zones, S. I., Eds. 1996; Vol. 431, pp 225-236.

77. Okamoto, M.; Osafune, Y., *Microporous Mesoporous Mat.* **2011,** *143* (2-3), 413-418.

78. Van Vu, D.; Miyamoto, M.; Nishiyama, N.; Egashira, Y.; Ueyama, K., *J. Catal.* **2006,** *243* (2), 389-394.

79. Van Vu, D.; Miyamoto, M.; Nishiyama, N.; Ichikawa, S.; Egashira, Y.; Ueyama, K., *Microporous Mesoporous Mat.* **2008,** *115* (1-2), 106-112.

80. Vu, D. V.; Miyamoto, M.; Nishiyama, N.; Egashira, Y.; Ueyama, K., *Catal. Lett.* **2009,** *127* (3-4), 233-238.

81. Lombard, A.; Simon-Masseron, A.; Rouleau, L.; Cabiac, A.; Patarin, J., *Microporous Mesoporous Mat.* **2010,** *129* (1-2), 220-227.

82. Mores, D.; Stavitski, E.; Verkleij, S. P.; Lombard, A.; Cabiac, A.; Rouleau, L.; Patarin, J.; Simon-Masseron, A.; Weckhuysen, B. M., *Phys. Chem. Chem. Phys.* **2011,** *13* (35), 15985-15994.

83. Persson, A. E.; Schoeman, B. J.; Sterte, J.; Otterstedt, J. E., *Zeolites* **1995,** *15* (7), 611-619.

84. Cundy, C. S.; Cox, P. A., *Microporous Mesoporous Mat.* **2005,** *82* (1-2), 1-78.

85. Lupulescu, A. I.; Rimer, J. D., *Science* **2014,** *344* (6185), 729-732.

86. Ren, N.; Subotic, B.; Bronic, J.; Tang, Y.; Sikiric, M. D.; Misic, T.; Svetlicic, V.; Bosnar, S.; Jelic, T. A., *Chem. Mater.* **2012,** *24* (10), 1726-1737.

87. Ren, N.; Bosnar, S.; Bronić, J.; Dutour Sikirić, M.; Mišić, T.; Svetličić, V.; Mao, J.-J.; Antonić Jelić, T.; Hadžija, M.; Subotić, B., *Langmuir* **2014,** *30*, 8570-8579.

88. Davis, T. M.; Drews, T. O.; Ramanan, H.; He, C.; Dong, J. S.; Schnablegger, H.; Katsoulakis, M. A.; Kokkoli, E.; McCormick, A. V.; Penn, R. L.; Tsapatsis, M., *Nat. Mater.* **2006,** *5* (5), 400-408.

89. Hasan, F.; Singh, R.; Li, G.; Zhao, D. Y.; Webley, P. A., *J. Colloid Interf. Sci.* **2012,** *382*, 1-12.

90. Itani, L.; Liu, Y.; Zhang, W. P.; Bozhilov, K. N.; Delmotte, L.; Valtchev, V., *J. Am. Chem. Soc.* **2009,** *131* (29), 10127-10139.

91. Maldonado, M.; Oleksiak, M. D.; Chinta, S.; Rimer, J. D., *J. Am. Chem. Soc.* **2013,** *135* (7), 2641-2652.

92. Althoff, R.; Schulz-Dobrick, B.; Schüth, F.; Unger, K., *Microporous Mater.* **1993,** *1* (3), 207-218.

93. Hughes, A. E.; Wilshier, K. G.; Sexton, B. A.; Smart, P., *J. Catal.* **1983,** *80* (1), 221-227.

94. Kosslick, H.; Fricke, R., Chemical Analysis of Aluminosilicates, Aluminophosphates and Related Molecular Sieves. In *Characterization II*, Karge, H.; Weitkamp, J., Eds. Springer Berlin Heidelberg: 2007; Vol. 5, pp 1-66.

95. Gorte, R. J., *Catal. Lett.* **1999,** *62* (1), 1-13.

96. Kofke, T. J. G.; Gorte, R. J.; Kokotailo, G. T., *J. Catal.* **1989,** *116* (1), 252-262.

97. Jones, A. J.; Carr, R. T.; Zones, S. I.; Iglesia, E., *J. Catal.* **2014,** *312*, 58-68.

98. Gounder, R.; Iglesia, E., *J. Am. Chem. Soc.* **2009,** *131* (5), 1958-1971.

99. O'Connor, C. T.; Moller, K. P.; Manstein, H., *CATTECH* **2001,** *5* (3), 172-182.

100. Odedairo, T.; Balasamy, R. J.; Al-Khattaf, S., *J. Mol. Catal. A: Chem.* **2011,** *345* (1-2), 21-36.

101. Sun, Y. Y.; Han, Y.; Yuan, L.; Ma, S. Q.; Jiang, D. H.; Xiao, F. S., *J. Phys. Chem. B* **2003,** *107* (8), 1853-1857.

102. Pham, T. N.; Sooknoi, T.; Crossley, S. P.; Resasco, D. E., *ACS Catal.* **2013,** *3* (11), 2456-2473.

103. Corma, A.; Fornes, V.; Forni, L.; Marquez, F.; Martinez-Triguero, J.; Moscotti, D., *J. Catal.* **1998,** *179* (2), 451-458.

104. Koo, J.-B.; Jiang, N.; Saravanamurugan, S.; Bejblova, M.; Musilova, Z.; Cejka, J.; Park, S.-E., *J. Catal.* **2010,** *276* (2), 327-334.

105. Hedlund, J.; Mintova, S.; Sterte, J., *Microporous Mesoporous Mat.* **1999,** *28* (1), 185-194.

106. Li, Q. H.; Wang, Z.; Hedlund, J.; Creaser, D.; Zhang, H.; Zou, X. D.; Bons, A. J., *Microporous Mesoporous Mat.* **2005,** *78* (1), 1-10.

107. Li, Y.; Lubchenko, V.; Vekilov, P. G., *Rev. Sci. Instrum.* **2011,** *82* (5).

108. Provencher, S. W., *Comput. Phys. Commun.* **1982,** *27* (3), 229-242.

109. Fedeyko, J. M.; Rimer, J. D.; Lobo, R. F.; Vlachos, D. G., *J. Phys. Chem. B* **2004,** *108* (33), 12271-12275.

110. Rimer, J. D.; Lobo, R. F.; Vlachos, D. G., *Langmuir* **2005,** *21*, 8960-8971.

111. de Moor, P.; Beelen, T. P. M.; Komanschek, B. U.; Diat, O.; van Santen, R. A., *J. Phys. Chem. B* **1997,** *101* (51), 11077-11086.

112. Kragten, D. D.; Fedeyko, J. M.; Sawant, K. R.; Rimer, J. D.; Vlachos, D. G.; Lobo, R. F.; Tsapatsis, M., *J. Phys. Chem. B* **2003,** *107* (37), 10006-10016.

113. Kumar, S.; Wang, Z. P.; Penn, R. L.; Tsapatsis, M., *J. Am. Chem. Soc.* **2008,** *130* (51), 17284.

114. Schoeman, B. J., *Microporous Mesoporous Mat.* **1998,** *22* (1-3), 9-22.

115. Watson, J. N.; Iton, L. E.; White, J. W., *Chem. Commun.* **1996,** (24), 2767-2768.

116. Rimer, J. D.; Fedeyko, J. M.; Vlachos, D. G.; Lobo, R. F., *Chem. Eur. J.* **2006,** *12* (11), 2926-2934.

117. Miyamoto, M.; Kamei, T.; Nishiyama, N.; Egashira, Y.; Ueyama, K., *Adv. Mater.* **2005,** *17* (16), 1985.

118. Corma, A., *Chem. Rev.* **1997,** *97* (6), 2373-2419.

119. Nicholas, J. B., *Top. Catal.* **1997,** *4* (1-2), 157-171.

120. Derouane, E. G.; Fripiat, J. G., *Zeolites* **1985,** *5* (3), 165-172.

121. Deka, R. C.; Vetrivel, R.; Pal, S., *J. Phys. Chem. A* **1999,** *103* (30), 5978-5982.

122. Zhao, Y.; Truhlar, D. G., *J. Phys. Chem. C* **2008,** *112* (17), 6860-6868.

123. Eichler, U.; Brandle, M.; Sauer, J., *J. Phys. Chem. B* **1997,** *101* (48), 10035-10050.

124. Joshi, Y. V.; Thomson, K. T., *J. Catal.* **2005,** *230* (2), 440-463.

125. Sillar, K.; Burk, P., *J. Mol. Struc.-Theochem* **2002,** *589*, 281-290.

126. Courtney, T. D.; Nikolakis, V.; Mpourmpakis, G.; Chen, J. G. G.; Vlachos, D. G., *Appl. Catal., A* **2012,** *449*, 59-68.

127. Stoyanov, S. R.; Gusarov, S.; Kuznicki, S. M.; Kovalenko, A., *J. Phys. Chem. C* **2008,** *112* (17), 6794-6810.

128. Hafner, J.; Benco, L.; Bucko, T., *Top. Catal.* **2006,** *37* (1), 41-54.

129. Olson, D. H.; Khosrovani, N.; Peters, A. W.; Toby, B. H., *J. Phys. Chem. B* **2000,** *104* (20), 4844-4848.

130. Schroder, K. P.; Sauer, J.; Leslie, M.; Catlow, C. R. A.; Thomas, J. M., *Chem. Phys. Lett.* **1992,** *188* (3-4), 320-325.

131. Brandle, M.; Sauer, J., *J. Am. Chem. Soc.* **1998,** *120* (7), 1556-1570.

132. Bruggemann, T. C.; Vlachos, D. G.; Keil, F. J., *J. Catal.* **2011,** *283* (2), 178-191.

133. Hansen, N.; Krishna, R.; van Baten, J. M.; Bell, A. T.; Keil, F. J., *J. Phys. Chem. C* **2009,** *113* (1), 235-246.

134. Liu, D. X.; Bhan, A.; Tsapatsis, M.; Al Hashimi, S., *ACS Catal.* **2011,** *1* (1), 7-17.

135. Mihaleva, V. V.; van Santen, R. A.; Jansen, A. P. J., *J. Chem. Phys.* **2003,** *119* (24), 13053-13060.

136. Yang, L.; Trafford, K.; Kresnawahjuesa, O.; Sepa, J.; Gorte, R. J.; White, D., *J. Phys. Chem. B* **2001,** *105* (10), 1935-1942.

137. Chu, Y. Y.; Han, B.; Zheng, A. M.; Deng, F., *J. Phys. Chem. C* **2012,** *116* (23), 12687-12695.

138. Klimes, J.; Bowler, D. R.; Michaelides, A., *J. Phys.: Condens. Matter* **2010,** *22* (2).

139. Klimes, J.; Bowler, D. R.; Michaelides, A., *Phys. Rev. B* **2011,** *83* (19).

140. Bahn, S. R.; Jacobsen, K. W., *Comput. Sci. Eng.* **2002,** *4* (3), 56-66.

141. Kresse, G.; Furthmuller, J., *Comput. Mater. Sci.* **1996,** *6* (1), 15-50.

142. Grimme, S., *J. Comput. Chem.* **2006,** *27* (15), 1787-1799.

143. Ch. Baerlocher, L. B. M., D.H. Olson, *Atlas of Zeolite Framework Types*. Elsevier: New York, 2007.

144. Kresse, G.; Furthmuller, J., *Phys. Rev. B* **1996,** *54* (16), 11169-11186.

145. Kresse, G.; Hafner, J., *Phys. Rev. B* **1994,** *49* (20), 14251-14269.

146. Perdew, J. P.; Burke, K.; Ernzerhof, M., *Phys. Rev. Lett.* **1996,** *77* (18), 3865-3868.

147. Hammer, B.; Hansen, L. B.; Norskov, J. K., *Phys. Rev. B* **1999,** *59* (11), 7413-7421.

148. Perdew, J. P.; Chevary, J. A.; Vosko, S. H.; Jackson, K. A.; Pederson, M. R.; Singh, D. J.; Fiolhais, C., *Phys. Rev. B* **1992,** *46* (11), 6671-6687.

149. Civalleri, B.; Garrone, E.; Ugliengo, P., *J. Phys. Chem. B* **1998,** *102* (13), 2373-2382.

150. Kubelkova, L.; Beran, S.; Lercher, J. A., *Zeolites* **1989,** *9* (6), 539-543.

151. Farneth, W. E.; Gorte, R. J., *Chem. Rev.* **1995,** *95* (3), 615-635.

152. Parrillo, D. J.; Lee, C.; Gorte, R. J., *Appl. Catal., A* **1994,** *110* (1), 67-74.

153. Janik, M. J.; Davis, R. J.; Neurock, M., *Catal. Today* **2005,** *105* (1), 134-143.

154. Haw, J. F.; Song, W. G.; Marcus, D. M.; Nicholas, J. B., *Accounts Chem. Res.* **2003,** *36* (5), 317-326.

155. Hemelsoet, K.; Van der Mynsbrugge, J.; De Wispelaere, K.; Waroquier, M.; Van Speybroeck, V., *ChemPhysChem* **2013,** *14* (8), 1526-1545.

156. Lesthaeghe, D.; Van Speybroeck, V.; Marin, G. B.; Waroquier, M., *Angew. Chem., Int. Ed.* **2006,** *45* (11), 1714-1719.

157. Stöcker, M., *Microporous Mesoporous Mat.* **1999,** *29* (1-2), 3-48.

158. Bjørgen, M.; Svelle, S.; Joensen, F.; Nerlov, J.; Kolboe, S.; Bonino, F.; Palumbo, L.; Bordiga, S.; Olsbye, U., *J. Catal.* **2007,** *249* (2), 195-207.

159. Dahl, I. M.; Kolboe, S., *J. Catal.* **1994,** *149* (2), 458-464.

160. Ilias, S.; Bhan, A., *ACS Catal.* **2013,** *3* (1), 18-31.

161. Sun, J.; Yang, G. H.; Yoneyama, Y.; Tsubaki, N., *ACS Catal.* **2014,** *4* (10), 3346-3356.

162. Cheung, P.; Bhan, A.; Sunley, G. J.; Iglesia, E., *Angew. Chem., Int. Ed.* **2006,** *45* (10), 1617-1620.

163. Liu, H. C.; Cheung, P.; Iglesia, E., *J. Catal.* **2003,** *217* (1), 222-232.

164. Hazari, N.; Iglesia, E.; Labinger, J. A.; Simonetti, D. A., *Accounts Chem. Res.* **2012,** *45* (4), 653-662.

165. Li, X. A.; San, X. G.; Zhang, Y.; Ichii, T.; Meng, M.; Tan, Y. S.; Tsubaki, N., *ChemSusChem* **2010,** *3* (10), 1192-1199.

166. Arcoumanis, C.; Bae, C.; Crookes, R.; Kinoshita, E., *Fuel* **2008,** *87* (7), 1014-1030.

167. Olah, G. A.; Goeppert, A.; Prakash, G. K. S., *J. Org. Chem.* **2009,** *74* (2), 487-498.

168. Semelsberger, T. A.; Borup, R. L.; Greene, H. L., *J. Power Sources* **2006,** *156* (2), 497-511.

169. Blaszkowski, S. R.; van Santen, R. A., *J. Am. Chem. Soc.* **1996,** *118* (21), 5152-5153.

170. Blaszkowski, S. R.; van Santen, R. A., *J. Phys. Chem. B* **1997,** *101* (13), 2292-2305.

171. Carr, R. T.; Neurock, M.; Iglesia, E., *J. Catal.* **2011,** *278* (1), 78-93.

172. Schiffino, R. S.; Merrill, R. P., *J. Phys. Chem.* **1993,** *97* (24), 6425-6435.

173. Sinclair, P. E.; Catlow, C. R. A., *J. Chem. Soc., Faraday Trans.* **1996,** *92* (12), 2099-2105.

174. Moses, P. G.; Nørskov, J. K., *ACS Catal.* **2013,** *3* (4), 735-745.

175. Shah, R.; Gale, J. D.; Payne, M. C., *J. Phys. Chem. B* **1997,** *101* (24), 4787-4797.

176. Jones, A. J.; Iglesia, E., *Angew. Chem., Int. Ed.* **2014,** *53* (45), 12177-12181.

177. Kubelková, L.; Nováková, J.; Nedomová, K., *J. Catal.* **1990,** *124* (2), 441-450.

178. Sandré, E.; Payne, M. C.; Gale, J. D., *Chem. Commun.* **1998,** (22), 2445-2446.

179. Olsbye, U.; Svelle, S.; Bjørgen, M.; Beato, P.; Janssens, T. V. W.; Joensen, F.; Bordiga, S.; Lillerud, K. P., *Angew. Chem., Int. Ed.* **2012,** *51* (24), 5810-5831.

180. Yang, L.; Trafford, K.; Kresnawahjuesa, O.; Šepa, J.; Gorte, R. J.; White, D., *J. Phys. Chem. B* **2001,** *105* (10), 1935-1942.

181. Kim, K.; Ryoo, R.; Jang, H.-D.; Choi, M., *J. Catal.* **2012,** *288*, 115-123.

182. Jones, A. J.; Zones, S. I.; Iglesia, E., *J. Phys. Chem. C* **2014,** *118* (31), 17787-17800.

183. Artioli, N.; Lobo, R. F.; Iglesia, E., *J. Phys. Chem. C* **2013,** *117* (40), 20666-20674.

184. Ghorbanpour, A.; Rimer, J. D.; Grabow, L. C., *Catal. Commun.* **2014,** *52*, 98-102.

185. Brogaard, R. Y.; Weckhuysen, B. M.; Nørskov, J. K., *J. Catal.* **2013,** *300*, 235-241.

186. Piccini, G.; Sauer, J., *J. Chem. Theory Comput.* **2013,** *9* (11), 5038-5045.

187. Henkelman, G.; Uberuaga, B. P.; Jónsson, H., *J. Chem. Phys.* **2000,** *113* (22), 9901-9904.

188. Perea, D. E.; Arslan, I.; Liu, J.; Ristanović, Z.; Kovarik, L.; Arey, B. W.; Lercher, J. A.; Bare, S. R.; Weckhuysen, B. M., *Nat. Commun.* **2015,** *6*.

189. Ivanova, S.; Vanhaecke, E.; Louis, B.; Libs, S.; Ledoux, M.-J.; Rigolet, S.; Marichal, C.; Pham, C.; Luck, F.; Pham-Huu, C., *ChemSusChem* **2008,** *1* (10), 851-857.

190. Rownaghi, A. A.; Rezaei, F.; Stante, M.; Hedlund, J., *Appl. Catal., B* **2012,** *119*, 56-61.

191. Xu, M. T.; Lunsford, J. H.; Goodman, D. W.; Bhattacharyya, A., *Appl. Catal., A* **1997,** *149* (2), 289-301.

192. Nguyen, C. M.; Reyniers, M.-F.; Marin, G. B., *Phys. Chem. Chem. Phys.* **2010,** *12* (32), 9481-9493.

193. Brogaard, R. Y.; Moses, P. G.; Nørskov, J. K., *Catal. Lett.* **2012,** *142* (9), 1057-1060.

194. Wellendorff, J.; Lundgaard, K. T.; Møgelhøj, A.; Petzold, V.; Landis, D. D.; Nørskov, J. K.; Bligaard, T.; Jacobsen, K. W., *Phys. Rev. B* **2012,** *85* (23).

195. Brogaard, R. Y.; Henry, R.; Schuurman, Y.; Medford, A. J.; Moses, P. G.; Beato, P.; Svelle, S.; Nørskov, J. K.; Olsbye, U., *J. Catal.* **2014,** *314*, 159-169.

196. Mlinar, A. N.; Zimmerman, P. M.; Celik, F. E.; Head-Gordon, M.; Bell, A. T., *J. Catal.* **2012,** *288*, 65-73.

197. Wang, M.; Xia, Y.; Zhao, L.; Song, C.; Peng, L.; Guo, X.; Xue, N.; Ding, W., *J. Catal.* **2014,** *319*, 150-154.

198. Ghorbanpour, A.; Gumidyala, A.; Grabow, L. C.; Crossley, S. P.; Rimer, J. D., *ACS Nano* **2015,** *9* (4), 4006-4016.

199. Barzetti, T.; Selli, E.; Moscotti, D.; Forni, L., *J. Chem. Soc., Faraday Trans.* **1996,** *92* (8), 1401-1407.

200. Corma, A.; Fornés, V.; Forni, L.; Márquez, F.; Martínez-Triguero, J.; Moscotti, D., *J. Catal.* **1998,** *179* (2), 451-458.

201. Arce-Ramos, J. M.; Grabow, L. C.; Handy, B. E.; Cardenas-Galindot, M. G., *J. Phys. Chem. C* **2015,** *119* (27), 15150-15159.

202. Brändle, M.; Sauer, J., *J. Am. Chem. Soc.* **1998,** *120* (7), 1556-1570.

203. Chatterjee, A.; Bhattacharya, D.; Chatterjee, M.; Iwasaki, T., *Microporous Mesoporous Mat.* **1999,** *32* (1-2), 189-198.

204. Shor, E. A. I.; Shor, A. M.; Nasluzov, V. A.; Vayssilov, G. N.; Rösch, N., *J. Chem. Theory Comput.* **2005,** *1* (3), 459-471.

205. Jin, Y. J.; Asaoka, S.; Zhang, S. D.; Li, P.; Zhao, S. L., *Fuel Process. Technol.* **2013,** *115*, 34-41.

206. Wang, C.-M.; Brogaard, R. Y.; Xie, Z. K.; Studt, F., *Catal. Sci. Technol.* **2015,** *5* (5), 2814-2820.

207. Wang, C.-M.; Brogaard, R. Y.; Weckhuysen, B. M.; Nørskov, J. K.; Studt, F., *J. Phys. Chem. Lett.* **2014,** *5* (9), 1516-1521.

208. Jones, A. J.; Iglesia, E., *ACS Catal.* **2015,** *5*, 5741-5755.

209. Dedecek, J.; Balgova, V.; Pashkova, V.; Klein, P.; Wichterlova, B., *Chem. Mater.* **2012,** *24* (16), 3231-3239.

210. Opalka, S. M.; Zhu, T., *Microporous Mesoporous Mat.* **2016,** *222*, 256-270.

211. Sazama, P.; Dedecek, J.; Gabova, V.; Wichterlova, B.; Spoto, G.; Bordiga, S., *J. Catal.* **2008,** *254* (2), 180-189.

212. Henkelman, G.; Arnaldsson, A.; Jonsson, H., *Comput. Mater. Sci.* **2006,** *36* (3), 354-360.

213. Díaz, I.; Kokkoli, E.; Terasaki, O.; Tsapatsis, M., *Chem. Mater.* **2004**, *16*, 5226-5232.

Appendix A: Supplementary characterization of the synthesized ZSM-5 and ZSM-5@silicalite-1 samples

A.1 Powder X-ray diffraction (XRD)

Powder XRD measurements were performed to verify the crystallinity of annealed and non-annealed H-ZSM-5 samples. XRD confirmed that each sample possessed the expected crystal structure without the appearance of impurities or amorphous material. The resulting curves were compared to a standard XRD pattern of calcined MFI zeolite.[213] Figure A.1 indicates that both samples possess an MFI framework structure and that the annealing step did not alter the crystallinity.

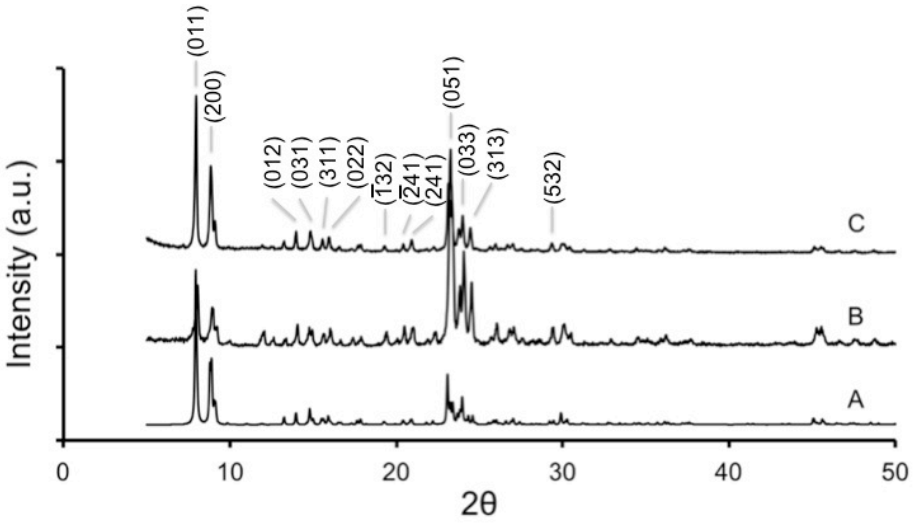

Figure A.1 Powder XRD patterns of (A) reference calcined MFI zeolite[20] along with (B) the non-annealed and (C) annealed H-ZSM-5 crystals synthesized in this study. Comparison of experimental patterns to the reference pattern reveals that both non-annealed and annealed H-ZSM-5 samples possess an MFI crystal structure. Indexed peaks on the reference pattern were obtained from the International Zeolite Association Structure Database.[20]

A.2 Physisorption measurements

Nitrogen adsorption/desorption measurements at 77 K were carried out to assess the textural properties of core and core-shell samples and to elucidate the potential blockage of pores as a result of ZSM-5 surface passivation with silicalite-1. The N_2 isotherms (Figure A.2) exhibit a type I pattern that is characteristic of microporous materials. BET analysis revealed almost identical surface area for core and core-shell samples (475 and 454 m^2/g, respectively), suggesting pore blockage is negligible.

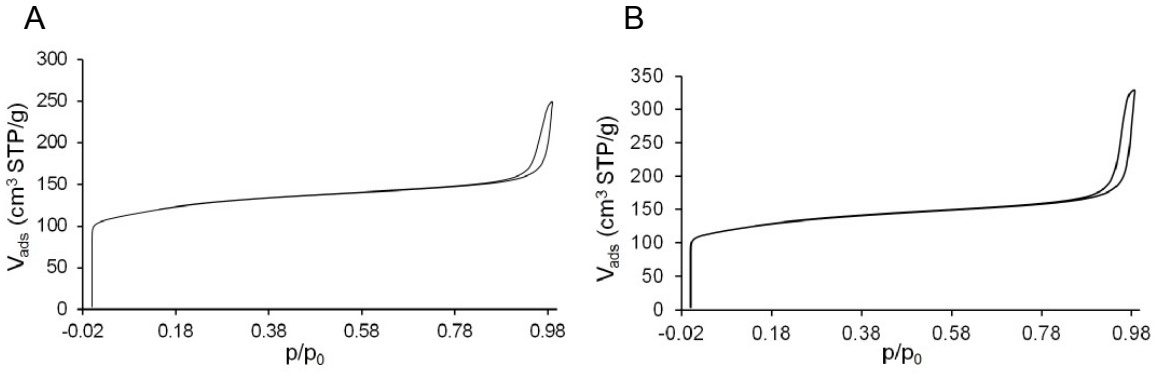

Figure A.2 Nitrogen adsorption/desorption isotherms for H-ZSM-5 core (A) and core-shell (B) samples. The core-shell sample for BET analysis was prepared using a silicalite-1 growth solution with a molar composition of 20 TEOS:14 TPAOH:9500 H_2O (i.e., 10 nm shell thickness).

A.3 Dynamic light scattering (DLS) studies

Figure A.3 contains a representative autocorrelation function (Figure A.3A) and CONTIN particle size distribution (Figure A.3B) for DLS analysis of ZSM-5@silicalite-1 particles.

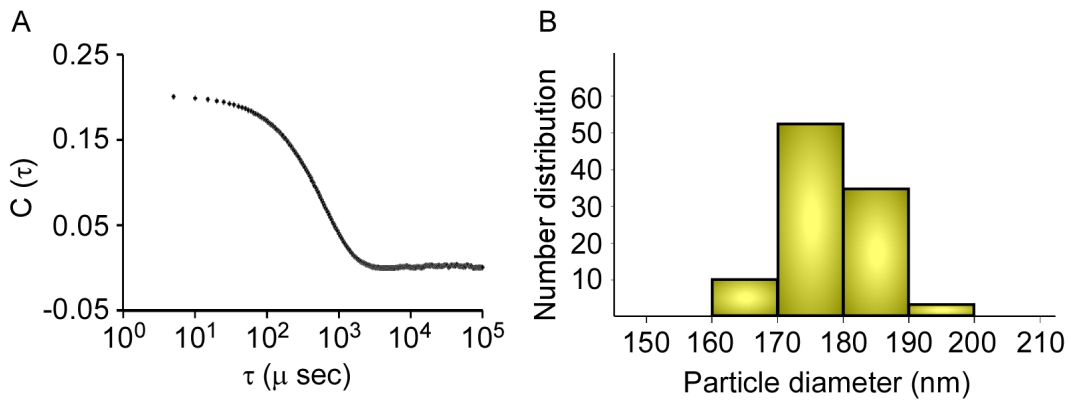

Figure A.3 (A) DLS autocorrelation function of a ZSM-5@silicalite-1 sample that was prepared in a silicalite-1 growth solution with a molar composition of 14 TEOS:7 TPAOH: 9500 H_2O (heated for 6 h at 100 °C). (B) The corresponding CONTIN analysis of the autocorrelation function reveals a single particle size distribution.

A.4 Di-tertbutyl pyridine adsorption infrared (IR) spectroscopy

IR spectra of H-ZSM-5 and H-ZSM-5@silicalite-1 were compared before and after adsorption of a bulky pyridine, di-tertbutyl pyridine (DTBP). Protonation of DTBP appears at 1616 cm^{-1}.

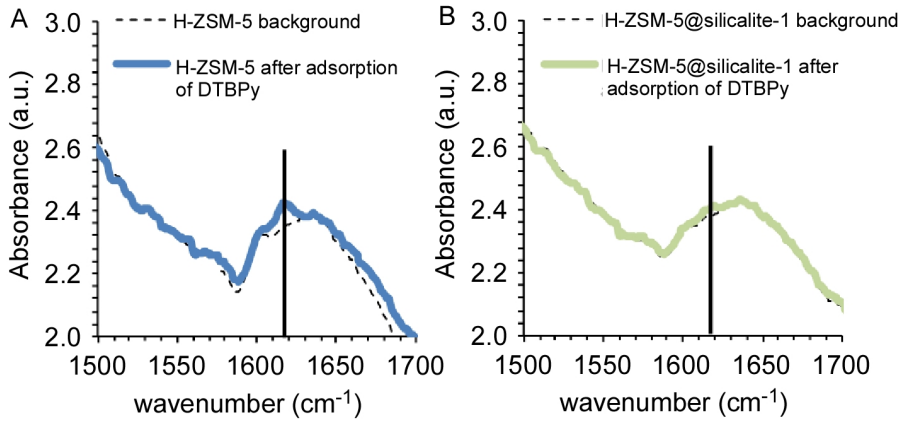

Figure A.4 Di-tertbutyl pyridine (DTPB) adsorption and analysis by IR for (A) H-ZSM-5 and (B) H-ZSM-5@silicalite-1. The IR spectroscopy results were provided by our collaborator, Prof. Crossley, and his group.

A.5 Isopropylamine (IPA) temperature programmed desorption (TPD)

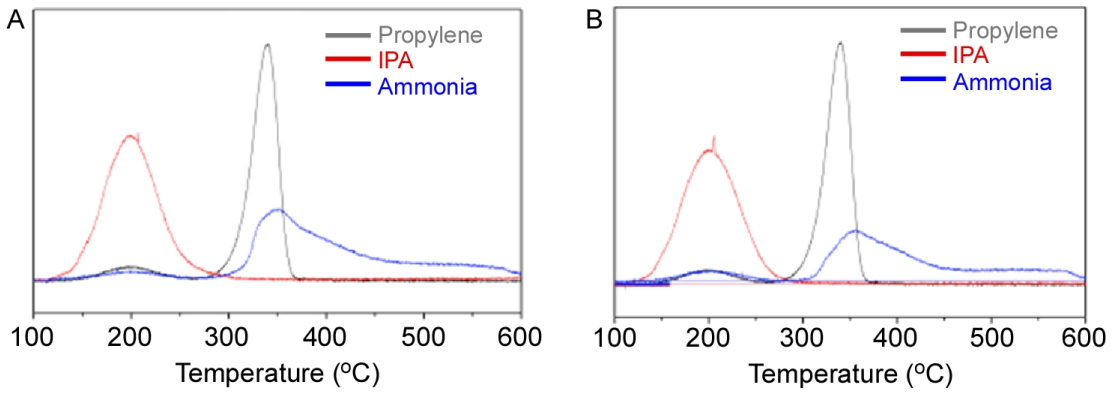

Figure A.5 Isopropylamine (IPA) TPD signals resulting from (A) H-ZSM-5 (core) and (B) H-ZSM-5@silicalite-1 (core-shell) samples. The IPA TPD results were provided by our collaborator, Prof. Crossley, and his group.

A.6 X-ray photoelectron spectroscopy (XPS)

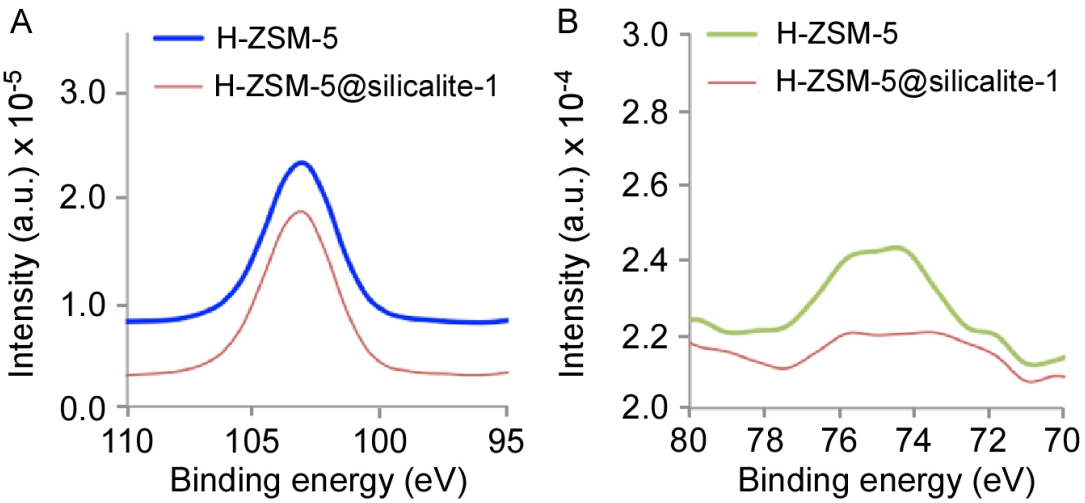

Figure A.6 XPS results of (A) Si 2p and (B) Al 2p binding energy regions for H-ZSM-5 (core) and H-ZSM-5@silicalite-1 (core-shell) samples. The H-ZSM-5 samples are offset in the y-axis for clarity. Data were collected at 45° takeoff angle; and to compensate for surface charging effects, the spectra were referenced to the hydrocarbon C 1s peak at 284.6 eV. The XPS results were provided by our collaborator, Prof. Crossley, and his group.

A.7 ^{27}Al NMR measurements

The extra-framework Al content in H-ZSM-5 and H-ZSM-5@silicalite-1 samples was quantified by ^{27}Al NMR. As shown in Figure 3.4, the intensities at 60 and 0 ppm correspond to framework and extra-framework alumina, respectively. Using these intensities we calculated the percentage of extra-framework alumina (Table A.1) based on the following expression

$$\left(\frac{Si}{Al}\right)_{framework} = \left(\frac{Si}{Al}\right)_{total} \cdot \frac{I_{60}+I_0}{I_{60}}, \quad \text{(A.1)}$$

where I_x is the intensity (x = 60 or 0 ppm) and $(Si/Al)_{total}$ accounts for both framework and extra-framework alumina in the zeolite. The amount of extra-framework Al reported here is lower than the amount typically reported for commercial MFI catalysts.[97-98]

Table A.1 Total Si/Al ratio and framework Si/Al ratio of H-ZSM-5 and H-ZSM-5@silicalite-1 estimated from ^{27}Al NMR. The ^{27}Al NMR results were provided by our collaborator, Prof. Crossley, and his group.

	Si/Al_{total}[a]	**$Si/Al_{framework}$**	**%Extra-framework alumina**
Core	44	48.5	9.1
Core-shell	53	55.8	5.0

[a] Si/Al_{total} from ICP-AES

A.8 TEM measurements

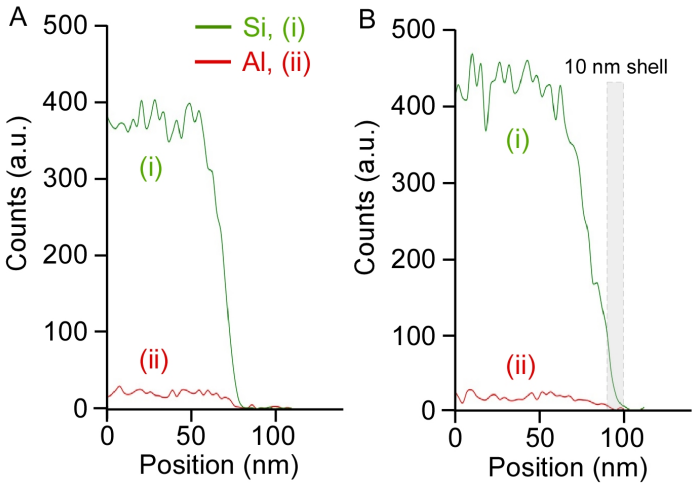

Figure A.7 Transmission electron microscopy (TEM) energy-dispersive X-ray spectroscopy (EDS) line scans along the cross-section of (A) core (ZSM-5) and (B) core-shell (ZSM-5@silicalite-1) particles.

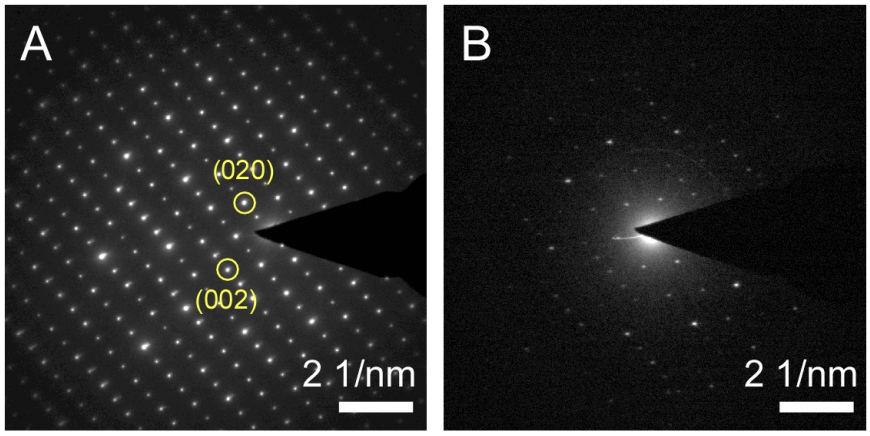

Figure A.8 Selected area electron diffraction (SAED) patterns of a core-shell particle reveal that ZSM-5@silicalite-1 is a single crystal. (A) The area selected for this SAED pattern on a (100) zone axis was located towards the center of the particle, thus encompassing both core and shell. (B) The area selected for this SAED pattern was located near the edge of the particle to confirm the crystallinity of the silicalite-1 shell.

Appendix B: Computational modeling of H-ZSM-5 external active sites

A modeling of the properties of H-ZSM-5 active sites located on its external surface was performed. The first step in such a modeling is to make a reasonable choice of the ZSM-5 crystal surface over which the T sites are studied. The surface properties of zeolites are dependent on synthesis conditions. ZSM-5 micron size crystals prepared with TPA cations as the SDA typically show a coffin shape morphology and form the largest surface perpendicular to the b axis.[213] Therefore, we considered the MFI zeolite crystal face perpendicular to the b axis as the dominant surface to be used in our modeling. Díaz et al. obtained HRTEM images of siliceous MFI zeolite crystals, which show the (010) facet is terminated so that the number of Si—OH groups on the surface is minimized (Figure B.1).[213] Although these crystals were obtained in the presence of the trimer TPA cations, bis-N,N-(tripropylammoniumhexamethylene)di-N,N-propylammonium trihydroxide, as the OSDA, the authors argued that the surface structure in the presence of the TPA cations will also be the same.

This information was used to construct the ZSM-5 surface model. An optimized silicalite-1 unit cell was used. The unit cell was cut at half along the b direction at the level explained above, while it was preserved as it was along the other two directions. The resulting dangling bonds were saturated by attaching hydrogen atoms to the oxygen atoms on the surface (no T site was present at the first atomic layer of the created surface). To simulate the crystal bulk, half of the cell along the b direction, except hydrogen atoms, was constrained for all the subsequent calculations and relaxation of atoms was done only for the other half. A vacuum space as long as 8 Å was placed at

either side of the cell along the b direction, while keeping the periodic boundary condition along the a and c directions. This model was used for all the following ZSM-5 surface calculations. It turned out that only four T sites, i.e., T7, T9, T10, and T12 were present in the first layer of T sites in this surface model. Figure B.2 shows the constructed model from the a-axis and b-axis views. We note that there are only three potential locations, i.e., bridging oxygen atoms, for the Brønsted acid proton around each Al site; the fourth oxygen atom appears in the form of a surface hydroxyl group.

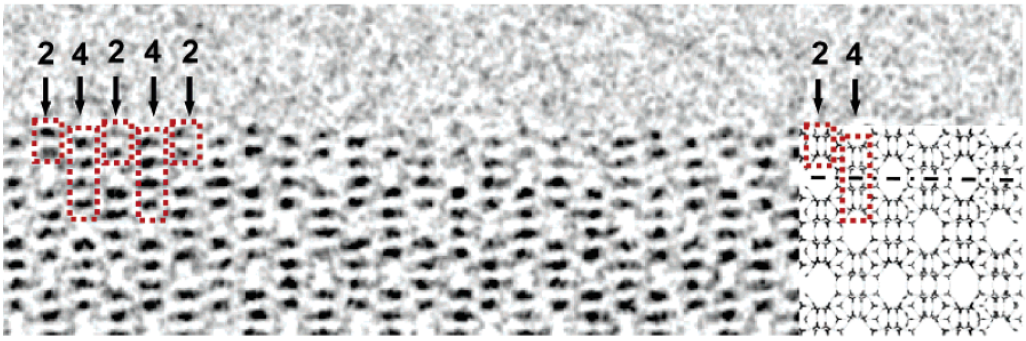

Figure B.1 HRTEM image of a siliceous MFI crystal down the a axis (sinusoidal channels). The arrows and red dots help to identify the surface termination at the crystal facet normal to the b axis, i.e., the (010) surface.[213]

The computational method was the same as that described in chapter 4, with two exceptions, cutoff energy = 400 eV and the net force convergence criterion equal to 0.05 eV/Å. For Al located at each of the T sites, the most stable Brønsted proton location was identified and considered for subsequent calculations (all of these sites were accessible to potential adsorbates). Table B.1 shows the stability (relative to the most stable T site), Brønsted O—H stretch frequency, Brønsted O—H bond length, and Si—OH—Al bond angle of the surface models with Al substituted at the four possible T sites. The definition of active site identifier is the same as that introduced in chapter 4.

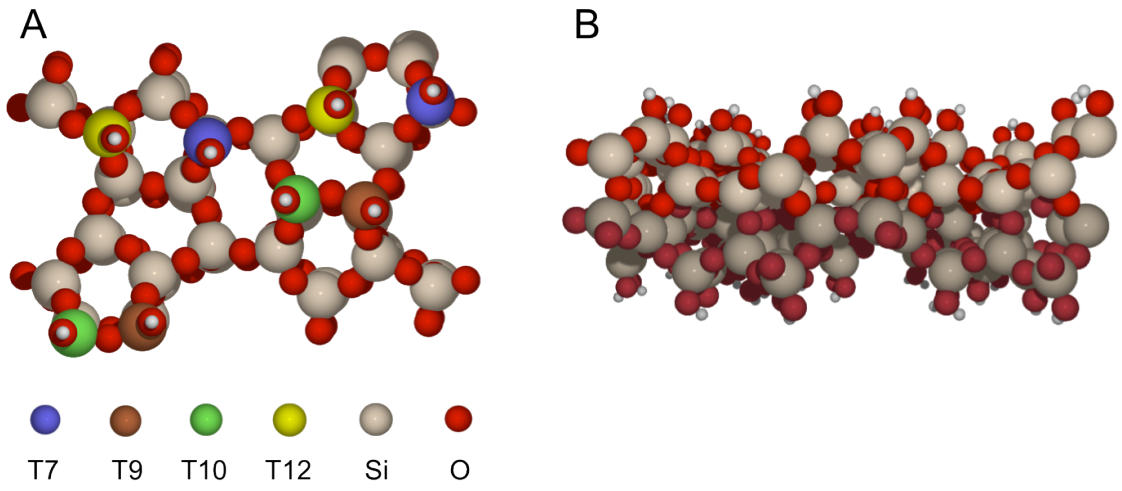

Figure B.2 The (010) surface model of zeolite MFI from two views: A) along the b axis and B) along the a axis. The four possible T sites of the surface are highlighted with color codes in panel A. The cell shown in panel B is repeated in the a and c directions. The darker lower half of the structure in panel B shows that part of the model which was constrained in geometry optimizations.

Table B.1 Properties of different Al-substituted T sites on the (010) surface of H-ZSM-5.

Active site identifier	**Stability (eV)**	**O—H frequency (cm^{-1})**	**O—H bond length (Å)**	**Si—OH—Al bond angle**
7—8	0.37	3601	0.981	138.2
9—10	0.00	3055	1.007	125.8
10—9	0.34	–	0.984	147.2
12—8	0.27	3088	1.005	140.2

Frequency calculations of the 10—9 model did not converge. This problem occurred in the calculation of the bulk properties of H-ZSM-5 as well and was solved only after the cutoff energy was raised to 540 eV. Examining the Brønsted O—H bond length values reported in Table B.1 and considering the correlation between the O—H bond length and

frequency of bulk sites reported in Table 4.3, we expect the O—H stretch frequency of 10—9 surface site to be around 3600 cm^{-1}.

Table B.2 lists the binding energies of CH_4, NH_3, CO, C_5H_5N, and CH_3OH on the four studies acid sites of H-ZSM-5 surface.

Table B.2 Binding energies of several probe molecules on potential active sites of H-ZSM-5 (010) surface.

Active site identifier	**CH_4**	**NH_3**	**CO**	**C_5H_5N**	**CH_3OH**
7—8	-0.41	-1.86	-0.60	-1.77	-1.25
9—10	-0.20	-1.50	0.00	-1.56	-0.68
10—9	-0.20	-1.94	-0.28	-1.70	-1.28
12—8	-0.29	-1.56	-0.38	-1.34	-0.97